



National Library  
of Canada

Acquisitions and  
Bibliographic Services Branch

395 Wellington Street  
Ottawa, Ontario  
K1A 0N4

Bibliothèque nationale  
du Canada

Direction des acquisitions et  
des services bibliographiques

395, rue Wellington  
Ottawa (Ontario)  
K1A 0N4

*Your file / Votre référence*

*Our file / Notre référence*

## NOTICE

## AVIS

The quality of this microform is heavily dependent upon the quality of the original thesis submitted for microfilming. Every effort has been made to ensure the highest quality of reproduction possible.

La qualité de cette microforme dépend grandement de la qualité de la thèse soumise au microfilmage. Nous avons tout fait pour assurer une qualité supérieure de reproduction.

If pages are missing, contact the university which granted the degree.

S'il manque des pages, veuillez communiquer avec l'université qui a conféré le grade.

Some pages may have indistinct print especially if the original pages were typed with a poor typewriter ribbon or if the university sent us an inferior photocopy.

La qualité d'impression de certaines pages peut laisser à désirer, surtout si les pages originales ont été dactylographiées à l'aide d'un ruban usé ou si l'université nous a fait parvenir une photocopie de qualité inférieure.

Reproduction in full or in part of this microform is governed by the Canadian Copyright Act, R.S.C. 1970, c. C-30, and subsequent amendments.

La reproduction, même partielle, de cette microforme est soumise à la Loi canadienne sur le droit d'auteur, SRC 1970, c. C-30, et ses amendements subséquents.

Canada

**University of Alberta**

**Generation of Microwave Subcarrier Signals on Optical Fiber  
Using Mach-Zehnder Modulator Non-linearities**

by

**Tom Y. S. Young** ©

A thesis submitted to the Faculty of Graduate Studies and Research in partial fulfillment  
of the requirements for the degree of **Master of Science**.

**Department of Electrical Engineering**

**Edmonton, Alberta**

Spring, 1996



National Library  
of Canada

Acquisitions and  
Bibliographic Services Branch

395 Wellington Street  
Ottawa, Ontario  
K1A 0N4

Bibliothèque nationale  
du Canada

Direction des acquisitions et  
des services bibliographiques

395, rue Wellington  
Ottawa (Ontario)  
K1A 0N4

*Your file* *Votre référence*

*Your file* *Notre référence*

**The author has granted an irrevocable non-exclusive licence allowing the National Library of Canada to reproduce, loan, distribute or sell copies of his/her thesis by any means and in any form or format, making this thesis available to interested persons.**

**L'auteur a accordé une licence irrévocable et non exclusive permettant à la Bibliothèque nationale du Canada de reproduire, prêter, distribuer ou vendre des copies de sa thèse de quelque manière et sous quelque forme que ce soit pour mettre des exemplaires de cette thèse à la disposition des personnes intéressées.**

**The author retains ownership of the copyright in his/her thesis. Neither the thesis nor substantial extracts from it may be printed or otherwise reproduced without his/her permission.**

**L'auteur conserve la propriété du droit d'auteur qui protège sa thèse. Ni la thèse ni des extraits substantiels de celle-ci ne doivent être imprimés ou autrement reproduits sans son autorisation.**

ISBN 0-612-10771-X

**Canada**

# University of Alberta

## Library Release Form

**Name of Author:** Tom Yun Sang Young


**Title of Thesis:** Generation of Microwave Subcarrier Signals on Optical  
Fiber Using Mach-Zehnder Modulator Non-linearities

**Degree:** Master of Science

**Year this Degree Granted:** 1996

Permission is hereby granted to the University of Alberta Library to reproduce single copies of this thesis and to lend or sell such copies for private, scholarly, or scientific research purposes only.

The author reserves all other publication and other rights in association with the copyright in the thesis, and except as hereinbefore provided, neither the thesis nor any substantial portion thereof may be printed or otherwise reproduced in any material form whatever without the author's prior written permission.

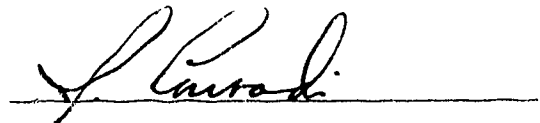
  
\_\_\_\_\_  
3441-111 A Street  
Edmonton, Alberta, Canada  
T6J 3L1

Date: Dec 6, 95

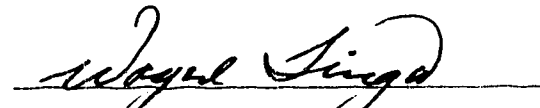
# University of Alberta

## Faculty of Graduate Studies and Research

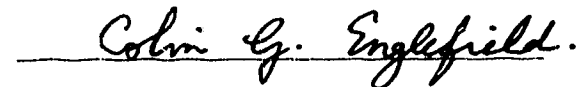
The undersigned certify that they have read, and recommend to the Faculty of Graduate Studies and Research for acceptance, a thesis entitled **Generation of Microwave Subcarrier Signals on Optical Fiber Using Mach-Zehnder Modulator Non-linearities** submitted by **Tom Yun Sang Young** in partial fulfillment of the requirements for the degree of **Master of Science**.



Dr. Jan Conradi, Co-supervisor



Dr. Wayne Tinga, Co-supervisor



Dr. Colin Englefield, Internal



Dr. Pavel Gburzynski, External

Date: Dec. 6/95

*"Whatever you do, work at it with all your heart,  
as working for the Lord, not for men..."*

*Colossians 3:23*

*To my parents,  
for their love, support and encouragement.*

## **Abstract**

This project is motivated by the rising demand for wireless personal communication systems. The microcellular system, which is similar to the conventional cellular telephone system but with much smaller cell size, has been proposed as a possible solution to this demand. An optical fiber feeder can be used in a microcellular system to distribute the RF signals to the base stations. Since there are various inherent advantages in operating a microcellular system at microwave or millimeter-wave frequencies, different techniques for the generation of optical signals at these frequencies have been studied. This thesis presents a novel approach in generating microwave optical signals using the inherent non-linearity of a Mach-Zehnder optical modulator. The operating principles of a Mach-Zehnder and the theoretical derivation of the proposed technique is presented. FM and  $\pi/4$  DQPSK experiments using the proposed technique demonstrate that it can indeed be used to generate and transmit optical microwave subcarrier signals at 17.4 GHz over optical fiber. A bit error ratio of  $2 \times 10^{-10}$  is measured for a  $\pi/4$  DQPSK experiment operating at 50 Mb/s using 50 km of fiber and an optical amplifier. Finally, chromatic dispersion effects in optical fiber are examined and it is concluded that the experimental system performance is dependent on the length of fiber used.



## **Acknowledgements**

I would like to thank my supervisors, Dr. Jan Conradi and Dr. Wayne Tinga, for their continual support and technical input throughout the course of this thesis project. Their thorough review of this thesis is also much appreciated. Completion of this work would not have been possible without the excellent facilities at TRLabs and special tribute must be given to Dr. Conradi for his efforts in establishing and maintaining such a state-of-the-art fiber optics research program.

I would also like to acknowledge my colleagues at TRLabs for making my graduate studies and research work at TRLabs enjoyable and productive. In particular, I would like to express my gratitude to Ben Chan, Stephen Lai, Dave Moore, Terrance Rosadiuk, Mike Seiben, Rohit Sharma, Sheldon Walklin, and Ping Wan for their assistance and many stimulating discussions.

Special recognition is given to Bob Davies for his technical advice and contribution to this thesis project; his knowledge in wireless communication systems is greatly appreciated. I also thank Dave Clegg and Jason Lamont for their help during the experimental phase of this project.

I would like to acknowledge the University of Alberta and the Government of Alberta for financially supporting me over the course of this work.

Finally, I would like to thank my family and friends for their support and encouragement which made this work possible.

This work was supported by the Natural Sciences and Engineering Research Council of Canada, Bell-Northern Research, and TRLabs through the NSERC/BNR/TRLabs Industrial Research Chair in Fiber Optic Communications at the University of Alberta.

# **Table of Contents**

<b>1. INTRODUCTION.....</b>	<b>1</b>
1.1 CELLULAR SYSTEMS .....	1
1.2 MICROCELLULAR SYSTEMS .....	1
1.3 OPTICAL FIBER FEEDER FOR MICROCELLULAR SYSTEMS .....	3
1.4 BASIC FIBER OPTIC LINK .....	5
1.5 TECHNIQUES FOR GENERATING MMW SIGNALS ON FIBER .....	6
<i>1.5.1 Direct Modulation and Electrical Mixing .....</i>	<i>6</i>
<i>1.5.2 External Modulators .....</i>	<i>7</i>
<i>1.5.3 Optoelectronic Mixing Receiver .....</i>	<i>8</i>
<i>1.5.4 Optical Heterodyning .....</i>	<i>9</i>
<i>1.5.5 Laser Non-linearity and Indirect Optical Injection-Locking.....</i>	<i>9</i>
<i>1.5.6 External Modulator Non-linearity.....</i>	<i>10</i>
1.6 THESIS OBJECTIVES .....	11
<b>2. EXTERNAL MODULATOR NONLINEARITIES .....</b>	<b>13</b>
2.1 THEORY OF OPERATION .....	13

2.2 MACH-ZEHNDER MODULATOR AS AN OPTOELECTRONIC MIXER AND HARMONIC GENERATOR .....	20
2.3 USE OF AN UNMODULATED CARRIER IN A MICROCELLULAR SYSTEM .....	23
<b>3. EXPERIMENTAL MODULATION FORMAT.....</b>	<b>26</b>
3.1 THE $\pi/4$ DQPSK MODULATION FORMAT.....	26
3.2 MODULATOR DESIGN.....	29
3.3 DEMODULATOR DESIGN.....	31
3.4 PERFORMANCE OF THE $\pi/4$ DQPSK MODULATION FORMAT .....	34
<b>4. EXPERIMENTAL SETUP AND COMPONENT ANALYSIS.....</b>	<b>38</b>
4.1 FM EXPERIMENTAL SETUP .....	38
4.2 DQPSK EXPERIMENTAL SETUP.....	40
4.3 RF COMPONENTS.....	43
<i>4.3.1 Amplifiers.....</i>	<i>43</i>
<i>4.3.2 Filters.....</i>	<i>44</i>
<i>4.3.3 Mixers .....</i>	<i>44</i>
<i>4.3.4 <math>\pi/4</math> DQPSK Modulator .....</i>	<i>45</i>
<i>4.3.5 <math>\pi/4</math> DQPSK Demodulator.....</i>	<i>47</i>
4.4 OPTICAL COMPONENTS.....	48

<i>h-Zehnder Switch</i> .....	49
<i>trization Controller</i> .....	50
<i>ical Amplifier</i> .....	50
<i>ical Fiber</i> .....	54
<i>tdetector</i> .....	54
ANALYSIS.....	54
<b>MENTAL RESULTS AND DISCUSSIONS</b> .....	<b>57</b>
PERIMENTS .....	57
TERIZATION OF $\pi/4$ DQPSK MODULATOR/DEMODULATOR.....	64
PSK EXPERIMENTS.....	67
<i>periment #1: Maximum Transmission without Fiber and EDFA</i> .....	69
<i>periment #2: Maximum Transmission with 25 km Fiber</i> .....	77
<i>periment #3: Minimum Transmission without Fiber and EDFA</i> .....	81
<i>periment #4: Maximum Transmission with 50 km Fiber and EDFA</i> .....	85
<i>periment #5: BER vs. Optical Loss Measurement</i> .....	90
<i>periment #6: Dispersion Experiment</i> .....	93

<b>6. CONCLUSIONS .....</b>	<b>96</b>
6.1 THESIS REVIEW .....	96
6.2 FUTURE IMPROVEMENT AND RESEARCH .....	99
<b>LIST OF REFERENCES.....</b>	<b>101</b>
<b>APPENDIX A: DIGITAL CELLULAR SYSTEM STANDARDS .....</b>	<b>105</b>
<b>APPENDIX B: DIGITAL CORDLESS PHONE STANDARDS .....</b>	<b>106</b>
<b>APPENDIX C: <math>\pi/4</math> DQPSK MODULATOR DESIGN .....</b>	<b>107</b>
<b>APPENDIX D: <math>\pi/4</math> DQPSK DEMODULATOR DESIGN.....</b>	<b>115</b>
<b>APPENDIX E: SCHEMATIC DIAGRAMS.....</b>	<b>117</b>

## **List of Tables**

Table 1: QPSK Phase Assignment.....	27
Table 2: $\pi/4$ DQPSK Decision Variables .....	34
Table 3: Amplifier Specifications .....	43
Table 4: Filter Specifications .....	44
Table 5: Mixer Specifications.....	45
Table 6: Experimental Settings and Results for Experiment #1 .....	70
Table 7: Noise Contribution for Experiment #1 .....	74
Table 8: Experimental Settings and Results for Experiment #2 .....	77
Table 9: Noise Contribution for Experiment #2 .....	80
Table 10: Experimental Settings and Results for Experiment #3 .....	81
Table 11: Noise Contribution for Experiment #3 .....	85
Table 12: Experimental Settings and Results for Experiment #4 .....	85
Table 13: Noise Contribution for Experiment #4 .....	90
Table 14: Optical Loss Settings.....	93
Table 15: Experimental Results for Experiment #6.....	95
Table 16: Digital Cellular System Standards.....	105
Table 17: Digital Cordless Telephone Standards.....	106

Table 18: Logical State Assignment .....	109
Table 19: Differential Encoder Next State Table.....	110
Table 20: Normalized I/Q Current Levels .....	111
Table 21: DAC Code Word Assignment .....	111
Table 22: DAC Code Word Truth Table .....	112

## **List of Figures**

Figure 1: Optical Fiber Feeder for Microcellular Systems .....	5
Figure 2: Basic Fiber Optic Link .....	6
Figure 3: Direct Modulation with Two Fiber Links .....	7
Figure 4: Fiber Optic Link Using External Modulator .....	8
Figure 5: Mach-Zehnder External Modulator .....	13
Figure 6: Mach-Zehnder Modulator Normalized Power Transfer Function.....	17
Figure 7: Mach-Zehnder as a Linear Modulator .....	18
Figure 8: Mach-Zehnder Non-linear Operation .....	19
Figure 9: Using Mach-Zehnder Nonlinearities in a Microcellular System.....	25
Figure 10: QPSK Phase States.....	27
Figure 11: $\pi/4$ DQPSK Phase Transition.....	29
Figure 12: Simplified $\pi/4$ DQPSK Modulator Block Diagram .....	30
Figure 13: Simplified $\pi/4$ DQPSK Demodulator Block Diagram .....	31
Figure 14: $\pi/4$ DQPSK Error Performance.....	36
Figure 15: FM Experimental Setup Block Diagram .....	40
Figure 16: $\pi/4$ DQPSK Experimental Setup Block Diagram .....	42
Figure 17: Down converter Block Diagram.....	42



Figure 18: $\pi/4$ DQPSK Modulator Block Diagram .....	46
Figure 19: $\pi/4$ DQPSK Demodulator Block Diagram .....	48
Figure 20: ETEK 2 X 2 Switch Configuration .....	50
Figure 21: Erbium Doped Fiber Amplifier Block Diagram .....	51
Figure 22: Unmodulated Carrier at 16.4 GHz (no fiber, no EDFA) .....	59
Figure 23: Spectrum of the RF Drive at 4.1 GHz (Signal Generator Output) .....	59
Figure 24: FM Signal at 17.35 GHz (no fiber, no EDFA) .....	60
Figure 25: FM Signal at 18.3 GHz (no fiber, no EDFA) .....	60
Figure 26: Simulated FM Spectrum Normalized to 50 kHz Centered at 17.35 GHz .....	61
Figure 27: Simulated FM Spectrum Normalized to 50 kHz Centered at 18.3 GHz .....	62
Figure 28: Unmodulated Carrier at 16.4 GHz (using 20 km of fiber and an EDFA) .....	63
Figure 29: FM Signal at 17.35 GHz (using 20 km of fiber and an EDFA) .....	63
Figure 30: FM Signal at 18.3 GHz (using 20 km of fiber and an EDFA) .....	64
Figure 31: Characterization of $\pi/4$ DQPSK MODEM Block Diagram .....	65
Figure 32: Performance of $\pi/4$ DQPSK MODEM .....	66
Figure 33: $\pi/4$ DQPSK Modulating Signal at 5.1 GHz .....	72
Figure 34: $\pi/4$ DQPSK Spectrum at 17.4 GHz (no fiber, no EDFA) .....	72
Figure 35: Unmodulated Carrier at 16.4 GHz (no fiber, no EDFA) .....	73
Figure 36: Down-converted Spectrum at 1.0 GHz (no fiber, no EDFA) .....	73

Figure 37: Eye Diagrams for Decision Variables (no fiber, no EDFA).....	76
Figure 38: $\pi/4$ DQPSK Spectrum at 17.4 GHz (with 25 km fiber, no EDFA).....	78
Figure 39: Unmodulated Carrier at 16.4 GHz (with 25 km fiber, no EDFA).....	79
Figure 40: Down-converted Spectrum at 1.0 GHz (with 25 km fiber, no EDFA).....	79
Figure 41: Eye Diagrams for Decision Variables (with 25 km fiber, no EDFA) .....	80
Figure 42: $\pi/4$ DQPSK Spectrum at 17.4 GHz (no fiber, no EDFA) .....	83
Figure 43: Unmodulated Carrier at 16.4 GHz (no fiber, no EDFA) .....	83
Figure 44: Down-converted Spectrum at 1.0 GHz (no fiber, no EDFA).....	84
Figure 45: Eye Diagrams for Decision Variables (no fiber, no EDFA).....	84
Figure 46: $\pi/4$ DQPSK Spectrum at 17.4 GHz (with 50 km fiber and EDFA) .....	88
Figure 47: Unmodulated Carrier at 16.4 GHz (with 50 km fiber and EDFA).....	88
Figure 48: Down-converted Spectrum at 1.0 GHz (with 50 km fiber and EDFA).....	89
Figure 49: Eye Diagrams for Decision Variables (with 50 km fiber and EDFA).....	89
Figure 50: Experimental Setup for BER vs. Optical Loss Measurement .....	91
Figure 51: BER Performance vs. SNR .....	93
Figure 52: Differential Encoder State Diagram .....	109

## List of Symbols

$\alpha$	Mach-Zehnder modulator normalized RF input drive amplitude at $f_{RF}$
$\beta$	Mach-Zehnder normalized RF input drive amplitude at $f_{RF} + f_{IF}$
$\bar{\beta}$	average propagation constant for the Mach-Zehnder modulator arms
$\beta_1, \beta_2$	propagation constants for the two Mach-Zehnder modulator arms
$\Delta\beta$	difference in propagation constant between the two arms
$\Delta f$	bandwidth in frequency
$\Delta\lambda$	bandwidth in wavelegnth
$\Delta_n$	phase difference between successive symbols for a $\pi/4$ DQPSK signal
$\varepsilon$	Mach-Zehnder modulator normalized DC bias
$\phi$	optical carrier phase
$\phi_n$	phase modulation constant for a $\pi/4$ DQPSK signal
$\gamma_b$	signal to noise ratio per bit per quadrature channel
$\eta$	detector quantum efficiency
$\lambda$	optical wavelength
$\nu$	optical frequency
$\omega_c$	carrier angular frequency
$\omega_o$	optical angular frequency
$B_N$	electrical noise equivalent bandwidth
$B_o$	optical bandwidth
$c$	speed of light
$C$	carrier power per quadrature channel
$e_{in}(t)$	Mach-Zehnder modulator input electric field in time domain
$E_b$	bit energy
$E_{in}$	Mach-Zehnder modulator input electric field amplitude
$CNR$	carrier to noise ratio
$e_{out}(t)$	Mach-Zehnder modulator output electric field in time domain

$E_{S_{in}}$	Mach-Zehnder modulator input electric field complex amplitude
$E_{S_{out}}$	Mach-Zehnder modulator output electric field complex amplitude
$F$	noise figure
$f_b$	bit rate
$f_{IF}$	intermediate frequency
$f_{RF}$	radio frequency
$f_s$	symbol rate
$G$	EDFA Gain
$g(t)$	pulse shape of base band signal
$h$	Planck's constant $6.6252 \times 10^{-34}$ J · s
$I_k$	$k$ -th order modified Bessel function
$I_n$	in-phase decision variable
$I_{out}(t)$	detected photocurrent
$i_{shot}^2$	shot noise current spectral density
$i_{sig-sp}^2$	signal-spontaneous beat noise current spectral density
$i_{RIN}^2$	RIN noise current spectral density
$i_{sp-sp}^2$	spontaneous-spontaneous beat noise current spectral density
$i_{th}^2$	thermal noise current spectral density
$J_n$	$n$ -th order Bessel function
$k$	Mach-Zehnder modulator insertion loss in amplitude
$K$	Mach-Zehnder modulator insertion loss in power
$L$	optical transmission loss in power
$N$	total single-sided noise power
$N_o$	single-sided power spectral density of Gaussian noise
$N_{sp}$	spontaneous emission factor
$P_b$	probability of bit error
$P_d$	detected signal power at the photodiode
$P_{EDFA}$	EDFA input optical power
$P_{in}$	Mach-Zehnder modulator peak input power

$P_{in\,rms}$	Mach-Zehnder modulator peak input rms power amplitude
$P_{out}(t)$	Mach-Zehnder modulator output power
$P_{out\,rms}(t)$	Mach-Zehnder modulator output rms power
$P_{sp}$	spontaneous emission power
$q$	electron charge
$Q(a, b)$	Marcum Q function
$Q_n$	quadrature decision variable
$\Re$	photodiode responsivity
$RIN$	relative intensity noise factor for the laser source
$SNR$	signal to noise ratio
$s(t)$	received $\pi/4$ DQPSK signal
$T$	room temperature
$T_b$	bit period
$T_s$	symbol period
$V(t)$	RF driving voltage to the Mach-Zehnder modulator
$V_\pi$	Mach-Zehnder modulator half wave voltage
$x(t)$	in-phase output signal of phase selector in $\pi/4$ DQPSK modulator
$y(t)$	quadrature output signal of phase selector in $\pi/4$ DQPSK modulator

# **1. Introduction**

## **1.1 Cellular Systems**

Demand for wireless personal communication systems is escalating rapidly worldwide. Wireless personal communication systems are attractive because they allow their users to be connected to other services and to reach anyone on the system anywhere. The widely used cellular telephone provides this mobility by allowing its users to be connected to the public telephone network transparently as long as the cellular telephones are within its service area. The microcellular system promises to be a potential solution to the rising demand for mobile communications.

## **1.2 Microcellular Systems**

Current mobile telephone systems in operation contain expensive base stations and large antenna towers. "Cellular system" is the terminology adopted for the mobile telephone system because the total coverage area is divided into cells. There is a base station associated with each cell which serves to connect any cellular phone user within that cell to the public telephone network. Cellular division of coverage area facilitates two functions. First, since the mobile telephone system operates in a limited UHF frequency band near 900 MHz, the cellular system allows for reuse of frequencies (channels) between cells that are not adjacent to each other. In other words, while it is necessary to assign different channels to adjacent cells to avoid interference, it is possible to reuse the same channels at a distant cell where the interfering signals are sufficiently attenuated. Second, the cellular system guarantees that the base stations are relatively close to the users; this serves to reduce the power consumption, and hence the size, of the portable phones since they do not have to radiate at a high power level to reach the base stations. Conventional base stations are very costly because they contain all the radio frequency (RF) equipment (modulator, demodulator, transmitter, and receiver) as well as the system

control circuitry. Large antenna towers are required to provide enough radio coverage for each cell since the cells are typically limited to be no smaller than 1 km radius due to zoning regulations, economics, and other factors [1].

As the traffic demand in a particular cell increases, system expansion in the conventional cellular system would involve the installation of more modulators and demodulators into the base station of that cell so that more channels can be assigned to carry the increasing traffic. Obviously, this cellular expansion cannot progress indefinitely as the total number of channels is depleted and fewer channels are available to be assigned to the adjacent cells. To limit the number of users per cell, the logical choice would be to decrease the size of each cell. It has been well documented [2] [3] that the microcellular system, which contains smaller cells (microcells) with several hundred meters diameter coverage area, promises effective frequency spectrum utilization and is believed to have the greatest potential for satisfying the increasing demand for mobile communications. By decreasing the cell size, the 'dead spots' encountered in a conventional cellular system can also be eliminated as there is always a base station nearby.

Two major difficulties arise in considering the design of a microcellular system. First, as the average distance between microcells shrinks, the risk of interference between distant cells increases. This problem can be remedied by operating the microcellular system in the microwave or millimeter-wave (MMW) frequency range. MMW signals are readily absorbed by oxygen and water molecules; this property can be exploited to limit the radiation range of a base station thus alleviating the risk of interference [4]. By operating in the higher frequency range, the relative bandwidth available is also higher and thus more channels can be allocated.

A second problem faced by the microcellular system is that a large number of base stations are required in order to cover a given area. For example, it has been estimated that 5000 base stations would be necessary to service the Tokyo metropolitan area [5]. For the microcellular system to be economically viable, it is very important to develop compact and simple base stations. A possible solution is to relocate the

modulators/demodulators and the system control circuitry away from the base stations to a central office. The base stations must then be connected to the central office via a “feeder” network which carries the calls (in the form of MMW signals) to and from the base stations. Advances in optical fiber technology, specifically in the area of subcarrier multiplexing for cable television applications [6] [7], have given fiber optic systems the capability of carrying a large number of channels on a single fiber; this qualifies fiber optic technology as a potential feeder for microcellular systems. Other desirable features of optical fiber systems, such as low attenuation, excellent frequency response, ease of installation, small physical size, and immunity from electro-magnetic interference, makes it a preferred transmission medium for the feeder network [8].

### **1.3 Optical Fiber Feeder for Microcellular Systems**

A block diagram for a simple microcellular system based on an optical fiber feeder network is shown in Figure 1. Note that all of the control circuitry and modulators/demodulators are concentrated at the central office. As calls (RF signals) from cellular phones are received by the base station, they are converted into RF modulated optical signals at the base station and transmitted to the central office where they are converted back to electrical signals for processing. Similarly, calls from the central office are converted into electrical signals at the base station and then radiated through the antenna.

Several advantages can be identified for this system [9]:

1. All of the switching functions, such as connection to the public telephone system or to another cellular phone, are performed at the central office; this simplifies traffic control processing as all of the RF signals are concentrated at the central office.
2. The base stations are now simple optical/electrical and electrical/optical converters that can be economically constructed. The reduced complexity also allows the base stations to be small in physical dimensions so that they can be easily installed.



3. A large number of radio signals can be transmitted for more than 20 km without repeaters since the fiber feeder has low loss and wide bandwidth.
4. The system can accommodate changes in modulation schemes or carrier frequency assignments for individual cells as the optical feeder is transparent to all radio signals.
5. By using electronic frequency division multiplexing or optical wavelength division multiplexing techniques, the optical feeder can share fiber cables with other fiber based systems such as cable television.
6. When used in conjunction with a spectrum delivery switch [10], which assigns channels dynamically to microcells depending on traffic demand, the blocking probability of the system (the probability of a call failing to be connected due to lack of available channels) can be greatly reduced.

The use of an optical fiber feeder for a UHF mobile radio system has been analyzed and demonstrated [11]. However, as described in Section 1.1, microwave and millimeter-wave (MMW) frequencies are more suitable to microcellular applications due to their inherent atmospheric absorption property and bandwidth availability. As a result, various techniques for generating optical signals modulated at MMW frequencies have been investigated.

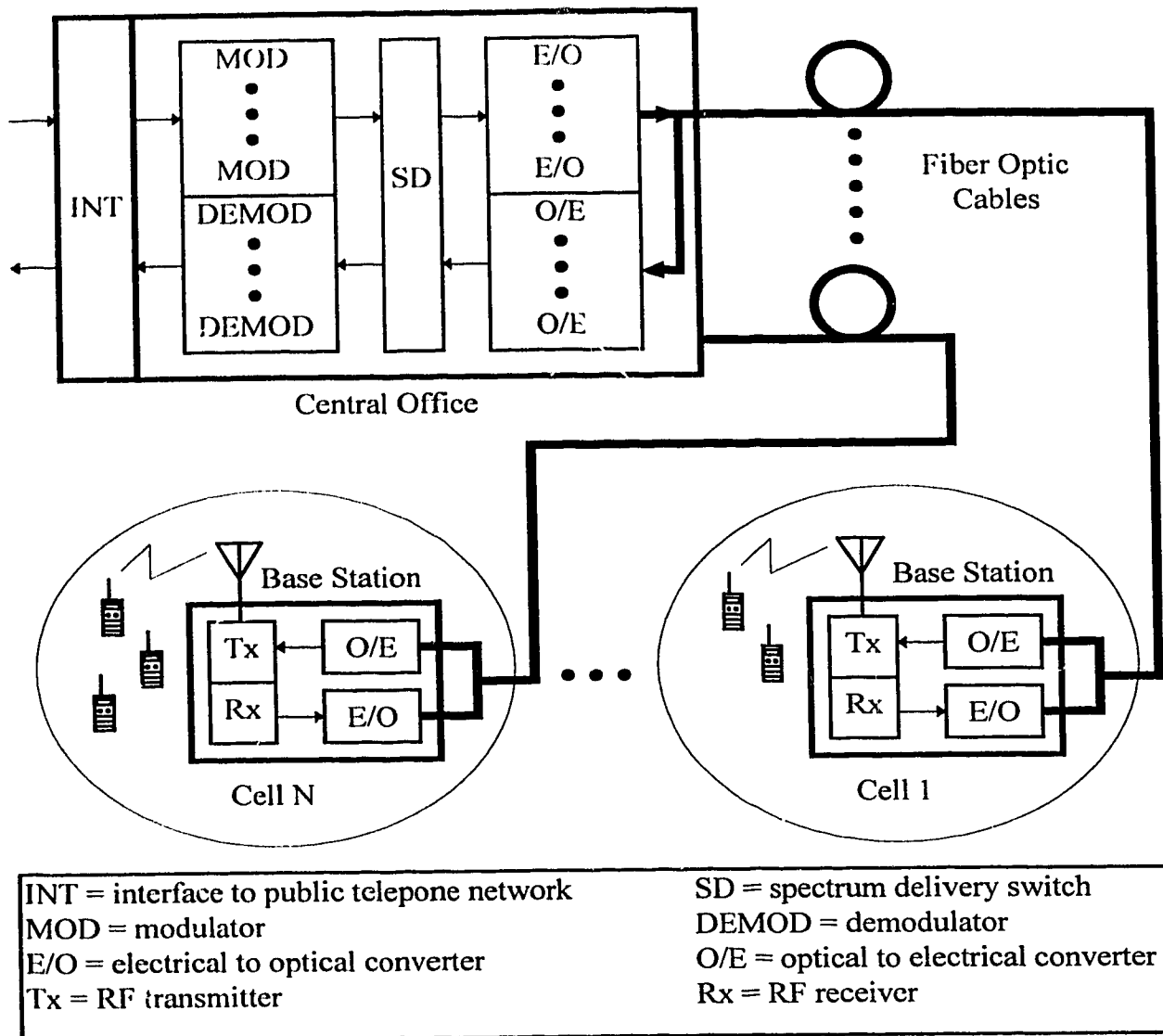


Figure 1: Optical Fiber Feeder for Microcellular Systems

## 1.4 Basic Fiber Optic Link

A basic fiber optic link consists of a laser diode, optical fiber, and a photodetector. Figure 2 illustrates a basic fiber optic link. The laser diode produces an optical signal whose output intensity is directly proportional to the applied bias current. The optical fiber is basically an optical wave guide which confines the propagation of the optical signal within the fiber. Finally, the photodetector is essentially an optical to electrical converter: it transforms the optical signal into an electrical signal.

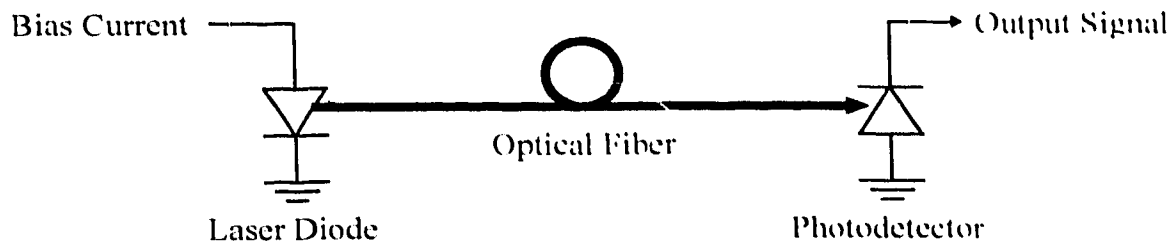


Figure 2: Basic Fiber Optic Link

## 1.5 Techniques for Generating MMW Signals on Fiber

Many techniques for the generation of MMW optical signals have been published. The following sections summarize some of these major techniques.

### 1.5.1 Direct Modulation and Electrical Mixing

The output power of laser diodes is directly related to their input bias current, hence laser diodes can be directly modulated by varying the bias current to produce a modulated optical signal [12]. However, a laser diode's frequency response is limited by its relaxation oscillation frequency, which is typically less than 20 GHz for high speed commercial devices. It is therefore presently not possible to directly modulate a laser at higher MMW frequencies. In addition, when a laser diode is modulated, the line width of the output optical signal will be broadened (a phenomenon known as “chirp”); this can drastically reduce the transmission distance in dispersive fiber. Hence even at lower MMW frequencies, the transmission performance and system dynamic range are still limited by the modulated laser diode, therefore rendering direct modulation unsuitable for long distance and wide band feeder networks.

Instead of directly modulating a laser with a modulated MMW signal, it is possible to transmit the information signal (at base band frequencies) and the MMW carrier separately using two laser diodes, optical fiber links and photodetectors (see Figure 3). The information signals and MMW carrier are then detected separately and can be mixed together using a MMW mixer producing the desired RF output. The advantage of this

configuration is that each link can be optimized separately from the other for each particular frequency and bandwidth. The dynamic range of this system is significantly superior to a simple single link configuration. The added component requirement is one of the main drawbacks of the double link system.

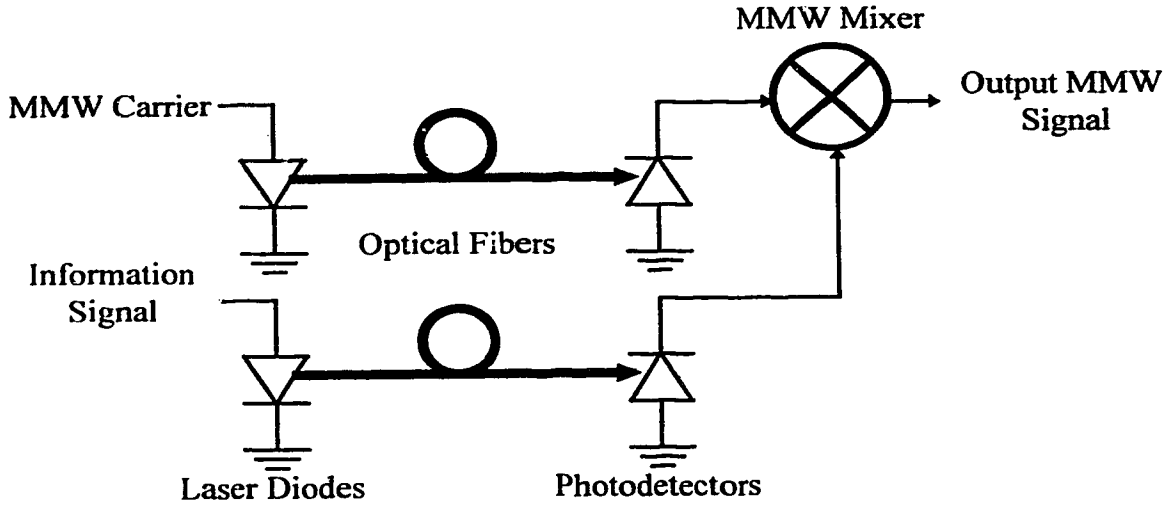


Figure 3: Direct Modulation with Two Fiber Links

### 1.5.2 External Modulators

As discussed in the previous section, direct modulation of laser diodes cannot be utilized in the direct generation of high frequency MMW signals due to the lasers' limited frequency response and chirping effect. Extensive research has been done in the area of external modulators having bandwidths of up to 50 GHz [13]. An optical external modulator can be viewed as a mixer in the optical domain: it multiplies an optical signal with an electrical signal and produces their product along with other harmonic terms. In optical transmission systems, an external modulator is typically used as a linear intensity modulator (see Figure 4) where the continuous wave (CW) optical signal from the laser diode is intensity modulated by the electrical modulation voltage. Since the laser diode is unmodulated, chirp is also eliminated hence the dispersion performance of fiber optic links employing external modulators are typically much better than that of the directly modulated links. Other configurations are possible such as combining direct modulation

of the laser diode with an external modulator [14], but they are still limited by the bandwidth of the external modulator or the laser diode. Most of the high performance external modulators commercially available employ the Mach-Zehnder Interferometer configuration, which is well documented [15] and will be explored in greater detail in a later section.

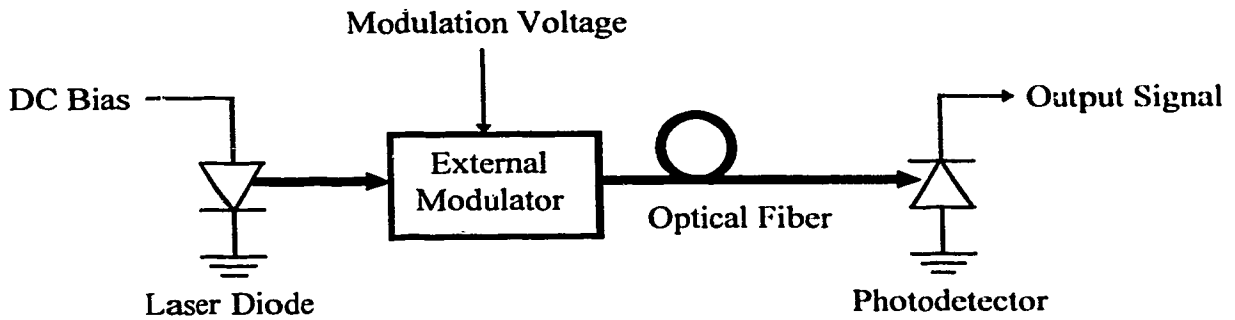


Figure 4: Fiber Optic Link Using External Modulator

### 1.5.3 Optoelectronic Mixing Receiver

In addition to performing optical to electric conversion, a photodiode can also be utilized as a MMW mixer [16]. In this approach, the laser source is directly modulated by a information carrying signal at sub-MMW frequencies; a LO signal at MMW frequencies is directly fed to the bias input of the photodiode. An approximately linear relationship exists between the bias voltage and the photodiode's responsivity (a device parameter relating the optical to electrical conversion efficiency), hence the responsivity becomes a function of the LO signal. Since the detected electrical current is obtained by multiplying the optical signal power by the photodiode's responsivity, the detected signal at sub-MMW frequencies will also be multiplied with the LO signal by the photodiode resulting in an up-converted MMW signal. This setup can eliminate the need of the high bandwidth electronic mixer as shown in Figure 3. One drawback for this implementation is the LO source requirement at the base station which complicates the base station design.

#### **1.5.4 Optical Heterodyning**

Optical heterodyning involves the transmission of the information signal modulated on one laser diode and mixing it with an unmodulated signal generated by another laser diode [17]. The modulation may be performed either directly or externally, and the difference in optical oscillation frequencies between the two laser diodes is the desired MMW frequency. It is therefore necessary to frequency lock the two laser diodes to accurately control the frequency difference. When the sum of the two signals is detected by a photodiode, which is essentially a square-law device, the difference frequency at the desired MMW frequency is produced as an output from the detector. There is virtually no limit to the difference in frequency achievable with this technique since optical frequencies are at hundreds of THz; the frequency limit is determined by the frequency response of the photodiode. The main disadvantage of this configuration is the requirement of two laser sources and the complexity in frequency locking these sources.

#### **1.5.5 Laser Non-linearity and Indirect Optical Injection-Locking**

A laser diode, similar to any ordinary diode, is a nonlinear device. This non-linearity can be exploited to generate harmonics at MMW frequencies beyond the rated bandwidth of the laser diode in combination with a square-law detector [18]. For example: when a laser diode is directly modulated by a 2 GHz signal, the harmonics at 4, 6, 8, 10 GHz can be detected. However, the use of laser non-linearity alone for the generation of high MMW frequencies is not reliable since the generation of harmonics compromises the stability and reliability of the device.

To further utilize the harmonics generated by the laser diode, the detected harmonics at MMW frequencies can be injected into an electronic oscillator (such as a FET or IMPATT oscillator [19]) so that the oscillator is locked onto one of the harmonics of the MMW signals. The term “indirect injection” is used since the optically generated harmonics are first converted to electrical signals before being injected into the oscillator. Once locked onto the harmonic frequency generated by the optical components, the oscillator can

produce a high power MMW signal at the same harmonic frequency; this optically generated harmonic can also be further up-converted to a higher frequency by the inherent non-linearity of the oscillator [19]. An obvious disadvantage of this system is the complex electronics requirement at the receiver end.

### 1.5.6 External Modulator Non-linearity

A novel approach has recently been published which utilizes the non-linearity of an external modulator to generate MMW signals above the modulator's rated bandwidth [20] [21]. The basic operation of Mach-Zehnder modulators will be presented in the next chapter. Like most electronic modulators, a Mach-Zehnder external modulator also possesses nonlinear properties. In particular, consider a sinusoidal modulating voltage described by

$$v(t) = V_{\pi}(1 + \varepsilon) + \alpha V_{\pi} \cos(\omega t), \quad \text{Eq. 1-1}$$

where  $V_{\pi}$  is a device parameter known as the half wave voltage,  $\varepsilon$  is the DC bias point normalized to  $V_{\pi}$ ,  $\alpha$  is the amplitude of the AC drive voltage normalized to  $V_{\pi}$ , and  $\omega$  is the modulating frequency. When such a signal is used to modulate an optical carrier using a Mach-Zehnder external modulator, the electric field at the external modulator output is given by [22]

$$E(t) = \cos\left\{\frac{\pi}{2} \cdot [(1 + \varepsilon) + \alpha \cdot \cos(\omega t)]\right\} \cdot \cos(\omega_o t), \quad \text{Eq. 1-2}$$

where  $\omega_o$  is the optical carrier frequency in the 200 THz range. This output characteristic is clearly non-linear. The frequency content of the output electric field can be determined by expressing (2) as a Bessel function expansion

$$\begin{aligned}
E(t) = & \frac{1}{2} \cdot J_0\left(\alpha \frac{\pi}{2}\right) \cdot \cos\left[\frac{\pi}{2} \cdot (1 + \varepsilon)\right] \cdot \cos(\omega_o t) \\
& - J_1\left(\alpha \frac{\pi}{2}\right) \cdot \sin\left[\frac{\pi}{2} \cdot (1 + \varepsilon)\right] \cdot \cos(\omega_o t \pm \omega t) \\
& - J_2\left(\alpha \frac{\pi}{2}\right) \cdot \cos\left[\frac{\pi}{2} \cdot (1 + \varepsilon)\right] \cdot \cos(\omega_o t \pm 2\omega t) \\
& + J_3\left(\alpha \frac{\pi}{2}\right) \cdot \sin\left[\frac{\pi}{2} \cdot (1 + \varepsilon)\right] \cdot \cos(\omega_o t \pm 3\omega t) \\
& + \dots
\end{aligned} \tag{Eq. 1-3}$$

It follows that by biasing the Mach-Zehnder modulator at  $V_\pi$  ( $\varepsilon = 0$ ), all the terms involving even multiples of  $\omega$  will be suppressed. Two strong components, which correspond to the Bessel function coefficients  $J_1$  and  $J_3$ , are then generated at the optical frequency  $\omega_o$  and are separated by twice the modulation drive frequency  $2\omega$  (i.e.  $3\omega - \omega = 2\omega$ ). The non-linearity of the Mach-Zehnder modulator can therefore be used to generate harmonic terms whose difference is the desired MMW frequency. When these harmonic terms are detected by a photodiode, the square-law characteristic of the photodiode beats them together to produce the desired MMW frequency.

Note that this technique is essentially identical to the optical heterodyne technique; the only difference is that only one laser source is required. The main advantage of using only one laser source, besides a lower component count requirement, is that the phase noise between the two harmonic terms is correlated and the electrical line width of the output signal can be very narrow. Although the amplitude of the harmonic terms generated by the Mach-Zehnder modulator tends to be quite low, they can still be efficiently transmitted to the base stations with the use of optical amplifiers. It has been demonstrated [23] that with the aid of optical amplifiers, high purity 60 GHz signals can be distributed to more than 1000 base stations using this technique.

## 1.6 Thesis Objectives

This thesis project involves further investigation into using the non-linearity of Mach-Zehnder external modulators to generate modulated MMW signals. One of the major drawbacks of the Mach-Zehnder non-linearity technique presented in the previous section is the hardware complexity in modulating the up-converted MMW signal at the desired



frequency. It was proposed in [24] that narrow band optical filters (with bandwidths of 10's of GHz) and an additional external modulator are required to impose modulation onto the up-converted carrier at MMW frequency. Besides the need for an extra optical modulator, the bandwidth requirement of the optical filters is also very difficult to achieve in practice, hence some of the major objectives of this thesis project are finding a method for up-converting the modulated MMW signal, transmitting and detecting this signal, and experimentally verifying the approach.

In addition to the problem in up-converting the modulated MMW signal, there is also a lack of any bit error ratio measurement using some form of digital modulation scheme for this kind of up-conversion system. Therefore another objective for this thesis project is to choose a widely accepted digital modulation format compatible with the proposed modulation technique, then perform experiments using the chosen modulation format and up-conversion technique to verify the system performance. This will also involve the design and construction of modulator/demodulator hardware required for the experiments.

In summary, this thesis project presents a technique utilizing the harmonic generation and opto-electronic mixing properties of the Mach-Zehnder modulator to up-convert modulated MMW signals. In chapter 2, the theory of operation of the Mach-Zehnder external modulator is presented, which is followed by the theoretical derivation of the up-conversion technique with modulation capability. Chapter 3 introduces the chosen modulation scheme; it also contains the modulator/demodulator design and performance analysis of the modulation format chosen for the experiment. In chapter 4, the experimental setup is presented including detailed analysis for most of the optical and electrical components used in the experiments. The noise analysis for the complete system is also included in this chapter. The experimental results and discussions are presented in chapter 5. A preliminary experiment is presented to verify the validity of the proposed system; this is followed by six experiments using the chosen modulation format and various optical configurations. Finally, chapter 6 concludes this thesis project with a short review and possible areas of research to further investigate this work.

## 2. External Modulator Nonlinearities

### 2.1 Theory of Operation

Operation of the Mach-Zehnder modulator is based on the electro-optic properties of special materials. The electro-optic properties of a material refer to the change in refractive index of a material under the influence of an electrical field. Materials having higher electro-optic coefficients, that is, their refractive indices are highly sensitive to the applied electric field, are more suitable to form the substrate of a Mach-Zehnder modulator because the required electrical drive voltage to produce a given change in refractive index can be minimized. Lithium Niobate, or  $\text{LiNbO}_3$ , is commonly used in Mach-Zehnder modulators due to its high electro-optic coefficient. A number of laboratories have optimized the processing procedure of Lithium Niobate and it is commercially available in up to 7.5 cm diameter wafers.

The basic physical structure of a Mach-Zehnder modulator is illustrated in Figure 5.

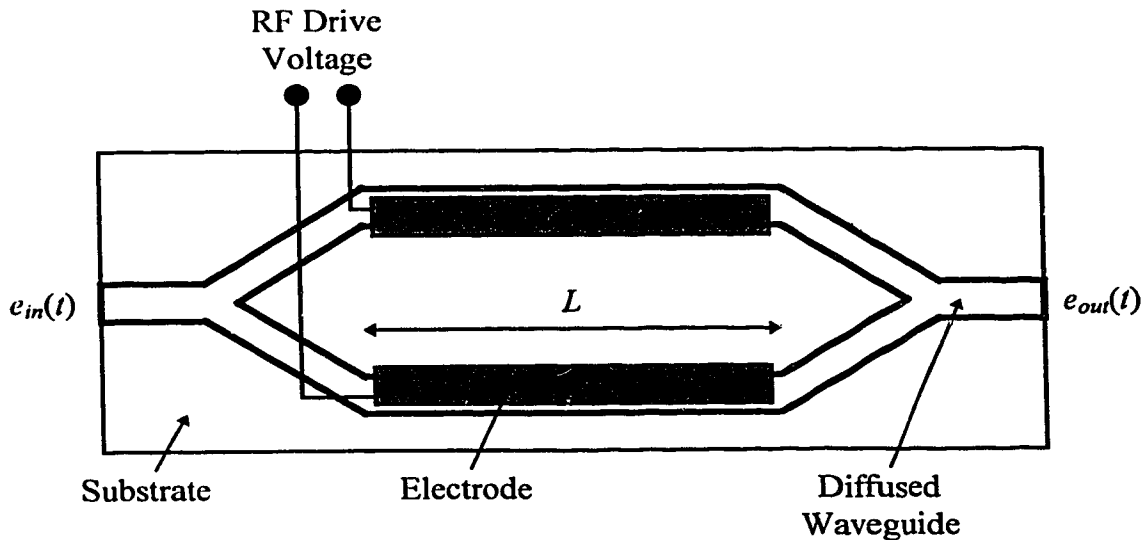


Figure 5: Mach-Zehnder External Modulator

In this figure,  $e_{in}(t)$  and  $e_{out}(t)$  are the time varying electric field expressions of the input and output optical signals, respectively. The optical signal entering the modulator is confined within the waveguide region due the higher refraction index of the waveguide as compared to the substrate. This higher refractive index is usually created by diffusing titanium atoms into the LiNbO<sub>3</sub> substrate. After entering the modulator, the optical signal is split into two arms via the input 3 dB coupler. The electrodes expose the two arms to different drive voltages resulting in different refractive indices in the two arms. Since the propagation coefficient (  $\beta_1$  and  $\beta_2$  ) of a waveguide is directly related to the refractive index, the two optical signals will travel at different velocities through the two arms. The two signals are recombined at the output coupler, and depending on the applied drive voltage, in-phase and out-of-phase addition of the two optical signals can be achieved.

To further examine the operation of the Mach-Zehnder modulator, let's define the complex amplitude of the input electric field of the optical signal as  $E_{sin} = E_m e^{j\phi}$ . Where  $E_m$  is the amplitude and  $\phi$  is the phase of the input light wave. In optical systems employing external modulators, the input optical signals can be assumed to be free of any amplitude or phase fluctuation since the optical sources are unmodulated. The unmodulated light from the optical sources are fed into the external modulators so that chirping effects can be minimized. In this case,  $E_m$  takes on a constant amplitude and  $\phi$  is zero, giving  $E_{sin} = E_m$  as the complex amplitude of the input electric field. The actual time varying input electric field can be obtained by taking  $\text{Re}\{E_{sin} \cdot e^{j\omega_o t}\}$ , where  $\omega_o$  is the optical angular frequency (in hundreds of THz) of the input light wave. This gives

$$e_{in}(t) = E_m \cos(\omega_o t) \quad \text{Eq. 2-1}$$

It is also convenient to define the Root Mean Squared (RMS) input power as

$$\begin{aligned} P_{in,rms} &= \overline{e_{in}^2(t)} \\ &= \frac{1}{2} E_m^2 \end{aligned} \quad \text{Eq. 2-2}$$

Returning to complex notation, for constant drive voltages, the two arms can be treated as waveguides with different propagation coefficients  $\beta_1$  and  $\beta_2$ . Assuming that the input and output couplers are ideal (that is, they split and combine the optical signal equally), and the transmission losses in the arms are identical, we can write the following expression for the output electric field's complex amplitude

$$\begin{aligned} E_{S_{out}} &= \frac{1}{2} E_{in} k \left[ e^{-j\beta_1 L} + e^{-j\beta_2 L} \right] \\ &= \frac{1}{2} E_{in} k \left[ \cos(\beta_1 L) + \cos(\beta_2 L) - j \left[ \sin(\beta_1 L) + \sin(\beta_2 L) \right] \right], \end{aligned} \quad \text{Eq. 2-3}$$

where  $L$  is the length of the device and the factor  $k$  is introduced to account for the transmission loss through the modulator. That is,  $k$  specifies the amount of attenuation experienced by an optical signal when equal drive voltages are applied to the two arms. Under this condition, the optical signals in the two arms travel at the same velocity and will recombine in phase at the output coupler.

By using the identities

$$\begin{aligned} \sin(x) + \sin(y) &= 2 \sin\left(\frac{x+y}{2}\right) \cos\left(\frac{x-y}{2}\right) \\ \cos(x) + \cos(y) &= 2 \cos\left(\frac{x+y}{2}\right) \cos\left(\frac{x-y}{2}\right), \end{aligned} \quad \text{Eq. 2-4}$$

Eq. 2-3 becomes

$$E_{S_{out}} = E_{in} k \cos[\Delta\beta L] e^{-j\bar{\beta}L} \quad \text{Eq. 2-5}$$

where

$$\bar{\beta} = \frac{\beta_1 + \beta_2}{2}, \text{ and } \Delta\beta = \frac{\beta_1 - \beta_2}{2}. \quad \text{Eq. 2-6}$$

The actual output electric field can be obtained by taking the real part of Eq. 2-5 multiplied by  $e^{j\omega_o t}$  giving

$$e_{out}(t) = E_{in} k \cos[\Delta\beta(t)L] \cos[\omega_o t - \bar{\beta}(t)L] \quad \text{Eq. 2-7}$$

Note that for the above equation, time dependency is introduced to the variables  $\Delta\beta$  and  $\bar{\beta}$ . This is done because both  $\beta_1$  and  $\beta_2$  are functions of time when time varying input electrical drives are applied to the electrodes.

Now let

$$\Delta\beta(t)L = \frac{\pi V(t)}{2V_\pi} \quad \text{Eq. 2-8}$$

where  $V(t)$  is the signal voltage applied across the electrodes. This definition relates the amount of phase shift encountered by an optical signal through the modulator to the signal voltage.  $V_\pi$  is a device parameter which specifies the bias voltage at which the optical signals in the two arms are delayed by exactly  $\pi$  radians in phase. When recombined under this condition, these two optical signals will interfere with each other destructively resulting in complete extinction at the output of the external modulator.

Substituting Eq. 2-8 into Eq. 2-7 results in

$$e_{out}(t) = E_{in} k \cos\left[\frac{\pi V(t)}{2V_\pi}\right] \cos(\omega_o t - \bar{\beta}(t)L). \quad \text{Eq. 2-9}$$

Note that  $\bar{\beta}(t)$  is usually assumed to be constant in the above equation; this requires that  $\beta_1(t)$  and  $\beta_2(t)$  change by the same amount but with opposite signs. This assumption is valid because most Mach-Zehnder modulators are constructed in this way so that frequency chirping associated with the modulators can be eliminated [25]. Therefore,  $\bar{\beta}(t)L = \bar{\beta}L$  represents a constant optical phase term which can be left out in the analysis.

The output power (normalized to 1 Ohm) is related to the output electric field by

$$\begin{aligned}
P_{out}(t) &= |E_{out}(t)|^2 \\
&= E_{out}(t) \cdot E_{out}^*(t) \\
&= E_{in}^2 k^2 \cos^2\left(\frac{\pi V(t)}{2V_\pi}\right) \\
&= \frac{P_{in} K}{2} \left[ 1 + \cos\left(\frac{\pi V(t)}{V_\pi}\right) \right]
\end{aligned}
\tag{Eq. 2-10}$$

where  $P_{in} = (E_{in})^2$  is the peak input power to the external modulator and  $K = k^2$  specifies the insertion power loss of the modulator. Finally, the RMS output power of the Mach-Zehnder modulator can be expressed as

$$P_{out\,rms}(t) = \frac{P_{in\,rms} K}{2} \left[ 1 + \cos\left(\frac{\pi V(t)}{V_\pi}\right) \right]. \tag{Eq. 2-11}$$

The output power response is plotted in the following figure.

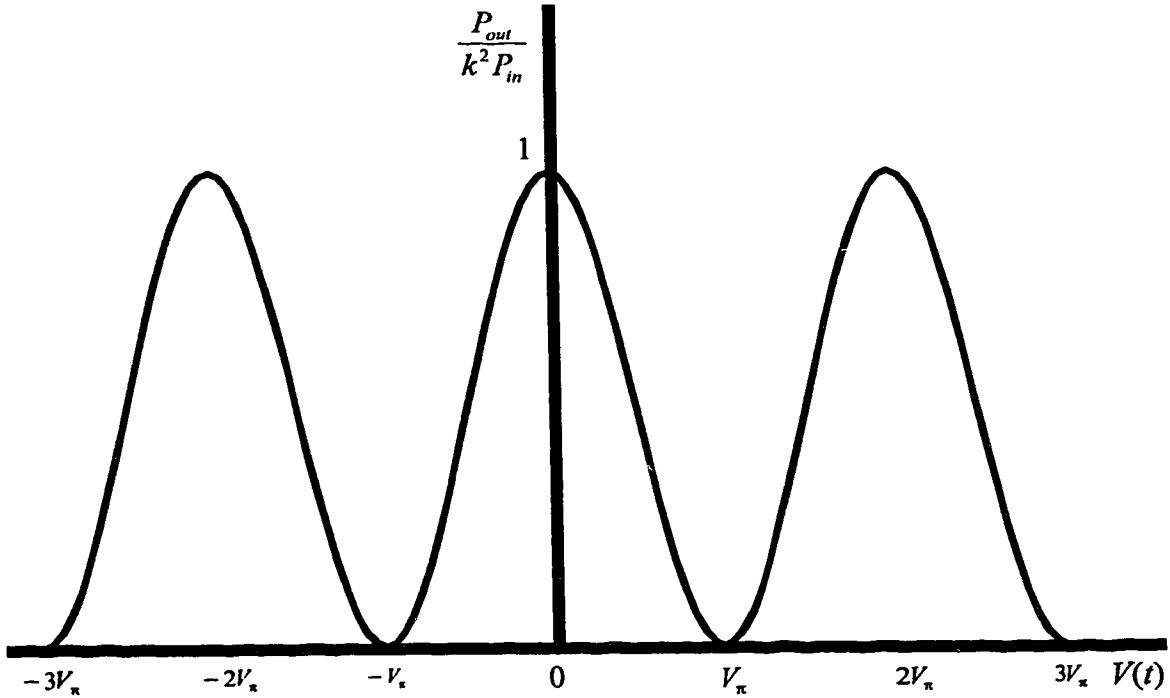


Figure 6: Mach-Zehnder Modulator Normalized Power Transfer Function

Note that the power transfer function is periodic with a period of  $2V_\pi$ , hence  $V_\pi$  defines the half period of the modulator response. In most system applications, the Mach-Zehnder external modulators are used as linear amplitude modulators by setting the bias at the center of the approximately linear region near  $V_\pi/2$ . The following figure demonstrates a typical bias condition in a fiber optic system.

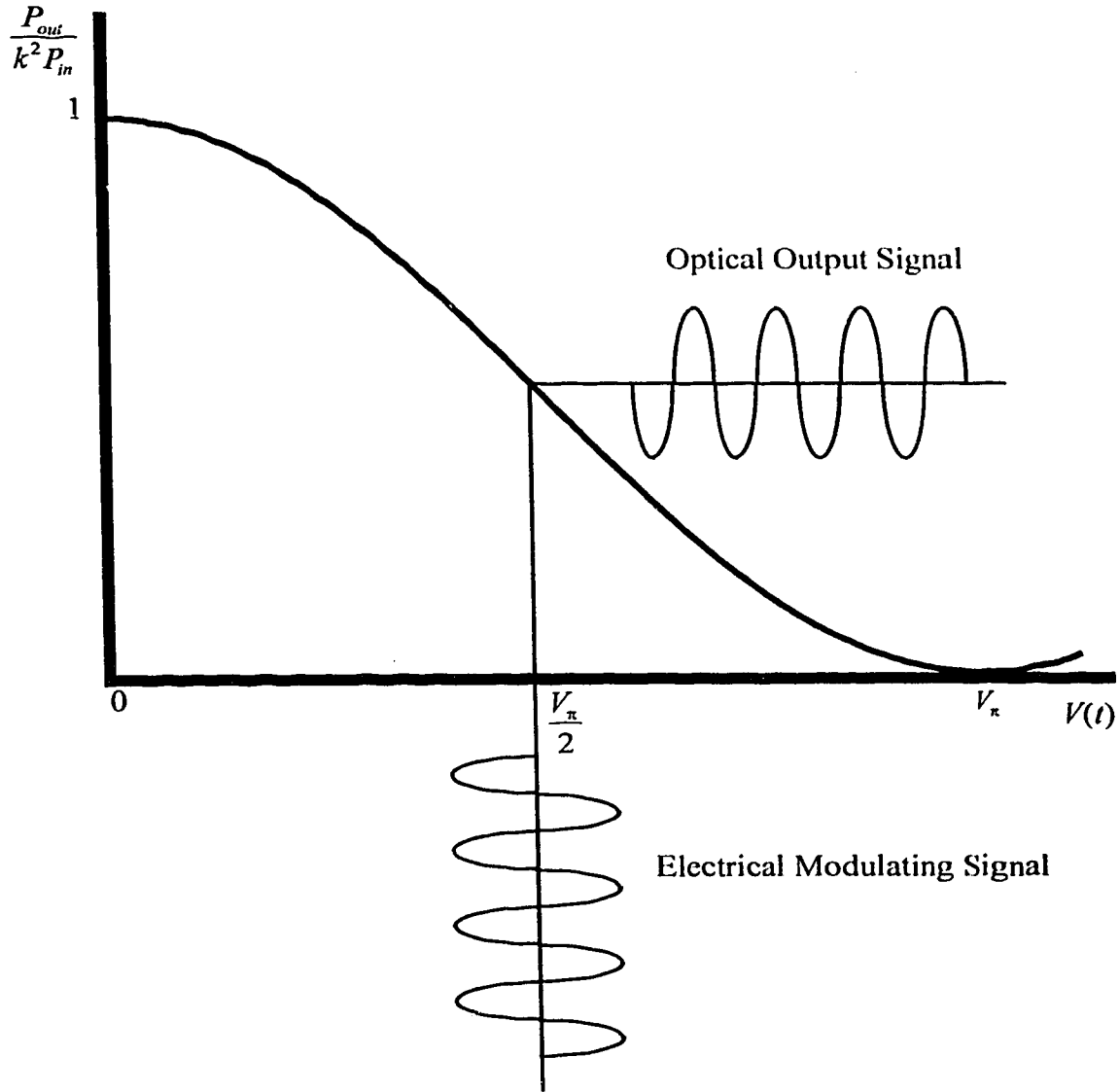


Figure 7: Mach-Zehnder as a Linear Modulator

As long as the input modulating signal,  $V(t)$ , is kept relatively small, the linear approximation is valid. However, it is evident that when the amplitude of  $V(t)$  approaches  $V_\pi/2$ , the output power response becomes highly non-linear. Furthermore, if the DC bias point is set to any integer multiple of  $V_\pi$ , the effects of non-linearity will be even more pronounced as illustrated in Figure 8. The use of this non-linearity for generating harmonics and mixing effects will be discussed in detail in the next section.

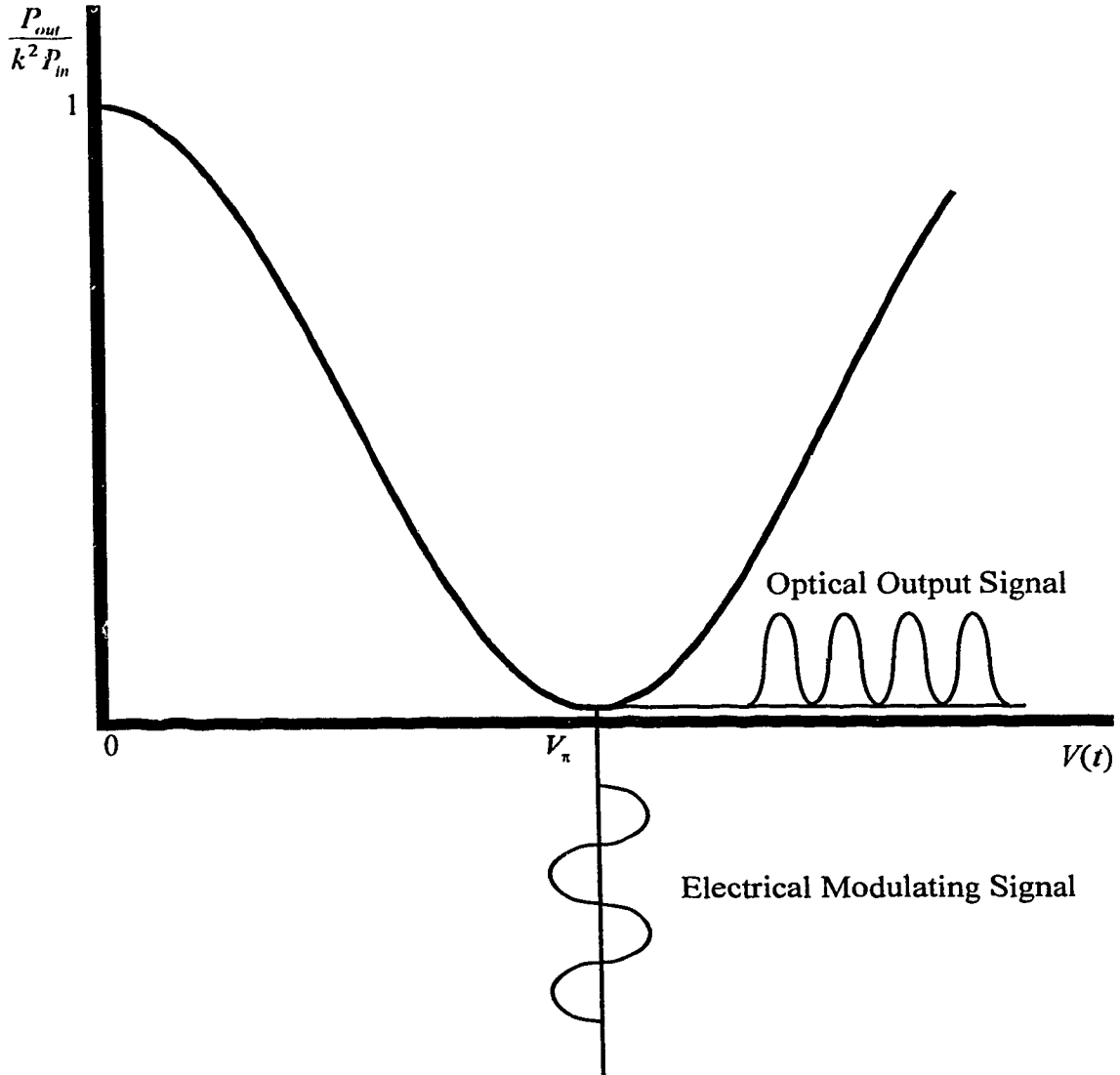


Figure 8: Mach-Zehnder Non-linear Operation



## 2.2 Mach-Zehnder Modulator as an Optoelectronic Mixer and Harmonic Generator

Generally, the non-linearity of any device can be exploited to perform mixing and harmonic generation functions to some extent. The Mach-Zehnder modulator, which has a nonlinear transfer characteristic as shown in Eq. 2-10, can also be used as a harmonic generator and an opto-electric mixer simultaneously. Using Eq. 2-10 as the input to a length of optical fiber, and ignoring fiber dispersion, the detected photo-current at the end of the fiber can be written as

$$\begin{aligned} I_{out}(t) &= L \cdot \Re \cdot P_{out}(t) \\ &= \frac{K \cdot L \cdot P_{in} \cdot \Re}{2} \left[ 1 + \cos \left[ \frac{\pi V(t)}{V_{\pi}} \right] \right], \end{aligned} \quad \text{Eq. 2-12}$$

where  $\Re$  is the responsivity of the photodiode (in A/W) and  $L$  is the net optical loss from the output of the modulator to the photodiode. In order to utilize the modulator as a mixer, we must feed in at least two signals at different frequencies. By defining these signals as an unmodulated signal at frequency  $f_{RF}$  and a phase or frequency modulated signal at carrier frequency  $f_{RF} + f_{IF}$ , the total input signal to the modulator can be written as

$$\begin{aligned} V(t) &= V_{\pi}(1 - \varepsilon) \\ &+ \alpha V_{\pi} \cos[2\pi(f_{RF} + f_{IF})t + m(t)] + \beta V_{\pi} \cos(2\pi f_{RF}t). \end{aligned} \quad \text{Eq. 2-13}$$

The first term in the above equation is the DC bias voltage which sets the operating point of the Mach-Zehnder modulator; for example, if  $\varepsilon = 0, \pm 1, \pm 2 \dots$ , etc., the modulator is biased at the maximum or minimum transmission point. The second term is the angle (phase or frequency) modulated signal at the frequency  $f_{RF} + f_{IF}$  with its amplitude defined by the constant  $\alpha$  normalized to  $V_{\pi}$ .  $m(t)$  is the angle modulating base band signal which is to be recovered in the final output. The third term is an unmodulated carrier at the frequency  $f_{RF}$  with its amplitude defined by  $\beta$ , which is also normalized to

$V_{\pi}$ . Substituting Eq. 2-13 into Eq. 2-12, setting  $\varepsilon = 0, \pm 1, \pm 2 \dots$ , (i.e. the modulator is biased at its maximum or minimum transmission points), and carrying out the expansion yields

$$I_{out}(t) = \frac{KLP_m \mathfrak{R}}{2} \left[ \begin{aligned} &1 \pm \sin\left[\pi\alpha \cos(2\pi(f_{RF} + f_{IF1})t + m(t))\right] \sin\left[\pi\beta \cos(2\pi f_{RF}t)\right] \\ &\mp \cos\left[\pi\alpha \cos(2\pi(f_{RF} + f_{IF1})t + m(t))\right] \cos\left[\pi\beta \cos(2\pi f_{RF}t)\right] \end{aligned} \right].$$

Eq. 2-14

In the above equation, the top signs are used when  $\varepsilon = 0, \pm 2, \pm 4, \dots$  (biased at minimum transmission points), whereas the bottom signs are used when  $\varepsilon = \pm 1, \pm 3, \pm 5, \dots$  (biased at maximum transmission points). Now identities involving Bessel functions can be used to expand each of the composite trigonometric functions in the above equation into an infinite sum of cosines. These identities are [26]

$$\begin{aligned} \cos[x \cos(y)] &= J_0(x) - 2J_2(x)\cos(2y) + 2J_4(x)\cos(4y) - \dots \\ \sin[x \cos(y)] &= 2J_1(x)\cos(y) - 2J_3(x)\cos(3y) + 2J_5(x)\cos(5y) - \dots \end{aligned} \quad \text{Eq. 2-15}$$

The result is that each of the two products within the larger square brackets in Eq. 2-14 represent a multiplying, or mixing process involving two infinite sums. One of the sums contains harmonics of the modulated information signal while the other contains harmonics of the unmodulated carrier. In other words, the harmonics of the unmodulated carriers are used to up-convert each of the modulated information signal harmonics. This can be verified by carrying out the expansion to produce Eq. 2-16.

$$I_{out}(t) = \frac{kLP_{in}\Re}{2} \left[ \begin{aligned} &1 \mp J_0(\pi\alpha)J_0(\pi\beta) \\ &\pm 2J_1(\pi\alpha)J_1(\pi\beta)\cos[2\pi(f_{IF1})t + m(t)] \\ &\mp 2J_2(\pi\alpha)J_2(\pi\beta)\cos[2\pi(2f_{IF1})t + 2m(t)] \\ &\pm 2J_3(\pi\alpha)J_3(\pi\beta)\cos[2\pi(3f_{IF1})t + 3m(t)] \\ &+ \dots \\ &\pm 2J_0(\pi\alpha)J_2(\pi\beta)\cos[2\pi(2f_{RF})t] \\ &\pm 2J_1(\pi\alpha)J_1(\pi\beta)\cos[2\pi(2f_{RF} + f_{IF1})t + m(t)] \\ &\mp 2J_1(\pi\alpha)J_3(\pi\beta)\cos[2\pi(2f_{RF} - f_{IF1})t - m(t)] \\ &\pm 2J_2(\pi\alpha)J_0(\pi\beta)\cos[2\pi(2f_{RF} + 2f_{IF1})t + 2m(t)] \\ &\pm 2J_2(\pi\alpha)J_4(\pi\beta)\cos[2\pi(2f_{RF} - 2f_{IF1})t - 2m(t)] \\ &\mp 2J_3(\pi\alpha)J_1(\pi\beta)\cos[2\pi(2f_{RF} + 3f_{IF1})t + 3m(t)] \\ &\mp 2J_3(\pi\alpha)J_5(\pi\beta)\cos[2\pi(2f_{RF} - 3f_{IF1})t - 3m(t)] \\ &+ \dots \\ &\mp 2J_4(\pi\alpha)J_4(\pi\beta)\cos[2\pi(4f_{RF})t] \\ &\mp 2J_1(\pi\alpha)J_3(\pi\beta)\cos[2\pi(4f_{RF} + f_{IF1})t + m(t)] \\ &\pm 2J_1(\pi\alpha)J_5(\pi\beta)\cos[2\pi(4f_{RF} - f_{IF1})t - m(t)] \\ &\mp 2J_2(\pi\alpha)J_2(\pi\beta)\cos[2\pi(4f_{RF} + 2f_{IF1})t + 2m(t)] \\ &\mp 2J_2(\pi\alpha)J_6(\pi\beta)\cos[2\pi(4f_{RF} - 2f_{IF1})t - 2m(t)] \\ &\mp 2J_3(\pi\alpha)J_1(\pi\beta)\cos[2\pi(4f_{RF} + 3f_{IF1})t + 3m(t)] \\ &\pm 2J_3(\pi\alpha)J_7(\pi\beta)\cos[2\pi(4f_{RF} - 3f_{IF1})t - 3m(t)] \\ &+ \dots \end{aligned} \right]$$

Eq. 2-16

Again the top signs in the above equation are used when the Mach-Zehnder modulator is biased at its minimum transmission points; the bottom signs are used when it is biased for maximum transmission. Note that unmodulated carriers are indeed present at even multiples of  $f_{RF}$ ; only even harmonics are present because the DC bias point was chosen to be any integer multiple of  $V_\pi$  (by setting  $\varepsilon = 0, \pm 1, \pm 2, \dots$  etc.) which leads to the suppression of all odd harmonics. In addition, the above equation shows that the information signals are offset from the even harmonics of the unmodulated carrier at

harmonic intervals of  $f_{IF1}$ . This allows for an extra degree of flexibility in increasing the transmission frequency of the system. Since  $m(t)$  is simply multiplied by a constant in each of the information terms after the up conversion, Eq. 2-16 also suggests that it is possible to send any kind of phase (or frequency) modulated signal at frequencies of  $2f_{RF} \pm nf_{IF1}$ ,  $4f_{RF} \pm nf_{IF1}$ , etc. One of the properties inherent in this modulation technique is that the transmission bandwidth of the information signal increases linearly with the harmonic order  $n$  since the angle modulation index (the constant in front of  $m(t)$ ) is multiplied by  $n$  as shown in Eq. 2-16. A physical limitation to this technique is the decreasing signal amplitude achievable for higher harmonics or larger  $n$ . This is a result of the fact that the effective amplitude modulation index for a particular carrier is given by the combination of Bessel function terms in equation Eq. 2-16. By choosing their arguments appropriately the power levels at the desired frequencies can be optimized. Furthermore, by selecting  $f_{RF} + f_{IF1}$  to be near the upper limit of the frequency response of the Mach-Zehnder modulator, a linearly modulated (frequency or phase modulated) signal at  $nf_{IF1} + (2 \text{ or } 4)f_{RF}$  with significant output power can be obtained. On the other, if the signal at  $f_{IF1}$  is amplitude modulated, the modulating signal would appear as a modulation superimposed on the amplitude coefficient  $\alpha V_\pi$  in Eq. 2-13, which in turn would appear in the optical output embedded in the arguments of the appropriate Bessel functions and hence would be significantly distorted. Angle modulation formats also have significant signal-to-noise ratio advantages over amplitude modulation. For these reasons, and compatibility with existing and emerging UHF cellular formats, two forms of angle modulation are used in the experiments described later in this thesis.

## 2.3 Use of an Unmodulated Carrier in a Microcellular System

Figure 9 demonstrates how both the modulated and unmodulated carriers can be used in a microcellular system. This block diagram is similar to the one proposed in [27] but is significantly simpler in that only one external modulator and no narrow band optical filters at the laser and its signal sidebands frequencies are required, hence optical

hardware requirements are significantly reduced. From the block diagram of Figure 9 we see that by using wavelength division multiplexers (WDM), bi-directional transmission is possible with the use of two lasers at different wavelengths. One optical carrier, at optical frequency  $f_{o1}$  (for example: at 1300 nm), carries the signal from the central office to the base station; the other carrier at optical frequency  $f_{o2}$  (for example: at 1550 nm) carries the signal in the reverse direction. Alternatively, the WDM couplers could be replaced by optical circulators in which case lasers within the operating wavelength range of the circulators could be used.

As explained in the previous section, the non-linear transfer characteristic of the Mach-Zehnder modulator can be used to generate both an unmodulated carrier as well as the information signal at frequencies near the even harmonics of the original input signals. At the base station, the diplexer filters out the information signal at the desired frequency, which is chosen to be at  $4f_{RF} + f_{IF1}$  in the experiments. This signal is then radiated through the antenna and received by the portable phone user. The other output of the diplexer permits the unmodulated carrier at  $4f_{RF}$  to pass to the local oscillator port of the electrical mixer. This unmodulated carrier is used to down-convert the return signal transmitted by the portable phone to  $f_{IF2}$  at the MMW mixer thereby providing remote control of the base station transmitter and receiver frequencies by the central office. Since the return signal does not have to be radiated at microwave or millimeter-wave frequencies at the central office,  $f_{IF2}$  can be chosen to fall within the bandwidth of the laser diode at  $f_{o2}$  and the laser can be directly modulated in the up-link direction. Using this technique the base station can be constructed with minimal and low cost hardware.

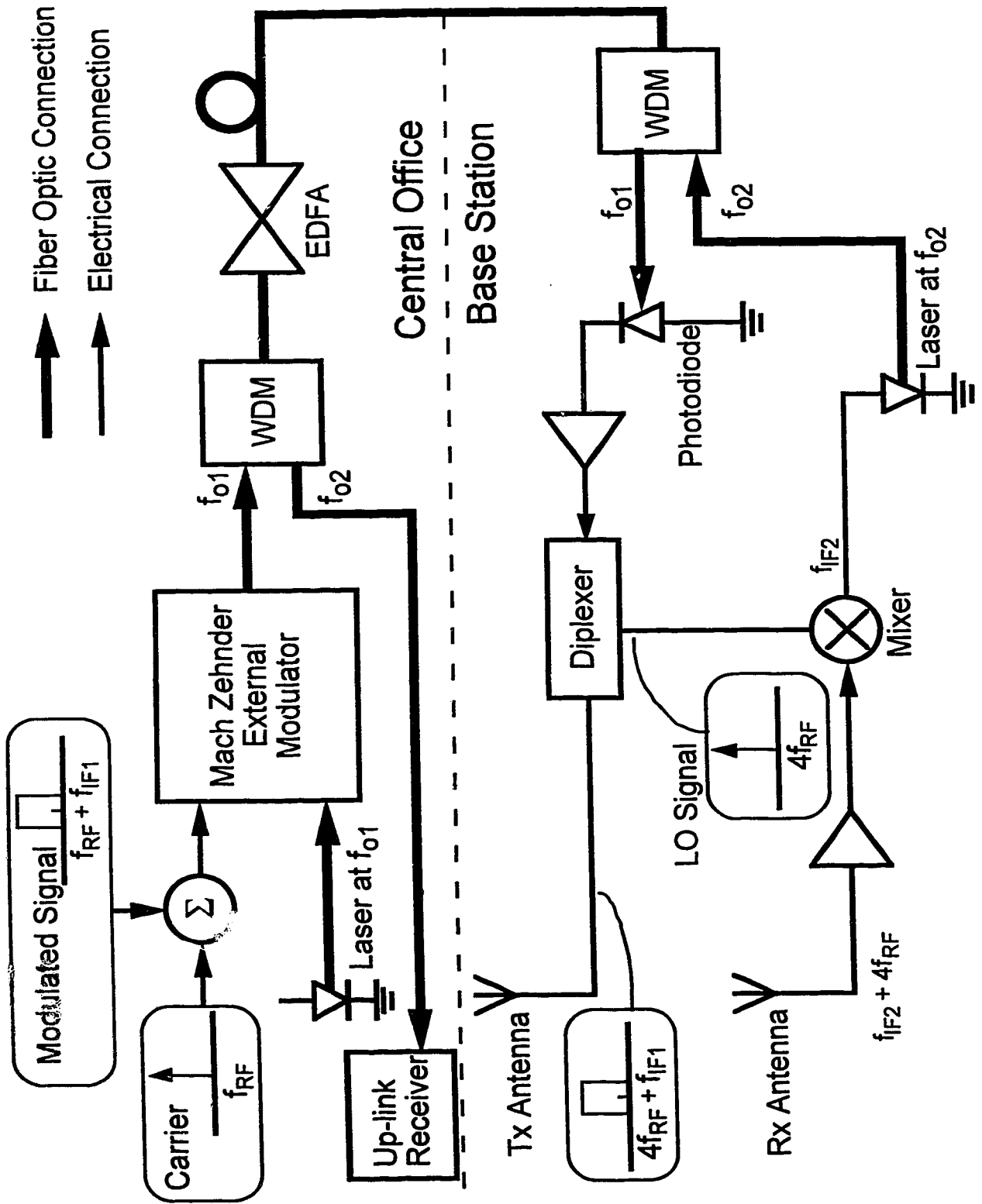


Figure 9: Using Mach-Zehnder Nonlinearities in a Microcellular System

### **3. Experimental Modulation Format**

In the previous chapter, Eq. 2-16 demonstrates that any form of angle modulation is preserved using the proposed technique to generate MMW signals on optical fiber. In order to fully characterize the noise performance on the system, a digital modulation scheme must be chosen to facilitate bit error ratio versus signal to noise measurements. For this thesis project,  $\pi/4$  Differential Quaternary Phase Shift Keying (DQPSK) was selected based on three reasons. First, it is a form of angle modulation, and hence can theoretically be transmitted using the proposed technique without any distortion. Second, it is a modulation format widely adopted in the wireless mobile industry due to its bandwidth efficiency. It is currently employed in second generation digital cellular standards such as North America Digital Cellular and Personal Digital Cellular (Japan) as well as in the Personal Hand Phone indoor cordless phone standard in Japan. This has resulted in many publications on the performance of  $\pi/4$  DQPSK in UHF and microwave radio channels. And finally, as will be shown later in this chapter, this modulation scheme allows for differential demodulation which simplifies the design of the demodulator by eliminating the need for carrier recovery circuits.

#### **3.1 The $\pi/4$ DQPSK Modulation Format**

First introduced and demonstrated by P. A. Baker [28], the  $\pi/4$  DQPSK modulation scheme was used for “high-speed” transmission of data over telephone lines in 1962. It is a special form of digital multi-phase modulation capable of carrying two bits of information during each symbol period without increasing the bandwidth requirement as compared to a binary angle modulation scheme. Let’s begin by writing the expression for a multi-phase digital signal as:

$$\begin{aligned}
s(t) &= \text{Re} \left\{ A \sum_n g(t - nT_s) \cdot e^{j(\phi_n + \omega_c t)} \right\} \\
&= A \cos \left[ \omega_c t + \sum_n \phi_n g(t - nT_s) \right]
\end{aligned}$$

Eq. 3-1

where  $A$  is a constant defining the signal amplitude in volts,  $\omega_c$  is the carrier frequency in rad/s,  $T_s$  is the symbol period (i.e.  $1/T_s$  is the bit rate) in seconds and  $n$  is the total number of symbols in the digital signal.  $g(t)$  defines the pulse shape of the modulating signal and is specified by the baseband filter used in the system. For simplicity,  $g(t)$  is assumed to be a rectangular pulse with amplitude of 1 and duration of  $T_s$ . Finally,  $\phi_n$  is the phase modulation constant and can take on discrete values in the interval  $[0, 2\pi]$ . For ordinary phase modulation, a specific value of  $\phi_n$  is chosen to represent a digital symbol. For example, in Quaternary Phase Shift Keying (QPSK), where two bits of information are transmitted during each symbol period, one can make the following phase assignment.

Phase Assignment $\phi_n$	Corresponding Symbol
$\pi/4$	00
$3\pi/4$	10
$5\pi/4$	11
$7\pi/4$	01

Table 1: QPSK Phase Assignment

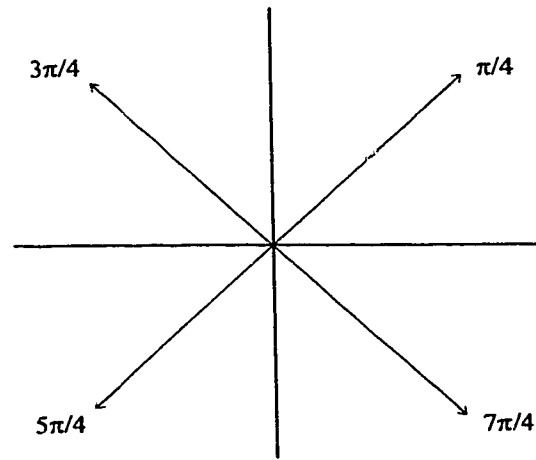


Figure 10: QPSK Phase States

Note that Gray coding is used so that each adjacent phase state differs by only one bit; this aids in eliminating the occurrence of double errors since most errors are caused by an incorrect decision between adjacent phase states. One of the major drawbacks of phase shift keying is the requirement for coherent demodulation; that is, it is necessary to recover the carrier so that the absolute phase during each symbol period can be



determined. This leads to the introduction of differentially encoded phase modulation, such as  $\pi/4$  DQPSK. In a differential modulation scheme, instead of making an absolute phase assignment, the modulation information is encoded into the phase changes between successive symbols in the modulated signal. Specifically, for  $\pi/4$  DQPSK, the phase constant  $\phi_n$  can be redefined as

$$\phi_n = \Delta_n + \phi_{n-1} \quad \text{Eq. 3-2}$$

where  $\Delta_n$  is the phase difference between successive symbols and can take on one of four values specified by  $\Delta_n = \frac{(2l-1)\pi}{4}$ ,  $l=1, 2, 3$  or  $4$ . This definition states that the absolute phase of the modulated signal sampled at a given time now depends on the symbol transmitted during the current symbol period, as well as the absolute phase during the previous symbol period. The phase assignment can also be made for  $\Delta_n$  in place of  $\phi_n$  in Table 1, hence a specific amount of phase difference between successive symbol periods corresponds to a particular transmitted symbol. To further clarify, assume that at time  $(n-1)T_s$ , the absolute phase is zero. Then according to Eq. 3-2 the absolute phase at time  $n T_s$  is now  $0 + \Delta_n$ , where  $\Delta_n$  can take on one of the four phase values in Table 1 ( $\pi/4$ ,  $3\pi/4$ ,  $5\pi/4$ , or  $7\pi/4$ ) depending on which symbol is sent. If we further assume that the symbol 00 is transmitted at time  $n T_s$ , then the absolute phase at time  $n T_s$  is now  $\pi/4$ . Similarly, the absolute phase at time  $(n+1) T_s$  will be  $\pi/4 + \Delta_{n+1}$ ; again depending on the symbol transmitted, it can take on one of four possible values ( $0$ ,  $\pi/2$ ,  $\pi$ , or  $3\pi/2$ ). Although the signal has gone through eight possible phase states, this is still a quaternary modulation scheme since during each symbol period the signal can jump to only one of four phase states, hence only 2 bits of information can be carried by each symbol. This can be further illustrated by Figure 11. As will be shown in a later section, this phase transition can be retrieved without recovering the absolute phase of the carrier.

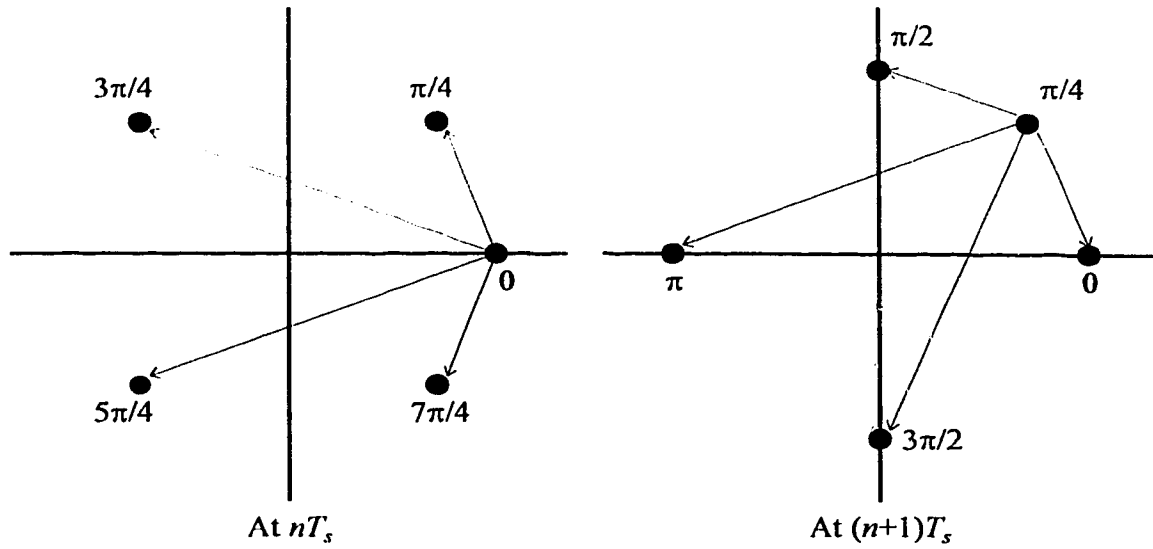


Figure 11:  $\pi/4$  DQPSK Phase Transition

### 3.2 Modulator Design

In order to generate the  $\pi/4$  DQPSK signal, let's rewrite Eq. 3-1 in its quadrature components. Using the identity

$$\cos(a + b) = \cos(a)\cos(b) - \sin(a)\sin(b), \quad \text{Eq. 3-3}$$

Eq. 3-1 can be written as

$$\begin{aligned} s(t) &= A \cos(\omega_c t) \cos \left[ \sum_n \phi_n g(t - nT_s) \right] \\ &\quad - A \sin(\omega_c t) \sin \left[ \sum_n \phi_n g(t - nT_s) \right] \\ &= x(t) \cos(\omega_c t) + y(t) \sin(\omega_c t) \end{aligned} \quad \text{Eq. 3-4}$$

where

$$x(t) = A \cos \left[ \sum_n \phi_n g(t - nT_s) \right]$$

$$y(t) = -A \sin \left[ \sum_n \phi_n g(t - nT_s) \right].$$

Eq. 3-5

Now if we have a binary digital input bit stream  $b_n$  with a bit period of  $T_b$ , where  $T_b = 2T_s$  for a quaternary system, the modulator illustrated in the following block diagram can be used to generate  $\pi/4$  DQPSK signals.

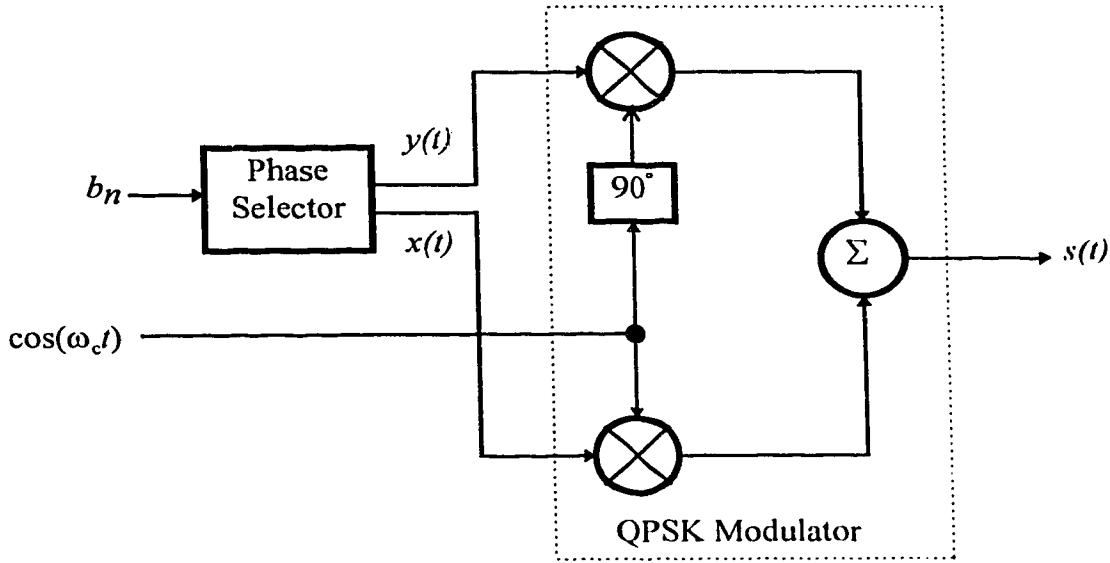


Figure 12: Simplified  $\pi/4$  DQPSK Modulator Block Diagram

The phase selector in the above diagram receives the binary bit stream  $b_n$  as input, splits the binary bit stream into two parallel bit streams to form the input symbols, performs differential encoding according to Eq. 3-2, then generates the required quadrature components  $x(t)$  and  $y(t)$  after the manner of Eq. 3-5. This quadrature implementation of the modulator is used because the multipliers (mixers), phase shifter and summer (power combiner) are commercially available in a single package as a QPSK Modulator, hence only the phase selector needs to be designed for the modulator. The design of the phase selector will be presented in a later section.

### 3.3 Demodulator Design

It is possible to demodulate a DQPSK signal without retrieving the carrier phase when a differential demodulator is employed. The following diagram depicts such a demodulator. Note that the mixers, phase shifter and power splitter are commercially available in a single package as an I/Q (In Phase/Quadrature) Phase Detector.

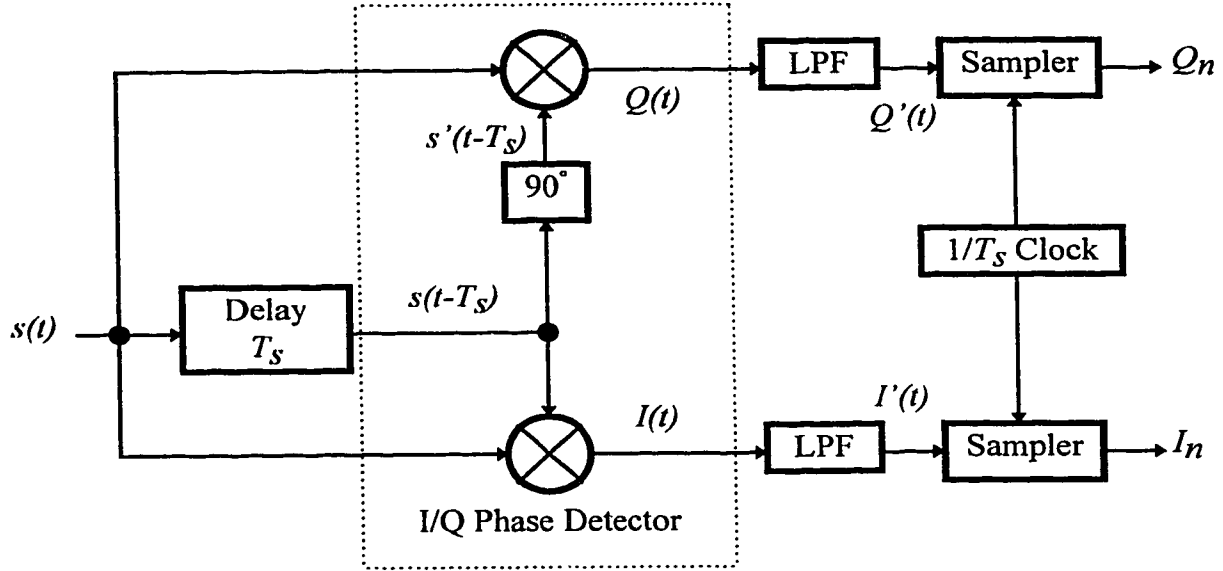


Figure 13: Simplified  $\pi/4$  DQPSK Demodulator Block Diagram

The operation of the demodulator is now presented. Using the definition for  $s(t)$  from Eq. 3-1, the signal after the  $T_s$  delay is

$$s(t - T_s) = B \cos \left[ \omega_c (t - T_s) + \sum_n \phi_n g(t - nT_s - T_s) \right], \quad \text{Eq. 3-6}$$

where a new positive amplitude constant  $B$  is introduced to account for attenuation through the delay block. Let's first focus on the in-phase ( $I$ ) side of the demodulator. At the output of the  $I$  mixer, we have

$$\begin{aligned}
I(t) &= s(t)s(t - T_s) \\
&= A \cos \left[ \omega_c t + \sum_n \phi_n g(t - nT_s) \right] \\
&\quad \cdot B \cos \left[ \omega_c (t - T_s) + \sum_n \phi_n g(t - nT_s - T_s) \right] \\
&= \frac{AB}{2} \begin{bmatrix} \cos[f(t)] \cos[2\omega_c t - \omega_c T_s + f(t - T_s)] \\ + \cos[f(t)] \cos[\omega_c T_s - f(t - T_s)] \\ - \sin[f(t)] \sin[2\omega_c t - \omega_c T_s + f(t - T_s)] \\ - \sin[f(t)] \sin[\omega_c T_s - f(t - T_s)] \end{bmatrix},
\end{aligned} \tag{Eq. 3-7}$$

where

$$\begin{aligned}
f(t) &= \sum_n \phi_n g(t - nT_s) \\
f(t - T_s) &= \sum_n \phi_{n-1} g(t - nT_s - T_s) = \sum_n \phi_{n-1} g(t - nT_s).
\end{aligned} \tag{Eq. 3-8}$$

The simplification on the second line of Eq. 3-8 is based on the fact that  $g(t)$  is the same for every symbol. By setting the cutoff frequency of the low pass filters to filter out signals at  $2\omega_c$ , Eq. 3-7 becomes

$$I'(t) = \frac{AB}{2} \begin{bmatrix} \cos[f(t)] \cos[\omega_c T_s - f(t - T_s)] \\ - \sin[f(t)] \sin[\omega_c T_s - f(t - T_s)] \end{bmatrix}. \tag{Eq. 3-9}$$

Using equation Eq. 3-3, Eq. 3-9 can be further simplified as

$$I'(t) = \frac{AB}{2} \cos[f(t) - f(t - T_s) + \omega_c T_s]. \tag{Eq. 3-10}$$

From Eq. 3-8,  $f(t) - f(t - T_s) = \sum_n (\phi_n - \phi_{n-1}) g(t - nT_s)$ . So when we sample the signal in Eq. 3-10 in the middle of  $g(t)$  and at the rate of once every  $T_s$ , the following decision variable is obtained (note that  $g(t)$  was defined as a rectangular pulse with amplitude equal to 1)

$$I_n = \frac{AB}{2} \cos[\Delta_n + \omega_c T_s]. \quad \text{Eq. 3-11}$$

Recall that  $\Delta_n$  was defined in Eq. 3-2 as a measure of the phase difference between successive symbols, hence this decision variable indeed contains the necessary information to decode the differentially encoded signal.

Now let's turn our attention to the quadrature ( $Q$ ) side of the demodulator. At the output of the phase shifter the following signal is generated

$$s'(t - T_s) = -C \sin \left[ \omega_c(t - T_s) + \sum_n \phi_n g(t - nT_s - T_s) \right]. \quad \text{Eq. 3-12}$$

Again a new positive amplitude constant  $C$  is introduced to account for change in amplitude through the phase shifter. At the output of the  $Q$  mixer, we have

$$\begin{aligned} Q(t) &= s(t)s'(t - T_s) \\ &= -A \cos \left[ \omega_c t + \sum_n \phi_n g(t - nT_s) \right] \\ &\quad \times C \sin \left[ \omega_c(t - T_s) + \sum_n \phi_n g(t - nT_s - T_s) \right] \\ &= -\frac{AC}{2} \begin{bmatrix} \cos[f(t)] \sin[2\omega_c t - \omega_c T_s + f(t - T_s)] \\ + \cos[f(t)] \sin[-\omega_c T_s + f(t - T_s)] \\ - \sin[f(t)] \cos[\omega_c T_s - f(t - T_s)] \\ + \sin[f(t)] \cos[2\omega_c t - \omega_c T_s + f(t - T_s)] \end{bmatrix}. \end{aligned} \quad \text{Eq. 3-13}$$

Following the same procedure and using the same assumptions as for the in-phase case, the following decision variable can be obtained for the quadrature side

$$Q_n = \frac{AC}{2} \sin[\Delta_n + \omega_c T_s]. \quad \text{Eq. 3-14}$$

Using the same Gray-encoded phase state assignment for QPSK in Table 1 as the differential phase assignment for  $\Delta_n$ , and assuming that  $\omega_c T_s = k2\pi$ , where  $k$  is an integer, the resulting decision variable values are tabulated in Table 2.

Symbol	$\Delta_n$	$\frac{2I_n}{AB}$	$\frac{2Q_n}{AC}$
00	$\pi/4$	$1/\sqrt{2}$	$1/\sqrt{2}$
10	$3\pi/4$	$-1/\sqrt{2}$	$1/\sqrt{2}$
11	$7\pi/4$	$-1/\sqrt{2}$	$-1/\sqrt{2}$
01	$5\pi/4$	$1/\sqrt{2}$	$-1/\sqrt{2}$

Table 2:  $\pi/4$  DQPSK Decision Variables

From this table it is apparent that simple voltage comparators and logic circuits can be used at the output of the samplers to correctly decode the transmitted symbol. The hardware implementation of the differential demodulator will be discussed in greater details in a later section.

### 3.4 Performance of the $\pi/4$ DQPSK Modulation Format

As mentioned before, the  $\pi/4$  DQPSK modulation format has been adopted by different cellular standards. Consequently, there is a significant amount of work in the literature dealing with the performance of  $\pi/4$  DQPSK in radio channels with special fading properties and in the presence of additive white Gaussian noise [29] [30]. In this thesis project the effect of radio channel fading will be neglected since radio propagation experiments will not be performed, and the transmission system can be assumed to have only additive white Gaussian noise. The theoretical derivation for the probability of error in  $\pi/4$  DQPSK signals in the presence of additive white Gaussian noise is quite involved and will not be presented here. Rather, the expression for the error probability is presented and details can be found in reference [31].

If we define  $\gamma_b$  as the signal to noise ratio (SNR) per bit at the input to the demodulator:

$$\gamma_b = \frac{E_b}{N_o} \quad \text{Eq. 3-15}$$

where  $E_b$  is the energy per bit of the signal and  $N_o$  is the single-sided power spectral density of the additive white Gaussian noise at the receiver, then the probability of bit error, or the bit error ratio (BER), for  $\pi/4$  DQPSK signals is

$$P_b = Q(a, b) - \frac{1}{2} I_0(ab) \exp\left[-\frac{1}{2}(a^2 + b^2)\right]$$

$$a = \sqrt{2\gamma_b \left(1 - \frac{1}{\sqrt{2}}\right)}$$

$$b = \sqrt{2\gamma_b \left(1 + \frac{1}{\sqrt{2}}\right)}$$
Eq. 3-16

where (for  $b > a > 0$ )

$$Q(a, b) = e^{-(a^2 + b^2)/2} \sum_{k=0}^{\infty} \left(\frac{a}{b}\right)^k I_k(ab)$$
Eq. 3-17

and  $I_k$  is the  $k$ -th order modified Bessel function.

Figure 14 illustrates the error performance of  $\pi/4$  DQPSK according to Eq. 3-16. Note that for second generation digital cellular systems, bit error ratios on the order of  $10^{-5}$  would be adequate for voice communications over the radio link, hence the SNR level required at the radio receiver (cellular phone) should be better than 12 dB. The received SNR at the output of the photodetector must be set at a level much higher than the 12 dB requirement after the radio link depending on the channel fading and loss characteristics. For this system, the goal is to achieve the maximum SNR at the photodetector output to produce a BER near the range of  $10^{-9}$ .



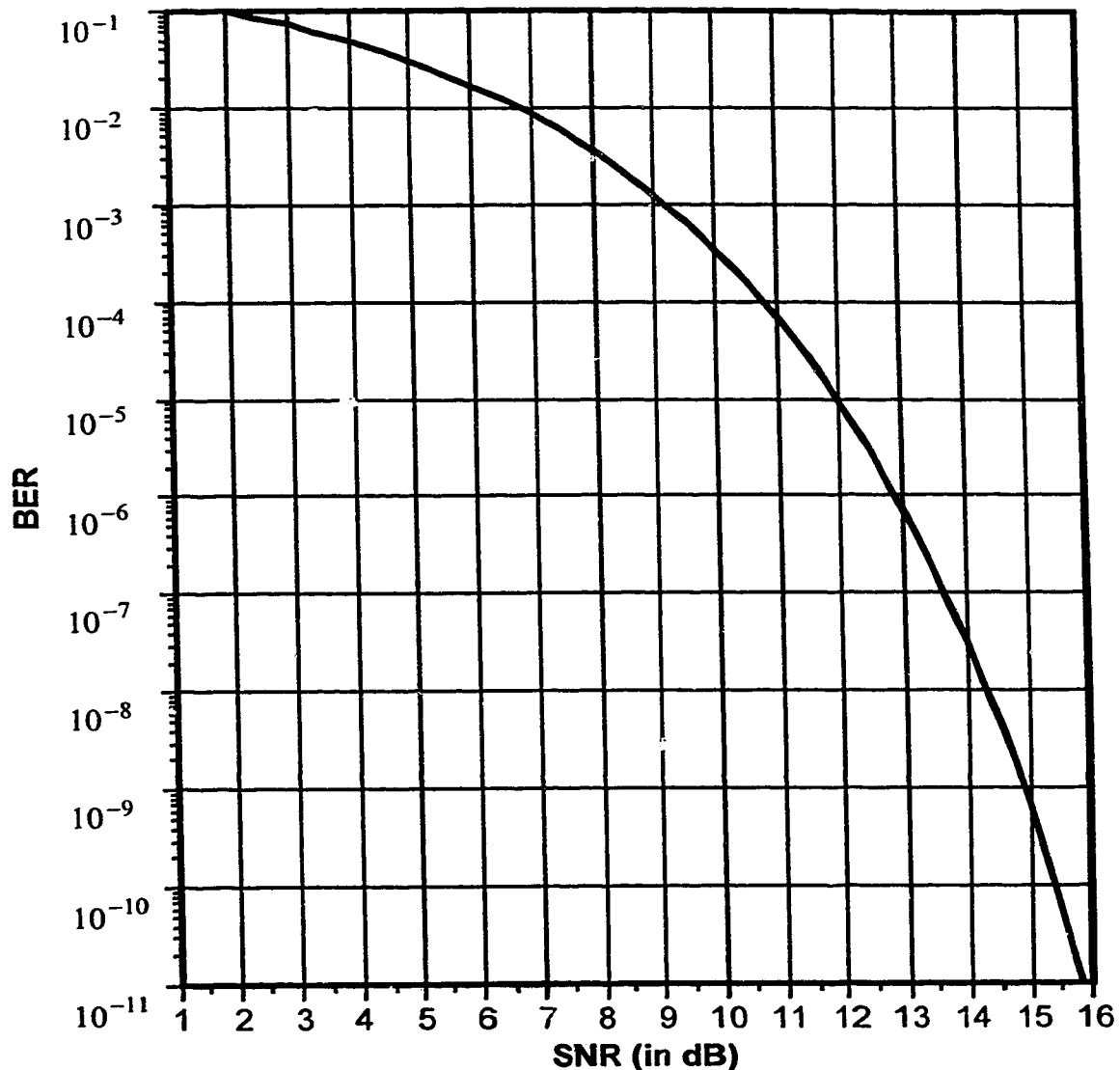


Figure 14:  $\pi/4$  DQPSK Error Performance

Instead of expressing the system performance in terms of SNR per bit, it is often more useful to relate the BER to a carrier-to-noise ratio (CNR) since most measurements are obtained using power and root-mean-squared (RMS) voltage meters in the laboratory. Eq. 3-18 can be used to transform the measured CNR to SNR per bit. Note that since the measured carrier power in the experiment is actually the sum of the power contribution from both in-phase and quadrature channels, this carrier power must be divided by 2 for the calculation of SNR per bit.

$$\begin{aligned}
E_b &= CT_b = C / 2f_b \\
N_o &= N / B_N \\
SNR &= \frac{E_b}{N_o} = \frac{C / f_b}{N / B_N} \quad , \\
SNR &= \frac{B_N}{f_b} \cdot CNR = \frac{C}{f_b N_o}
\end{aligned}
\tag{Eq. 3-18}$$

where  $C$  is the carrier power per quadrature channel,  $N$  is the total noise power,  $B_N$  is the equivalent noise bandwidth at the input of the receiver, and  $f_b$  is the bit rate of the base band binary bit stream which is related to the bit period by  $f_b = 1 / T_b$ .

## **4. Experimental Setup and Component Analysis**

### **4.1 FM Experimental Setup**

As discussed in section 2.2, the proposed frequency up-conversion technique is transparent to any form of phase or frequency modulation format. Before a complete BER experiment using  $\pi/4$  DQPSK was performed, it was decided that the system should be tested using a simple single-tone frequency modulated (FM) signal at the IF frequency ( $f_{IF}$ ) of 1 GHz because such a signal can be easily generated by a HP8642A signal generator available at TRLabs. The up-converted FM spectra can also be readily verified using a spectrum analyzer and compared with computer simulated spectra. This test was used to determine the validity of the proposed technique before a significant amount of work and capital was invested into the design and construction of a  $\pi/4$  DQPSK modulator/demodulator. Figure 15 illustrates the hardware setup for the FM experiment. This configuration is also applicable to the  $\pi/4$  DQPSK experiments by replacing the FM signal generator with the  $\pi/4$  DQPSK modulator and the spectrum analyzer with the down converter and  $\pi/4$  DQPSK demodulator; these components will be introduced in a later section.

While one of the eventual applications of this up conversion technique is for wireless networks operating in either the 20 or 50-60 GHz regions, our current experimental capabilities limit implementation to input frequencies up to around 5 GHz, but the experiments presented are intended to demonstrate the correctness of the theory and the viability of the proposed up conversion concepts. To this end, Figure 15 focuses on the use of frequencies near the fourth harmonic at 16.4 GHz of the unmodulated carrier at  $f_{RF}$ , which is chosen to be 4.1 GHz. To generate the baseband signal a 1.0 GHz carrier is frequency modulated by a 50 kHz tone, with a frequency modulation index of 1, giving a frequency deviation of 50 kHz. With  $f_{IF1}$  set to 1.0 GHz, the first up-converted information signal to appear above the fourth harmonic of  $f_{RF}$  will be at 17.4 GHz

$(4f_{RF} + f_{IF1})$ . In order to generate  $V(t)$  as defined by Eq. 2-13, a microwave mixer is used to up-convert the FM signal to  $f_{RF} + f_{IF1}$  (5.1 GHz). The up-converted FM signal is then combined with the unmodulated carrier at 4.1 GHz and the composite signal is amplified and fed to the AC input of the bias tee. Attenuators are used to adjust the amplitude constants  $\alpha$  and  $\beta$  independently so as to maximize the power in the desired harmonic in the final output. DC bias is added at the bias tee to set the operating point of the Mach-Zehnder modulator at quadrature so that only even harmonics of  $f_{RF}$  are present. The signal at the output of the bias tee constitutes  $V(t)$  as defined in Eq. 2-13, which is then fed to the Mach-Zehnder switch as the modulating voltage.

On the optical side, a 1551 nm laser source is used. The optical isolator at the output of the laser diode reduces backward reflected power into the laser. A polarization controller is also employed to adjust the polarization of light entering the Mach-Zehnder modulator to optimize its performance since the opto-electric effect of  $\text{LiNbO}_3$  crystal is highly sensitive to the orientation of the input signal's axis of polarization. Note that the 3 dB bandwidth of the Mach-Zehnder switch is approximately 7-8 GHz, and our experiment is designed to show that the amplitudes of the harmonic signals are unaffected by the modulator bandwidth, as long as the *input* signal frequencies are within the modulator bandwidth. The optical signal at the output of the Mach-Zehnder modulator is either detected immediately using a high speed PIN photodiode and then measured using a spectrum analyzer, or is amplified using an Erbium Doped Fiber Amplifier (EDFA), transmitted through 20 km of single mode fiber, detected by the PIN photodiode and electrically amplified before it is connected to the spectrum analyzer. The results of the FM experiment will be presented in the next chapter.

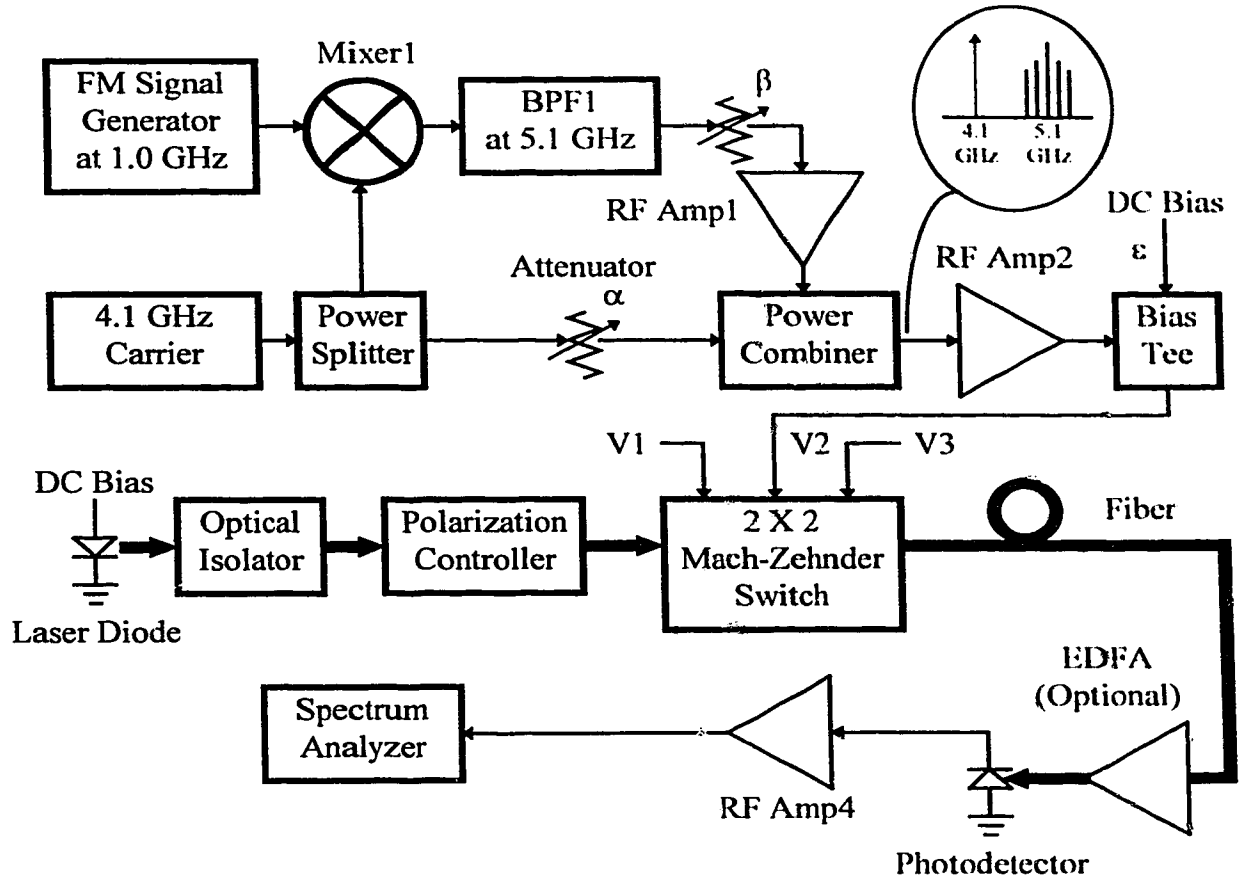


Figure 15: FM Experimental Setup Block Diagram

## 4.2 DQPSK Experimental Setup

The FM experiment serves as a proof-of-concept stage for the proposed modulation technique, but it fails to provide any BER measurement to fully demonstrate the system performance. It is therefore necessary to perform the  $\pi/4$  DQPSK experiments in order to analyze the noise performance of the system.

Figure 16 shows the experimental setup for the  $\pi/4$  DQPSK case. In comparison to the FM case, the FM signal generator is now replaced by the bit error ratio test (BERT) set and the  $\pi/4$  DQPSK modulator, and the RF amplifier and spectrum analyzer are substituted with the down converter and the  $\pi/4$  DQPSK demodulator. The BERT set generates a 50 Mbit/s pseudo-random bit stream which is used by the  $\pi/4$  DQPSK

modulator to modulate the carrier at 1.0 GHz ( $f_{IF1}$ ). This now becomes the modulated IF signal.

The down converter block diagram is shown Figure 17; it contains two band pass filters which filter out the fourth harmonic of the original 4.1 GHz carrier at 16.4 GHz ( $4f_{RF}$ ) as well as the  $\pi/4$  DQPSK modulated signal at 17.4 GHz ( $4f_{RF} + f_{IF1}$ ). The 16.4 GHz carrier is then used as the local oscillator signal to down-convert the modulated signal at 17.4 GHz down to 1.0 GHz using a microwave mixer. This signal is then fed to the input of the  $\pi/4$  DQPSK demodulator where it is demodulated down to base band, and the base band signal is routed back to the BERT set for BER measurements. It is important to point out that the unmodulated carrier at 16.4 GHz is intended to be used as a local oscillator signal in the up-link direction in a microcellular system; that is, it is used to convert the in-coming calls at microwave frequencies down to an intermediate frequency so that direct modulation of laser diodes is possible in the up-link direction. The use of this signal in the demodulation of the down-link signal in this experiment eliminates the need for a signal generator at 16.4 GHz and proves the usefulness of this up-converted carrier as a local oscillator signal in the eventual base station implementation. The  $\pi/4$  DQPSK modulator and demodulator will be presented later.

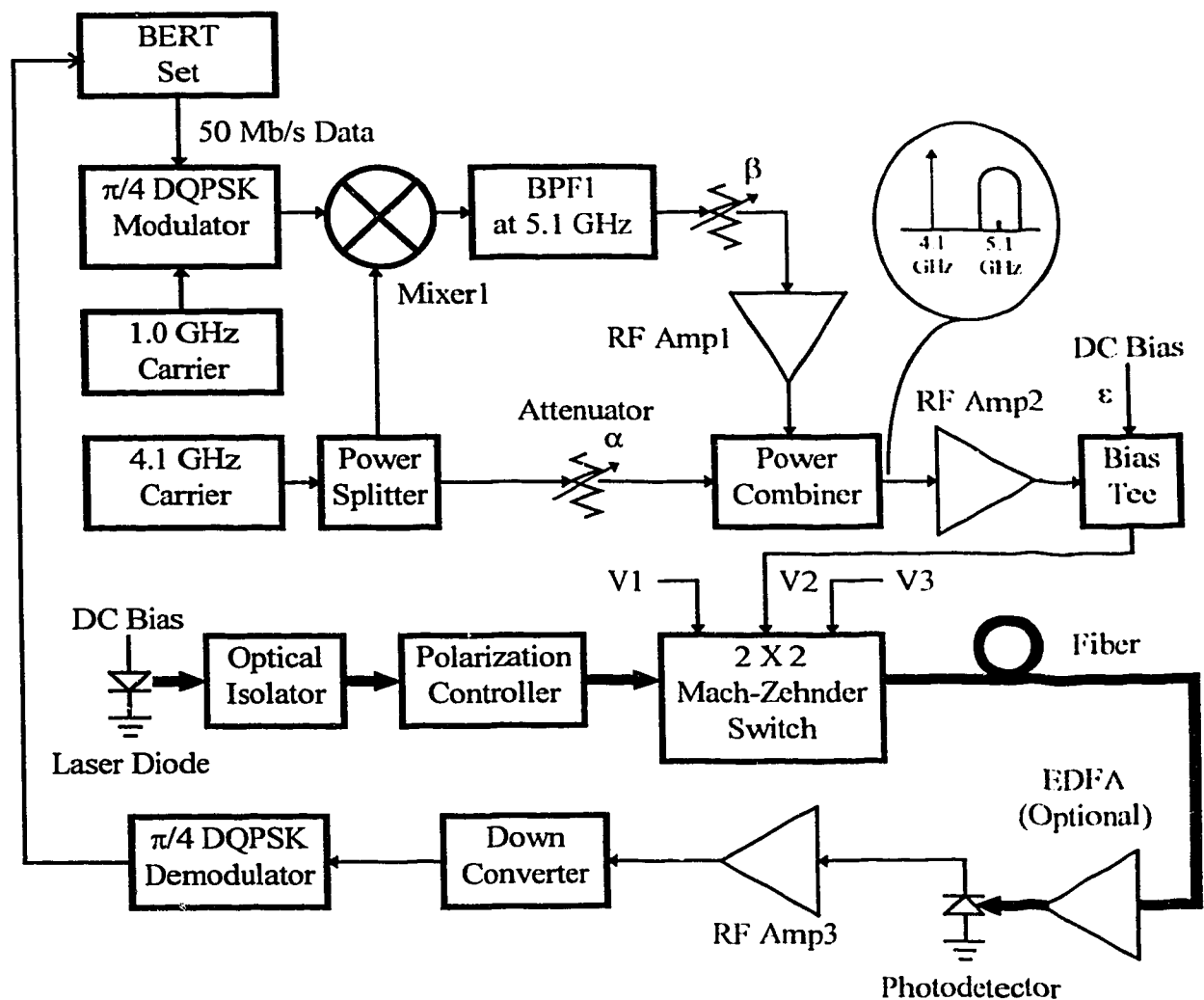


Figure 16:  $\pi/4$  DQPSK Experimental Setup Block Diagram

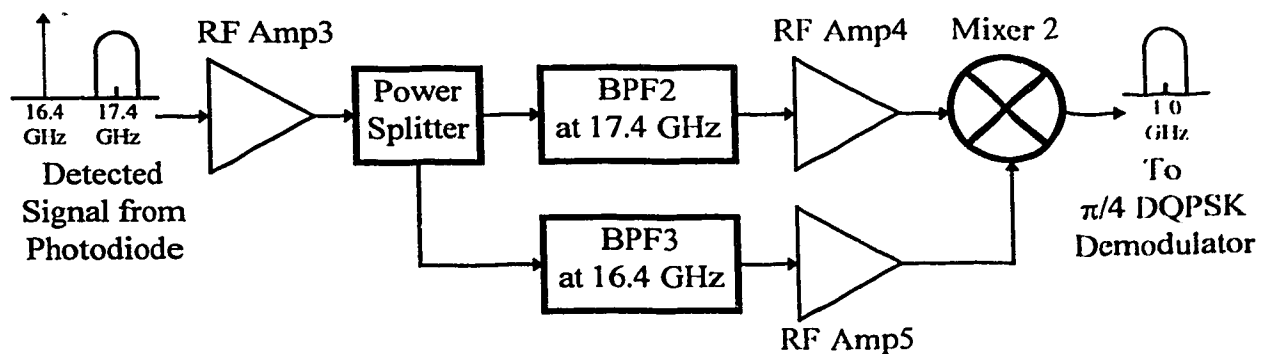


Figure 17: Down converter Block Diagram

## 4.3 RF Components

### 4.3.1 Amplifiers

A number of RF amplifiers are utilized in the experiments. The choice of amplifier for a specific application is generally based on the operating frequency, output power, gain and noise figure requirements. It is common practice to insert isolators or circulators at the output of high power amplifiers to limit the amount of reflected power since excessive reflected power can destroy the output stage of some amplifiers. A less expensive alternative would be to use attenuators in place of the isolators or circulators if the additional insertion loss can be tolerated. These attenuators are not shown in the block diagrams. The following table lists the specifications for the amplifiers used in the experiments.

Amplifier	Make	Model	Gain (dB)	Frequency Range (GHz)	Output Power 1 dB Comp. Point (dBm)	Noise Figure (dB)
IF Amp	Mini Circuit	ZHL-42W	30	0.01 - 4.2	+28	8
RF Amp1	CTT Inc.	APM/080-3036	36	2 - 8	+30	5.5
RF Amp2	SHF	SHF90P	25	10 kHz - 15	+ 10	7
RF Amp3	HP	AWT-18616	42	6 - 18	+20	2.8
RF Amp4	Miteq	JS4-00102600-30	30	0.1 - 26	+5	3
RF Amp5	HP	AWT-18057	42	8 - 18	+20	7

Table 3: Amplifier Specifications



### 4.3.2 Filters

Low pass and band pass filters are used in the experiments. The low pass filters are simple lumped element filters. All of the band pass filters are cavity filters featuring low insertion loss and high selectivity. The following table summarizes the specifications for the filters used in the experiments. Note that the two LPFs listed below are used in series in the demodulator to limit the amount of baseband noise in the experiment.

Filter	Make	Model	Center Frequency	3 dB Bandwidth	Insertion Loss
LPF	Mini Circuit	SLP-21.4	N/A	24 MHz	0.1 dB
LPF	Mini Circuit	SLP-30	N/A	36 MHz	0.1 dB
BPF1	K & L	7FV20-5100/T400-O/O	5.1 GHz	400 MHz	0.5 dB
BPF2	Trak Microwave	ACH17400-400-5SS	17.4 GHz	400 MHz	0.7 dB
BPF3	Trak Microwave	ACH16400-70-5SS	16.4 GHz	70 MHz	1.6 dB
IF BPF	Trak Microwave	ACC1000-100-6SS	1.0 GHz	100 MHz	0.3 dB

Table 4: Filter Specifications

### 4.3.3 Mixers

Two double-balanced mixers are chosen for the experiments. The double-balanced configuration provides excellent isolation between the input ports, which is essential for frequency conversion applications. The criteria for choosing a mixer are based on frequency range, LO power available (which relates to the maximum RF power), conversion loss, and isolation. The following table summarizes the performance of the two mixers used in the experiment. Note that the noise figure of a mixer is typically

equal to the specified conversion loss. During the experiments, the input power to the LO ports of the mixers must be maintained at the nominal LO power rating to achieve the specified performance. The input power level at the RF port (or at the IF port in the up-converter configuration) must also be at least 10 dB lower than the LO input power in order to remain in the linear operation region of the mixers.

Mixer	Make	IF Bandwidth	LO, RF Bandwidth	Conversion Loss	Nom. LO Power	Min. Isolation
Mixer 1	Narda 4804	DC - 1.7 GHz	4 - 8 GHz	7 dB	+10 dBm	17 dB
Mixer 2	Merrimac DML-2B-10G	DC - 3 GHz	2 - 18	6.5 dB	+7 to +10	18 dB

Table 5: Mixer Specifications

#### 4.3.4 $\pi/4$ DQPSK Modulator

Figure 18 depicts the block diagram for the hardware implementation of the  $\pi/4$  DQPSK Modulator. The schematic level design description for the different blocks of the modulator shown in Figure 18 can be found in Appendix C. Since  $\pi/4$  DQPSK is a quaternary modulation format, the 50 Mb/s input data stream from the BER test set is first divided into two parallel streams at the symbol rate 25 Mb/s by the demultiplexer (DEMUX). As shown in Figure 11, eight phase states are required to cover all the possible phase transitions for a  $\pi/4$  DQPSK signal. To obtain these phase states, the two parallel data streams are differentially encoded by the Differential Encoder (modeling Eq. 3-2) to produce one of eight possible digital states represented by 3 digital lines. These digital signals must be converted to analog voltages to drive the I and Q inputs of the I/Q Modulator. This is accomplished by using two 10-Bit Digital to Analog Converters (DACs). The phase state decoder performs the function of interfacing the three digital signals with the DACs by decoding the 3 digital signals and mapping the phase states to their corresponding 10-bit words. Each 10-bit word represent a current level to be

generated by the DACs. These DACs convert the 10-bit digital code words into analog current signals, which are then transformed into voltage signals by the current to voltage (I to V) buffers. The components described so far constitute the Phase Selector block in the Simplified Modulator Block Diagram found in Figure 12. The QPSK Modulator in Figure 18 contains the rest of the RF components (i.e. mixers, power splitters, and phase shifter) found in Figure 12.

The QPSK Modulator used is a Miteq SM0102LC1 I/Q Modulator. Its RF input power at 1.0 GHz must be maintained at +10 dBm to fully turn on the mixers, while the modulating signal at the I and Q inputs should be set to  $\pm 30$  mA peak (or +13 dBm RMS power for sinusoidal modulation) to achieve maximum spacing between phase states in the constellation. Conversion loss from the RF input to the RF output is approximately 10 dB. The output  $\pi/4$  DQPSK signal at 1.0 GHz is passed through the 1.0 GHz band pass filter to eliminate undesired harmonics and image terms produced by the mixing processes.

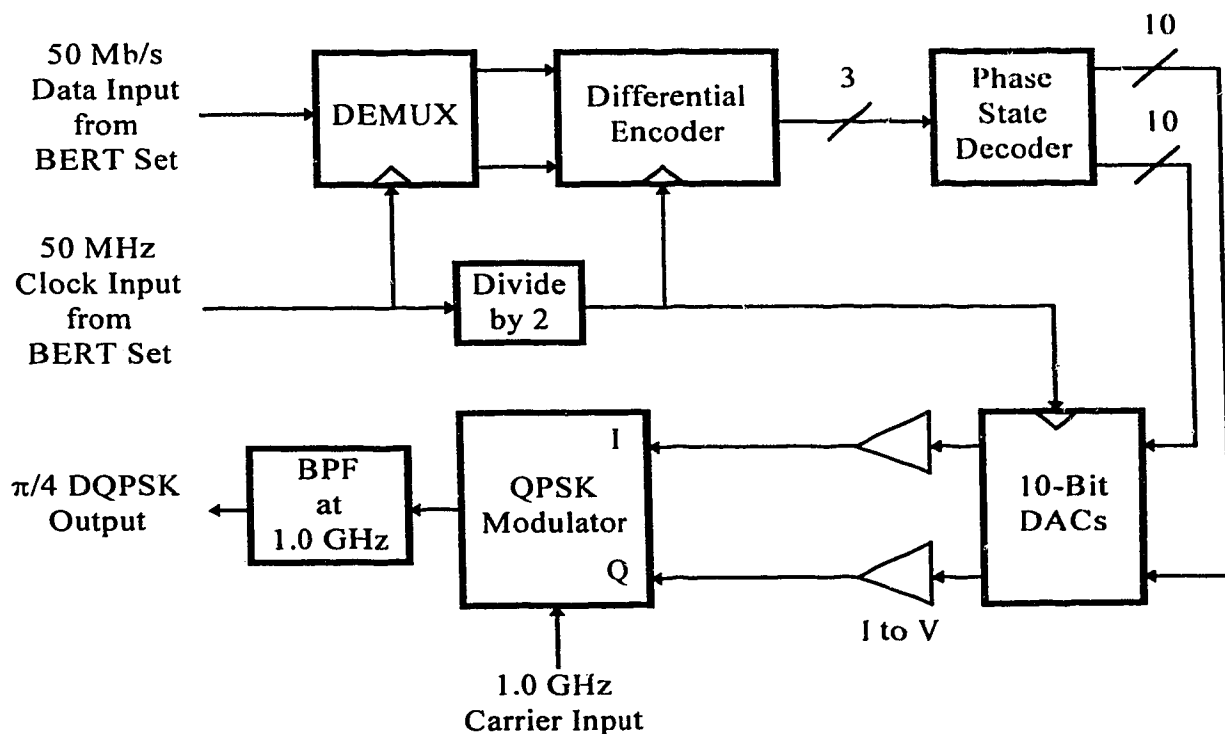


Figure 18:  $\pi/4$  DQPSK Modulator Block Diagram

#### 4.3.5 $\pi/4$ DQPSK Demodulator

Figure 19 depicts the  $\pi/4$  DQPSK demodulator block diagram. A schematic level design description can be found in Appendix D. The  $\pi/4$  DQPSK signal down-converted to 1.0 GHz is first fed to the IF filter at 1.0 GHz to purge all unwanted harmonics and then amplified by the IF amplifier. It is then split into two branches through a power splitter. To facilitate differential demodulation, one branch passes through a 40 ns delay line and then to the LO input of the I & Q Phase Detector while the other branch is fed directly to the RF port of the Phase Detector. A Miteq IQD01C07E I/Q Phase Detector with built in IF amplifiers (gain = 17 dB) at the I and Q outputs is used; it contains the mixers, power splitter and phase shifter shown in Figure 13. Similar to the other mixers employed in the experiment, the Phase Detector LO input must be kept at +10 dBm while the RF port input should be at least 10 dB less than the power level at the LO port. Outputs of the Phase Detector are filtered by cascading two low pass filters with the combined 3 dB cutoff frequency of 24 MHz; the filtered signals represent the decision variables described by Eq. 3-11 and 3-14. Two high speed comparators are used to compare the decision variables with zero volts and to generate 2 TTL signals corresponding to the transmitted symbol. These TTL signals are latched by the 25 MHz clock and then converted into a serial data stream by the multiplexer (MUX). Adjustment for the decision time of the demodulator to give optimum BER is provided by the Delay Adjust. Output from the Delay Adjust is fed back to the BERT set for BER measurements.

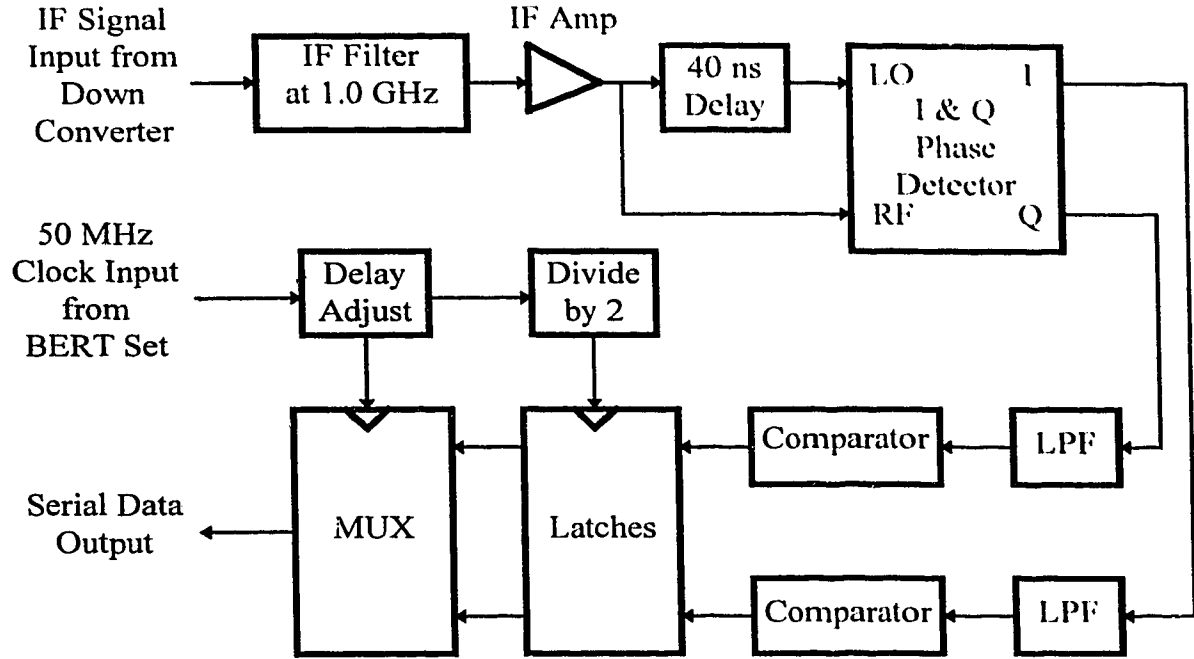


Figure 19:  $\pi/4$  DQPSK Demodulator Block Diagram

## 4.4 Optical Components

### 4.4.1 Laser Source

A Fujitsu distributed feedback (DFB) laser model #FLD150F3CJ is used as the optical source for all experiments. Its maximum output power is +6 dBm and its operating wavelength is 1551.0 nm. This laser is chosen because of its high output power and its DFB structure which yields a narrow spectral linewidth.

Because of the quantum nature of light, all lasers are inherently noisy. Spontaneous emission is the main contributor to phase and intensity noise in lasers [32]. Phase noise, or fluctuation in the emission frequency, is the cause of a laser's finite spectral linewidth; intensity fluctuation of the spontaneous emission causes the laser intensity noise. This laser intensity noise is commonly defined by the relative intensity noise (RIN) factor, which is the ratio of the laser intensity noise to the average output power of the laser. The RIN of the laser source used in this project was measured by a former graduate

student at TRILabs [44] to be approximately -139 dB/Hz at 16-18 GHz. It will be shown later that this RIN specification is adequate for the experiments as the noise contribution from the laser is never the dominant noise term.

#### **4.4.2 Optical Isolators**

Optical isolators are used to minimize backward traveling optical signals due to reflections along the system; this is especially important for the laser source as the spectral linewidth of the laser can be significantly degraded (broadened) by back reflections. For this reason, an optical isolator is inserted immediately after the laser source. In addition, it is also necessary to place optical isolators before and after an EDFA to eliminate Double Rayleigh Back-scattering (DRB) noise [33]. The optical isolators used typically provide at least 30 dB of optical isolation with an insertion loss of less than 2 dB.

#### **4.4.3 Mach-Zehnder Switch**

An ETEK EOSW-0202-1550 2X2 Electro-optic Switch is used as an optical external modulator in the experiments. Its physical structure is a balanced bridge interferometer 2X2 switch shown in Figure 20. This configuration is slightly different than the one depicted in Figure 5. The input and output couplers are constructed by placing two waveguides in close proximity. Depending on the tuning voltage settings at the input and output couplers, a certain amount of optical power from one waveguide will be coupled into the other. When the tuning voltages are adjusted so that the couplers split the optical power equally, the ETEK 2 X 2 Switch functions similarly to the Mach-Zehnder external modulator shown in Figure 5. This switch typically requires a DC switching voltage ( $V_{\pi}$ ) of approximately 4 to 5 Volts, and its specified electrical bandwidth at the electrical input  $V_2$  is 7 to 8 GHz with a maximum input power rating of +30 dBm. Its optical insertion loss is 6 to 8 dB.

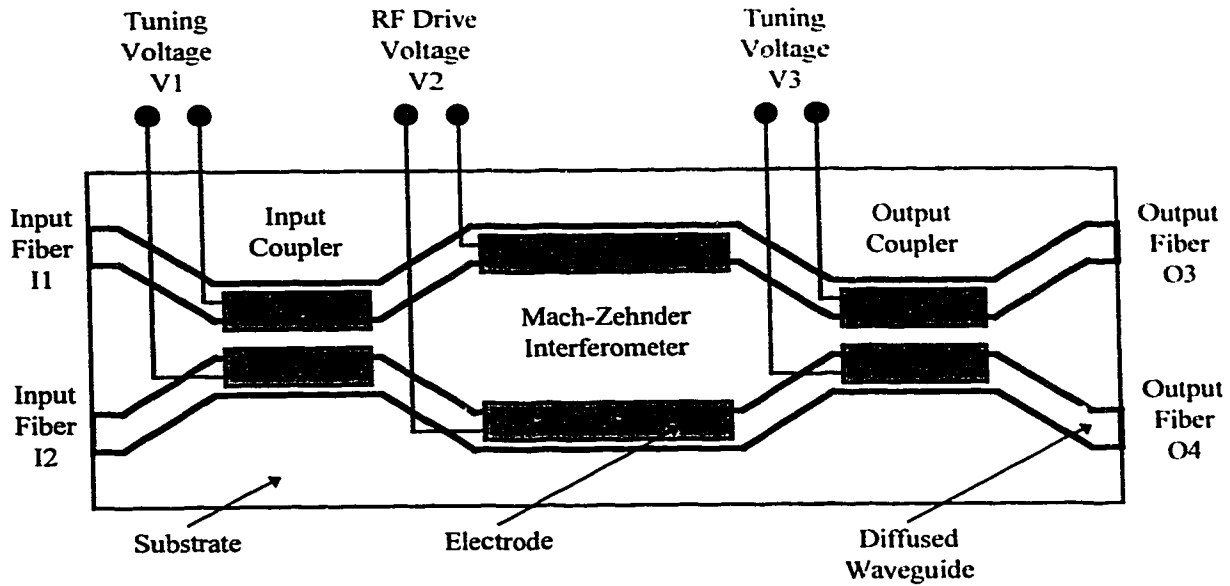


Figure 20: ETEK 2 X 2 Switch Configuration

#### 4.4.4 Polarization Controller

The Electro-optic effect in the Lithium Niobate external modulator is highly sensitive to the polarization of the input light. This electro-optic effect is approximately three times greater for a TE mode than for a TM mode. Therefore, in order to maximize the electro-optic effect of the modulator, it is essential that the polarization of the input light should be as linear as possible, and that the axis of polarization is oriented so that the TE mode is aligned properly to the applied electric field. The polarization controller used in the experiments to perform this function was built at TR Labs according to the directions given in reference [34]. Its insertion loss is typically 1 dB.

#### 4.4.5 Optical Amplifier

An Erbium Doped Fiber Amplifier (EDFA) is used in the experiment to boost the optical power for longer distance transmission. It can be treated as a conventional amplifier in the optical domain with a unique noise contribution. A typical EDFA is composed of a pump laser source, a length of Erbium-doped fiber, two wavelength division multiplexers (WDM), and an optical band pass filter as shown in Figure 21. Operation of EDFAs has

been widely studied due to their application in long haul transmission systems as in-line amplifiers. In addition, thermal noise generated by the receiver electronics is usually the limiting noise component in many optical transmission systems. In this case, an EDFA can also be used prior to the photodiode as a pre-amplifier to amplify the received optical signal and thus increase the signal to noise ratio. This can be performed until the optical noise generated by the EDFA surpasses the thermal noise of the receiver.

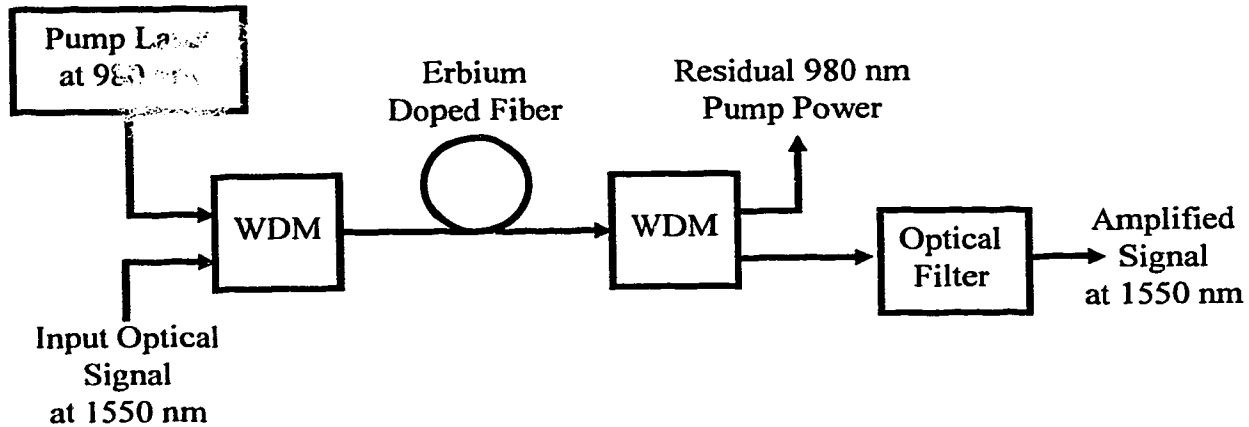


Figure 21: Erbium Doped Fiber Amplifier Block Diagram

The operating principles of EDFAs are relatively straight forward and will be presented here; a more detailed and mathematically involved explanation can be found in reference [35]. At the input of the EDFA, the optical signal at 1550 nm and the high-power pump laser output at 980 nm are multiplexed onto the same Erbium doped fiber through the WDM. The 980 nm pump light is readily absorbed by the Erbium ions ( $\text{Er}^{3+}$ ) in the Erbium doped fiber; this causes the Erbium ions to be excited to a higher energy level. As the 1550 nm signal passes through the Erbium fiber, stimulated emission occurs - the Erbium ions collapse back down to their original energy level and release the absorbed energy from the 980 nm pump into the 1550 nm signal. The amplified 1550 nm signal is separated from the 980 nm pump light through the output WDM and is then fed to the optical band pass filter. Reasons for this optical filter will be explained later. The portion of the 980 nm pump light that is not absorbed by the Erbium fiber is known as residual pump power and is available at the other output port of the WDM.



Since the spontaneous emission mechanism in the Erbium doped fiber is a statistical process, it is possible for the Erbium ions to change energy state spontaneously without being stimulated by the 1550 nm signal. The spontaneously emitted light, commonly called spontaneous emission, is also amplified as the spontaneously emitted photons travel down the Erbium doped fiber and stimulate additional photon emission resulting in amplified spontaneous emission (ASE), which is the main source of noise contribution for an EDFA. An optical band pass filter can be used to band-limit the amount of ASE power in the system since the ASE spectrum is typically tens of nanometers wide. In the experiments, a JDS FIBEL TB1500B tunable band pass filter is used. It has a tuning range of 1530-1560 nm, insertion loss of 2.5 dB, and 3 dB optical bandwidth of 1.4 nm at 1550 nm.

It is normally assumed that the ASE spectrum is flat across moderate optical bandwidths. Based on this assumption, the average ASE power from an EDFA can then be expressed as [36]

$$P_{sp} = 2h\nu B_o N_{sp} (G - 1) \quad \text{Eq. 4-1}$$

where  $\nu$  is the optical frequency of the 1551 nm input signal,  $h$  is Planck's constant of  $6.6262 \times 10^{-34}$  J-s,  $B_o$  is the ASE bandwidth specified by the optical filter,  $N_{sp}$  is the spontaneous emission factor of the EDFA, and  $G$  is the amplifier gain. The EDFA used in the experiment is TRILabs Serial # TRL9407-BF450-002. Its  $N_{sp}$  is 1.26, and its small signal gain for input optical power less than -20 dBm is approximately 14 dB. The optical bandwidth  $B_o$  is actually the noise bandwidth of the optical filter, and for calculation purposes,  $B_o$  is approximately 1.9 nm for the filter with 3 dB bandwidth of 1.4 nm.

When the ASE power and the amplified signal power are detected by a square law detector, the broad band ASE beats with both itself and the amplified signal resulting in base band noise. The base band noise current spectral density generated by ASE beating with itself is called spontaneous-spontaneous beat noise and is defined by [37]

$$i_{sp-sp}^2 = 4B_o \left[ N_{sp} \eta L (G - 1) q \right]^2 \quad \text{Eq. 4-2}$$

where  $\eta$  is the detector quantum efficiency given by  $\eta = \Re h\nu / q$ ,  $q$  is the electron charge, and  $L$  is the power loss factor introduced to account for the optical power loss from the output of the EDFA to the photodiode. Note that this equation assumes that the ASE spectrum is uniform within the bandwidth  $B_o$ . The multiplying process of ASE beating with itself in the electric field domain translates to the convolution of the rectangular ASE spectrum with itself in the frequency domain resulting in a triangular spontaneous-spontaneous beat noise spectrum with single-sided bandwidth of  $B_o$ . The noise current spectral density in Eq. 4-2 provides an approximate measure of the spontaneous-spontaneous beat noise power and assumes that the variation in ASE beat noise power due to its triangular spectral shape can be ignored. This assumption is based on the fact that an optical bandwidth in the range of nanometers corresponds to an electrical bandwidth in the order of hundreds of GHz, i.e., by using the relationship

$$\begin{aligned} f &= \frac{c}{\lambda} \\ \Delta f &= -\frac{c}{\lambda^2} \Delta \lambda \end{aligned} \quad \text{Eq. 4-3}$$

the optical bandwidth ( $\Delta \lambda$ ) of 1.4 nm is equal to an electrical bandwidth ( $\Delta f$ ) of 175 GHz at the operating wavelength ( $\lambda$ ) of 1551 nm. Therefore, only the first ten percent of the noise power near DC are significant in a system operating up to 18 GHz. In addition, we are only concerned with narrow band signals at 16.4 and 17.4 GHz in the experiment, hence the rectangular spontaneous-spontaneous beat noise spectrum can be treated as essentially flat in the experimental setup.

The noise contribution due to ASE beating with the signal at the square-law detector is known as signal-spontaneous beat noise and its noise current density is given by [37]

$$i_{sig-sp}^2 = \frac{4q^2}{h\nu} \eta^2 L^2 P_{EDFA} N_{sp} (G - 1) G \quad \text{Eq. 4-4}$$

where  $P_{EDFA}$  is the average input signal power to the EDFA. This expression is again based on the assumption that the ASE spectrum is rectangular and the signal spectrum can be approximated by the impulse function with non-zero value at the operating wavelength of the laser source (1551 nm). Under these conditions the base band signal-spontaneous beat noise spectrum is uniform within  $B_o$  with its amplitude specified by Eq. 4-4.

#### 4.4.6 Optical Fiber

Standard single mode fiber is used in all experiments. Its attenuation constant at an operating wavelength of 1551 nm is approximately 0.22 dB/km, and its dispersion factor is 17 ps/(km·nm). The dispersion factor is a measure of how much an optical pulse will be broadened as it travels through a length of fiber due to the frequency dependence of propagation delay in fiber. A maximum length of 50 km of optical fiber was used in the experiments.

#### 4.4.7 Photodetector

The optical detector used in the experiment is a BT&D model #PDC4310 PIN Photodetector. Its specified frequency response is DC to 20 GHz and the responsivity (optical to electrical conversion efficiency) is approximately 0.5 A/W at 16 to 18 GHz. Although former graduate students at TRLabs have reported that the 3 dB electrical bandwidth of the detector is actually less than 10 GHz, its narrow band frequency response from 16 to 18 GHz is still adequate for the experiments.

### 4.5 Noise Analysis

The mean squared noise current spectral density from the RF electronic components constitutes the system's thermal noise as given by

$$i_{th}^2 = \frac{4kTF}{R} \quad \text{Eq. 4-5}$$

where  $k = 1.38 \cdot 10^{-23}$  is the Boltzmann constant,  $T = 300$  is the resistor temperature,  $R = 50\Omega$  is the characteristic impedance of the electrical system, and  $F$  is the composite noise figure of the receiver. This composite noise figure can be determined by the following relationship [38].

$$F = F_{RF\text{Amp}2} + \frac{F_{RF\text{Amp}3} - 1}{G_{RF\text{Amp}2}} + \frac{F_{IF\text{Amp}} - 1}{G_{RF\text{Amp}2} G_{RF\text{Amp}3}} \quad \text{Eq. 4-6}$$

Using the noise figures and gain specifications tabulated in Table 3,  $F$  is equal to 2.8 dB, which is simply the noise figure of the first amplifier in the receiver (i.e. RF Amp 2).

The noise current spectral density due to the relative intensity noise of the optical source is given by

$$i_{RIN}^2 = RIN(P_d \mathfrak{R})^2 \quad \text{Eq. 4-7}$$

where  $RIN$  and  $\mathfrak{R}$  are respectively the relative intensity noise factor for the optical source and responsivity of the detector as defined before, and  $P_d$  is the average optical signal power incident on the detector.

The noise current spectral density caused by shot noise from the optical signal and ASE is

$$i_{shot}^2 = 2q\mathfrak{R}(P_d + P_{sp}) \quad \text{Eq. 4-8}$$

where  $P_{sp}$  is the ASE optical power defined in Eq. 4-1.

In addition, the EDFA also generates spontaneous-spontaneous beat noise  $i_{sp-sp}^2$  and signal-spontaneous beat noise  $i_{sig-sp}^2$  given by Eq. 4-2 and Eq. 4-4 respectively.

Finally, the detected signal current is given by

$$i_{sig}^2 = (\mathfrak{R}P_{sig})^2 \quad \text{Eq. 4-9}$$

where  $P_{sig}$  is the root mean squared optical power associated with the modulated signal at 17.4 GHz. This power level is related to the total optical signal power  $P_d$  by a constant specified by the input RF drive coefficients  $\alpha$  and  $\beta$  as defined before. Using Eq. 2-16,  $P_{sig}$  can be related to  $P_d$  by

$$P_{sig} = [J_1(\pi\alpha)J_3(\pi\beta)]P_d. \quad \text{Eq. 4-10}$$

This expression assumes that the Mach-Zehnder modulator output characteristics can be ideally described by Eq. 2-11. We can also use the measured carrier power at 17.4 GHz to calculate the carrier to noise ratio (CNR) for the system if the Mach-Zehnder modulator deviates significantly from the theoretical performance.

With the above five noise terms and signal current defined, and assuming an electrical noise bandwidth of  $B_N$ , the CNR of the modulated signal at 17.4 GHz can be given as

$$CNR = \frac{i_{sig}^2}{[i_{RIN}^2 + i_{shot}^2 + i_{sp-sp}^2 + i_{sig-sp}^2 + i_{th}^2] \cdot B_N}. \quad \text{Eq. 4-11}$$

## 5. Experimental Results and Discussions

### 5.1 FM Experiments

Prior to the construction of the  $\pi/4$  DQPSK modulator/demodulator, a frequency modulated (FM) signal was used to validate the operation of the proposed frequency up-conversion scheme. FM was chosen because tone modulated FM signals can be easily generated using an HP8642A signal generator available at TRLabs; the FM spectra can also be verified using a spectrum analyzer and compared with simulated spectra. Note that the experimental results presented in this section and part of the background theory were published in references [39] and [40].

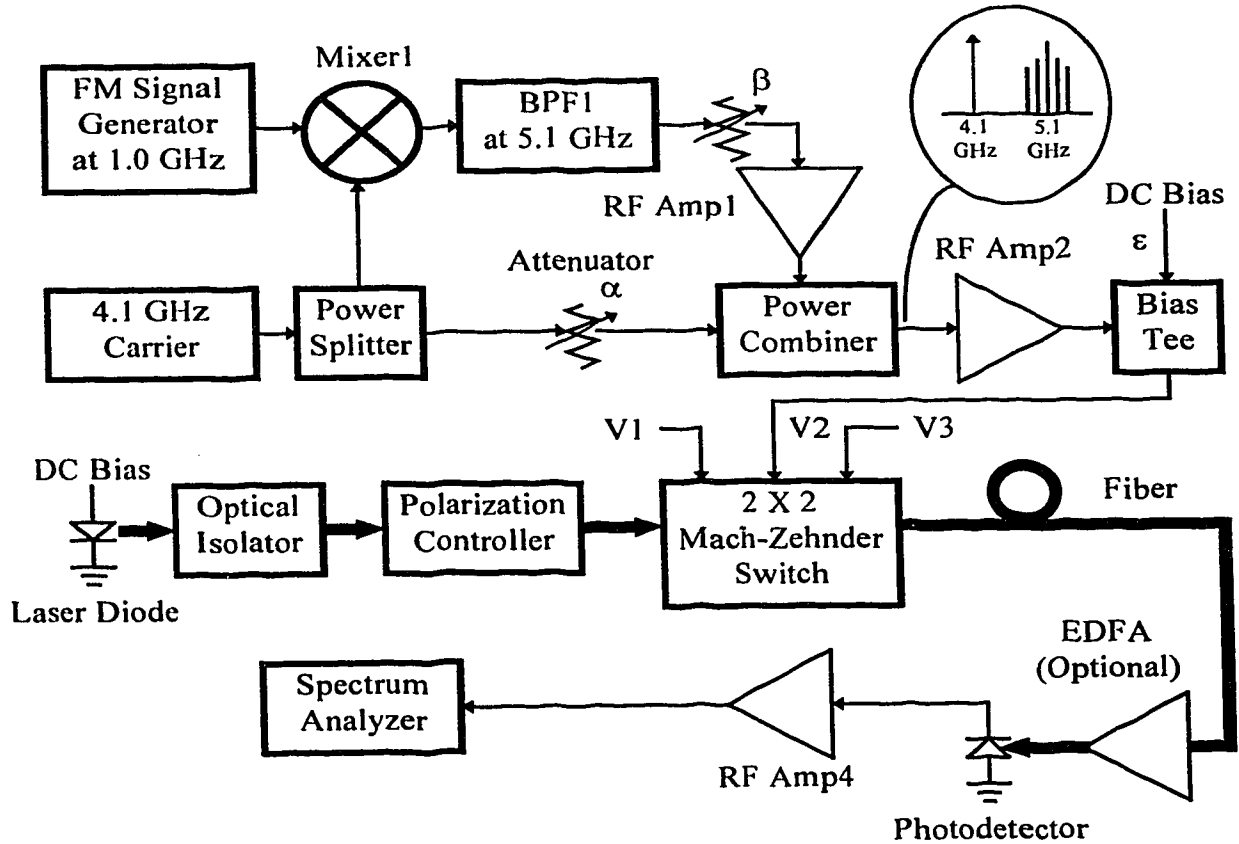


Figure 15: FM Experimental Setup Block Diagram

Figure 15 is redrawn to illustrate the setup used for the FM experiments. The FM signal is generated by modulating a 0.95 GHz ( $f_{IF}$ ) carrier by a 50 kHz sinusoidal signal, with a frequency modulation index of 1, giving a frequency deviation of 50 kHz. With  $f_{RF}$  chosen to be 4.1 GHz, the up-converted FM signal at  $4f_{RF} + f_{IF}$  will be at 17.35 GHz, instead of 17.4 GHz when a 1.0 GHz IF source is used.

Without using the optical/electrical amplifiers and optical fiber, the detected electrical spectra at the output of the Mach-Zehnder modulator in the frequency range near  $4f_{RF}$  are shown in Figure 22, Figure 24, and Figure 25. Figure 22 is the detected unmodulated carrier at 16.40 GHz. It is important to observe that its line width is extremely narrow ( $\sim 10$  Hz) and is, within the measurement capability, equal to that of the 4.1 GHz signal generator shown in Figure 23. This indicates that the phase noise of the laser, whose line width is  $> 150$  MHz, does not contribute to the broadening of the up-converted electrical carrier. This can be explained if we view this technique as an optical homodyne system where the optical local oscillator signal is generated, using the Mach-Zehnder non-linearity, by the same source as the optical information carrier [22]. Hence the phase noise of the two optical signals are highly correlated which results in extremely narrow line width in a coherent optical system. Note that the extra sidebands in Figure 23 are due to the residual phase noise of the signal generator having relatively insignificant power levels.

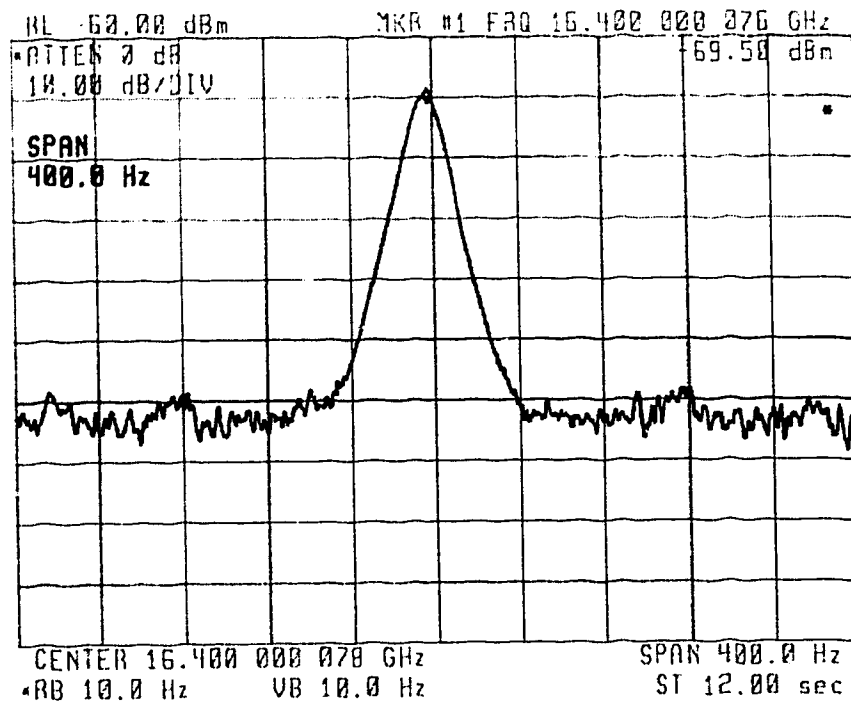


Figure 22: Unmodulated Carrier at 16.4 GHz (no fiber, no EDFA)

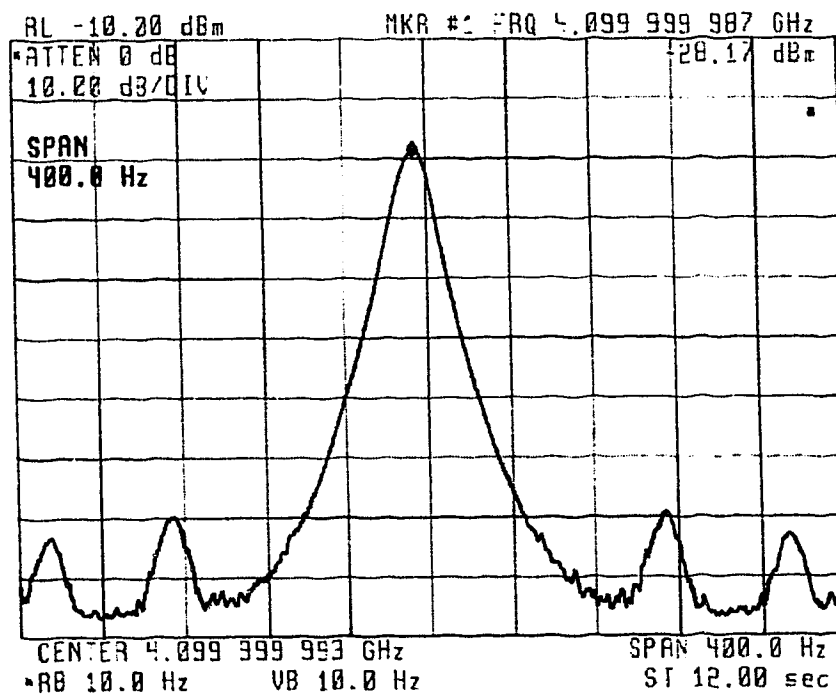


Figure 23: Spectrum of the RF Drive at 4.1 GHz (Signal Generator Output)



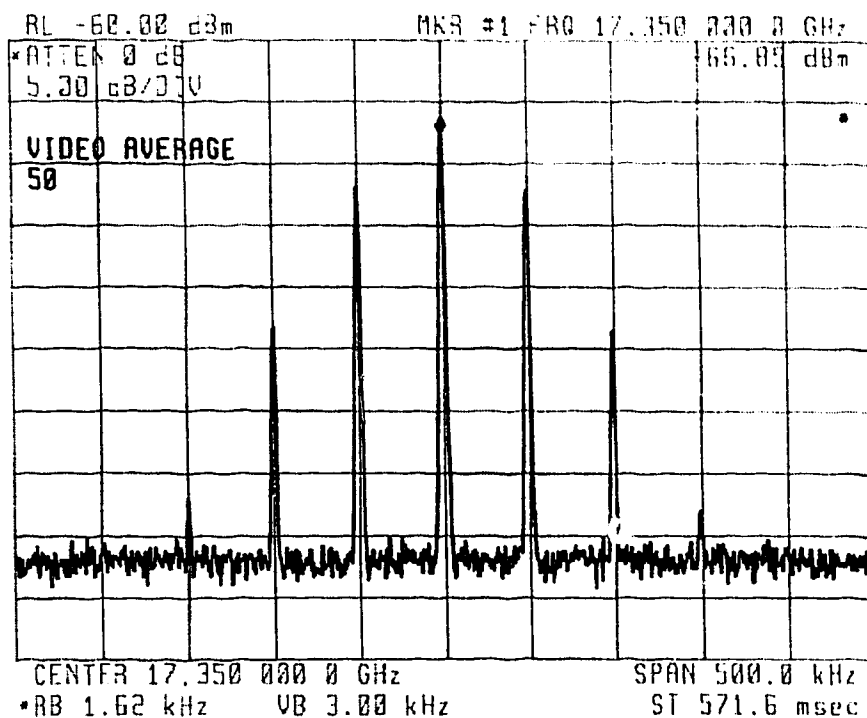


Figure 24: FM Signal at 17.35 GHz (no fiber, no EDFA)

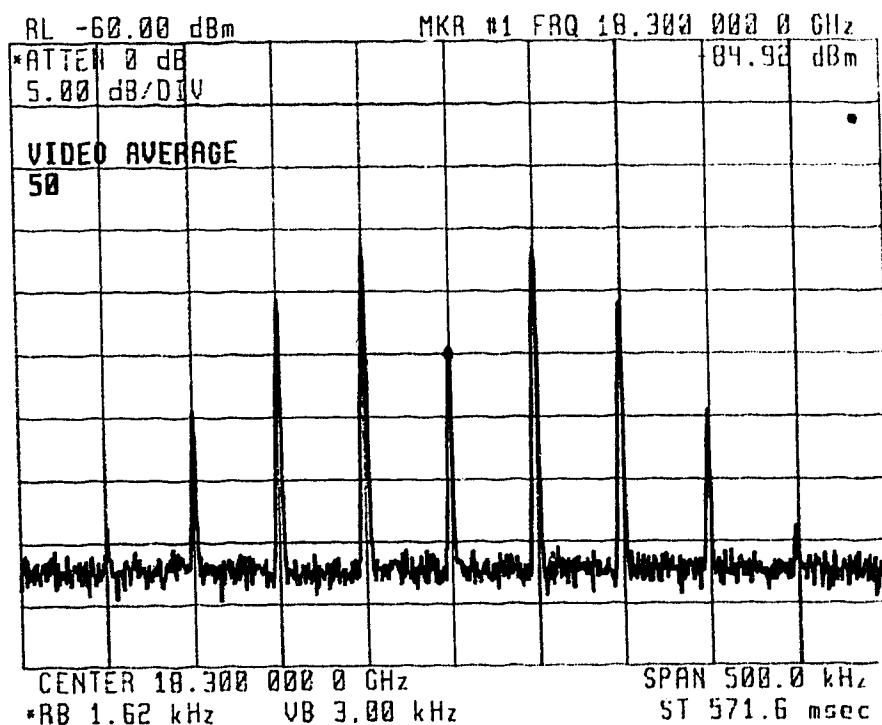


Figure 25: FM Signal at 18.3 GHz (no fiber, no EDFA)

The spectra for the up-converted information signals at 17.35 GHz and 18.30 GHz are depicted in Figure 24 and Figure 25 respectively. These frequencies correspond to the terms at  $4f_{RF} + f_{IF}$  and  $4f_{RF} + 2f_{IF}$  in the up-conversion scheme with  $f_{RF} = 4.1$  GHz and  $f_{IF} = 0.95$  GHz. For comparison, the corresponding theoretical FM spectra are shown in Figure 26 and Figure 27. In these figures, the frequency axes are normalized to the FM modulating frequency of 50 kHz, and are centered around the corresponding carrier frequency. A 50 kHz modulating signal and a frequency modulation index of 1 was used to generate Figure 26; the same 50 kHz modulating signal was employed in Figure 27 but the modulation index was increased from 1 to 2. This increase in modulation index can be explained by Eq. 2-16 where it is apparent that for an up-converted signal at frequency  $mf_{RF} + nf_{IF}$ , its phase (or frequency) modulation signal is multiplied by the integer  $n$ . For the signal at 18.30 GHz,  $n=2$ , hence its modulation index is twice that of the signal at 17.35 GHz. By comparing the simulated and measured spectra it is apparent that the relative amplitudes of the FM side bands are at the correct levels, hence the FM spectra are preserved using this technique, and the up-conversion technique behaves as expected according to Eq. 2-16.

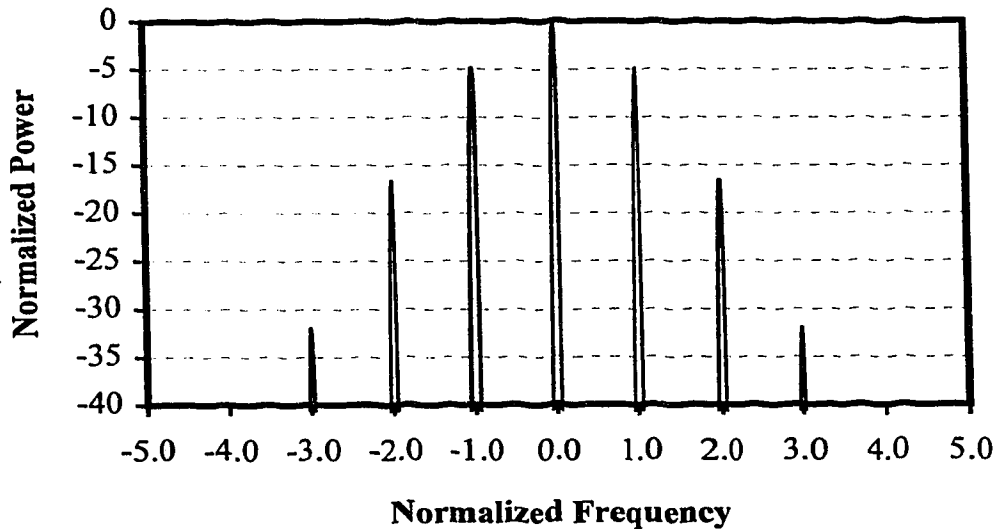


Figure 26: Simulated FM Spectrum Normalized to 50 kHz Centered at 17.35 GHz

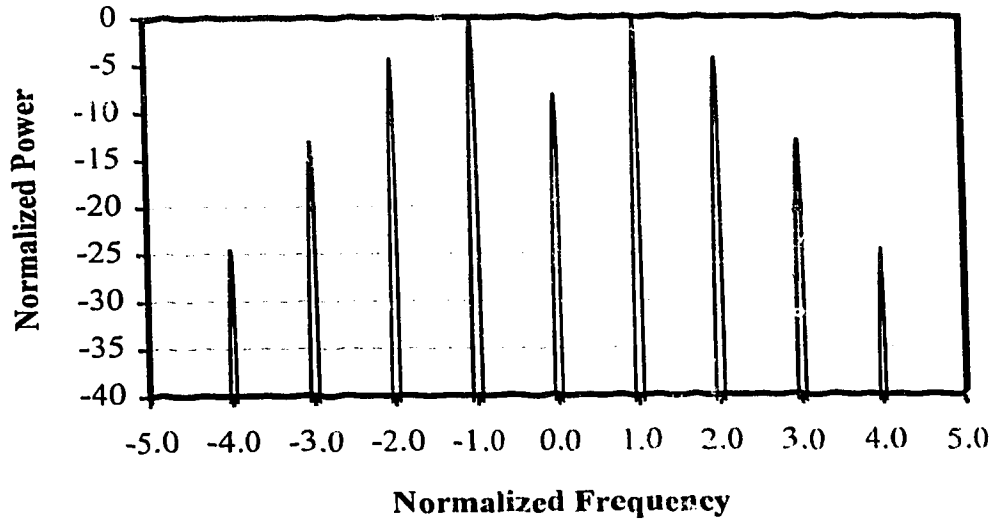


Figure 27: Simulated FM Spectrum Normalized to 50 kHz Centered at 18.3 GHz.

To explore the transmission characteristics over fiber using this technique, 20 km of optical fiber, an EDFA, and an electrical amplifier were inserted into the system. The resulting up-converted spectra are depicted in Figure 28 and Figure 29. Even with the use of 20 km of dispersive fiber and an EDFA, there is no observable degradation in the line width of the unmodulated carrier at 16.4 GHz and in the spectral shape of the detected FM signals at 17.35 GHz and 18.30 GHz as compared with Figure 22 to Figure 25. It can therefore be concluded that the proposed technique can indeed be used to up-convert an unmodulated carrier as well as a frequency modulated signal using only one external optical modulator. The performance of this technique will be verified in greater detail in a later section using  $\pi/4$  DQPSK signals.

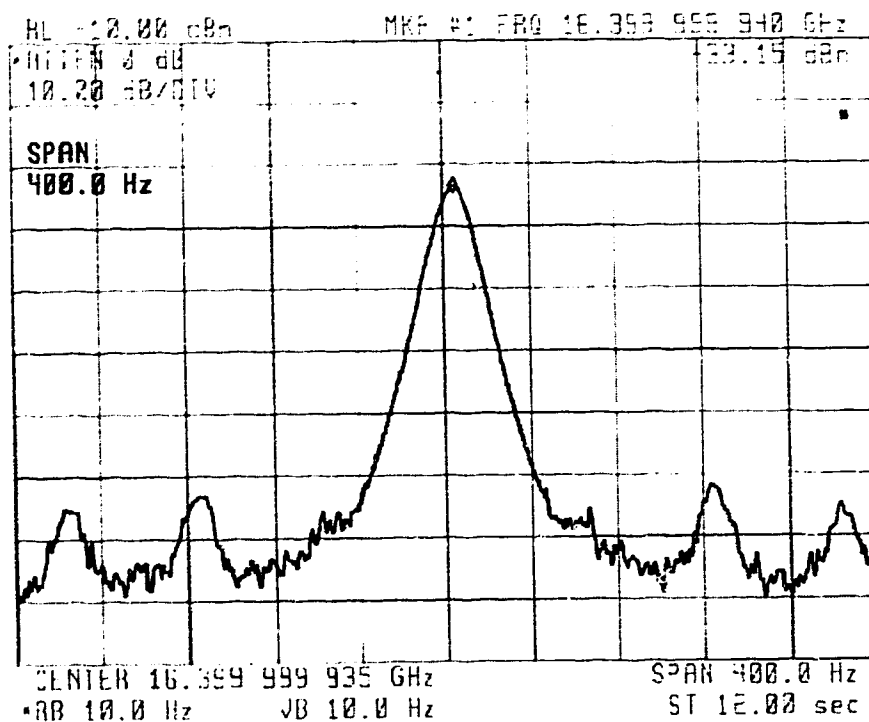


Figure 28: Unmodulated Carrier at 16.4 GHz (using 20 km of fiber and an EDFA)

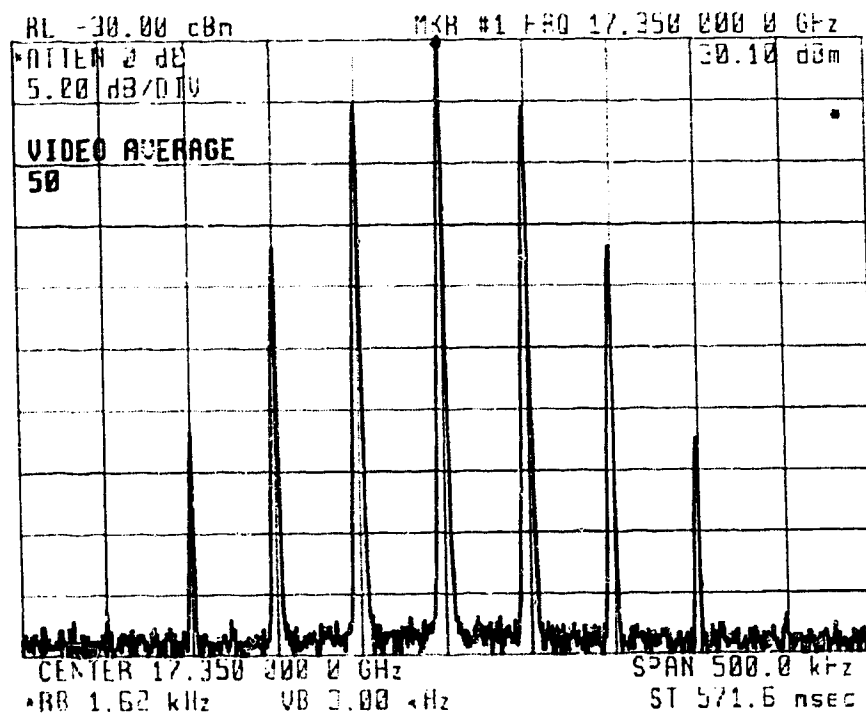


Figure 29: FM Signal at 17.35 GHz (using 20 km of fiber and an EDFA)

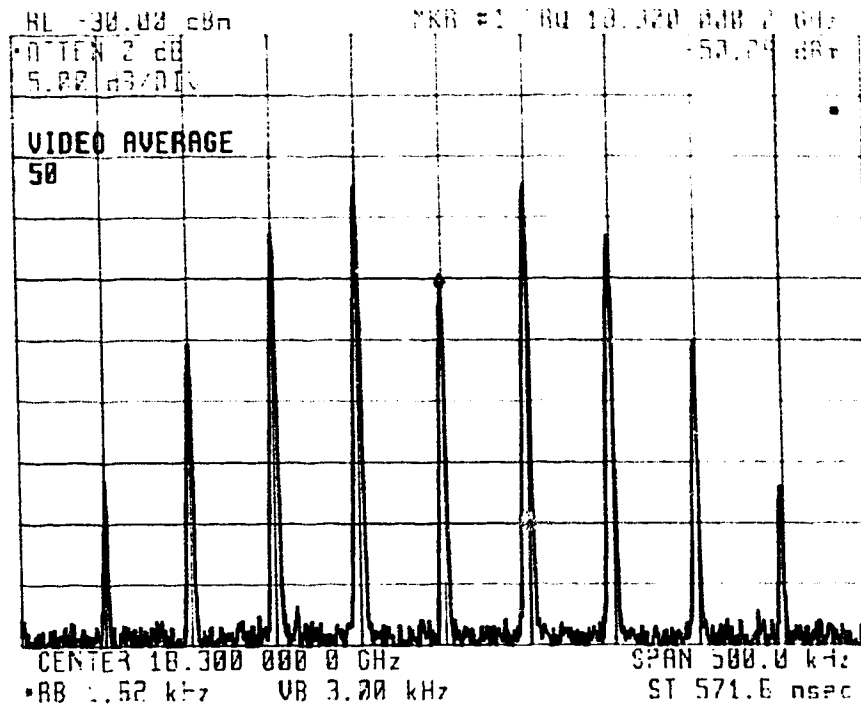


Figure 30: FM Signal at 18.3 GHz (using 20 km of fiber and an EDFA)

## 5.2 Characterization of $\pi/4$ DQPSK Modulator/Demodulator

In order to perform BER versus SNR measurements, the  $\pi/4$  DQPSK modulator/demodulator (MODEM) must first be tested back-to-back to obtain a set of reference data which can be used to compare with the experimental results. One of the most common ways for testing a communication system's noise performance is to maintain the signal power at a constant level while varying the noise power to produce a BER versus SNR curve. For the demodulator, the requirement of constant signal power is especially important because of the necessity to maintain a constant +10 dBm input power to the LO port of the I/Q Phase Detector as discussed in section 4.3.5. This requires a spectrally flat noise source with a usable bandwidth of at least 100 MHz centered around the IF frequency of 1.0 GHz. A good candidate for this noise source is the ASE power generated by an EDFA as described in section 4.4.5. Figure 31 depicts the hardware setup used for testing the  $\pi/4$  DQPSK MODEM.

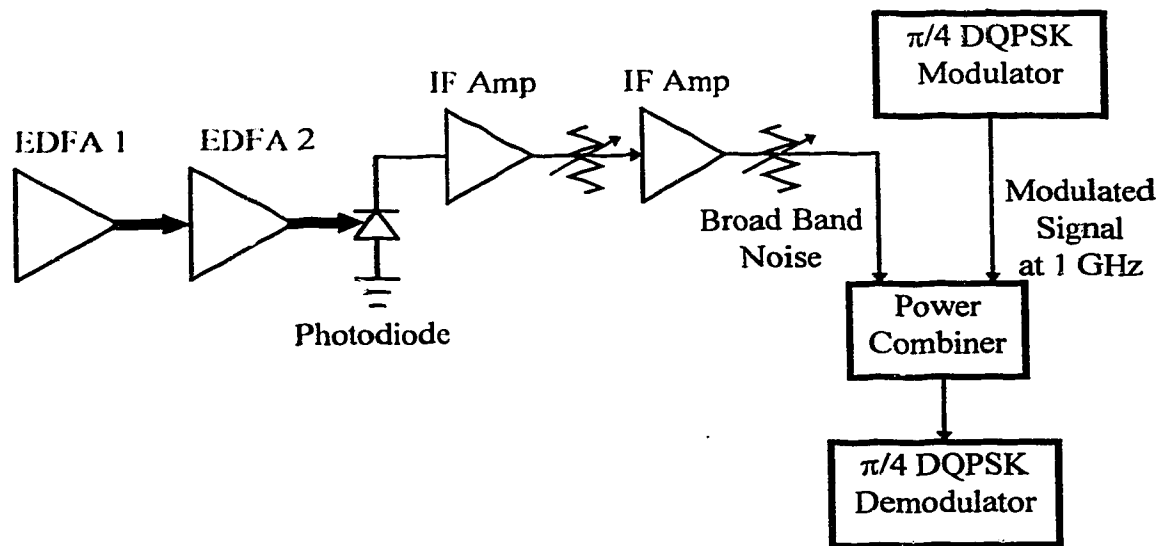


Figure 31: Characterization of  $\pi/4$  DQPSK MODEM Block Diagram

During testing, two EDFAs and two IF amplifiers were needed to generate enough ASE noise power for measuring the MODEM's BER performance up to  $10^{-3}$ . As illustrated, the two EDFAs are simply cascaded without any input signal at 1550 nm. ASE from EDFA 1 is amplified by EDFA 2, which also generate its own ASE; the sum of these two signals are available at the output of EDFA 2. This ASE optical power is detected by the photodiode, then amplified by two IF amplifiers. An attenuator is inserted between the amplifiers to prevent oscillation due to reflections. Note that during electrical amplification, additional thermal noise is added which further increases the total noise power. For BER measurements, the second attenuator can be adjusted to vary the amount of noise power and hence the eventual SNR level. A power combiner is used to combine the noise power and the  $\pi/4$  DQPSK signal at 1 GHz from the modulator. This combined signal is then fed to the demodulator to obtain BER measurements.

Figure 32 shows the BER versus SNR per bit curve obtained by varying the noise power level. To obtain the SNR per bit readings, the CNR value was first determined by measuring the carrier power with the base band modulation turned off (switching off the BER Test Set) then dividing through by the measured noise power at 1.0 GHz. The "noise marker" feature of the spectrum analyzer was employed to measure the single-

sided power spectral density  $N_o$ , which was then multiplied by the noise bandwidth of approximately 100 MHz (specified by the IF filter) to produce the measured noise power value. Eq. 3-18 can then be used to convert the measured CNR to SNR assuming that the noise bandwidth  $B_N$  is 100 MHz and the input bit rate  $f_b$  is 50 Mb/s. Note that the CNR in Eq. 3-18 must be multiplied by a factor of one-half to account for the power contribution from both I and Q channels.

$$SNR = \frac{B_N}{f_b} \cdot \frac{1}{2} CNR \quad \text{Eq. 3-18}$$

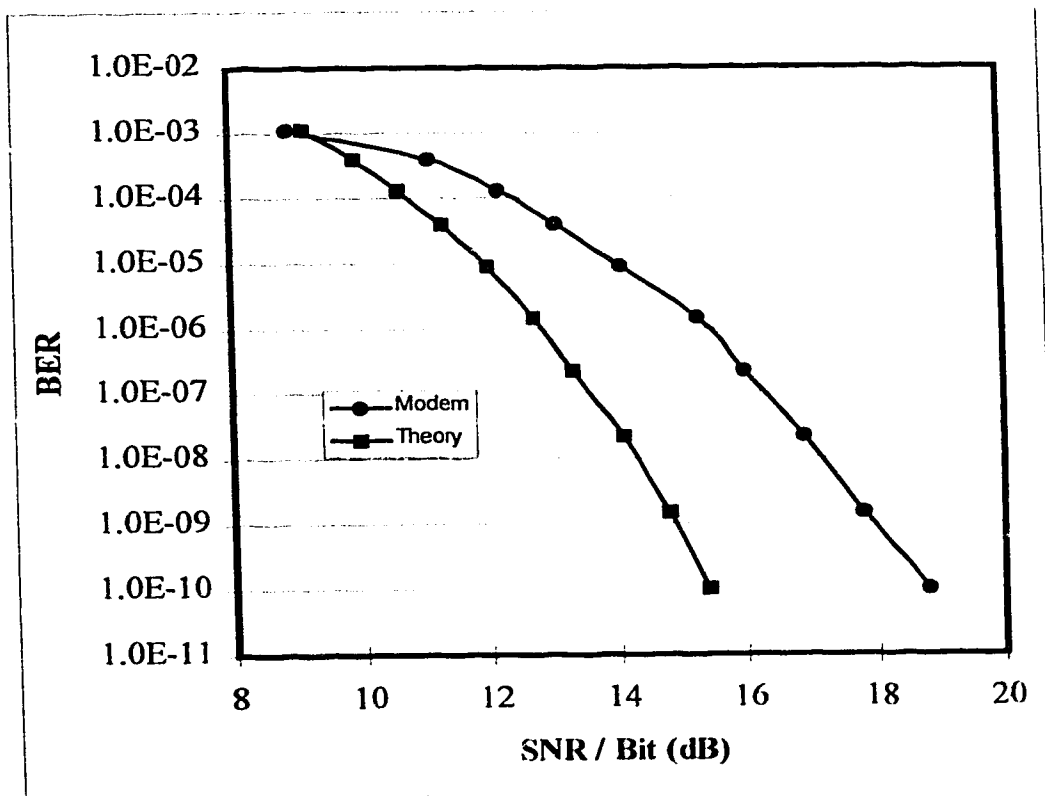


Figure 32: Performance of  $\pi/4$  DQPSK MODEM

From this figure, it is apparent that the MODEM's performance is sub-optimum. For example, the theoretical SNR value required to give a BER reading of  $10^{-10}$  is 15.4 dB whereas the actual SNR required is approximately 18.8 dB to produce the same BER. This difference of 3.4 dB is caused mainly by the assumption of a matched filter or an

integrate-and-dump demodulator used for the theoretical curve. The theoretical derivation of Eq. 3-16 is based on a demodulator architecture similar to the one shown in Figure 13 with the low pass filters replaced by matched filters (filters with impulse responses matched to the pulse shape of the base band signal) or integrate-and-dump circuits [31]. Since simple and commercially available low pass filters are used in the experiment, the performance of the demodulator can be expected to be sub-optimum. In addition, part of the discrepancy can probably be attributed to the use of non-ideal multipliers, splitter/combiner and phase shifter in the I & Q Phase Detector in contrast to the ideal components assumed in the derivation of Eq. 3-16. It is also likely that the decision timing adjustment did not provide enough resolution to allow for optimal decision setting, and the sensitivity of the decision circuitry may also be inadequate for lower BER counts. Nevertheless, the MODEM can still be used to analyze the validity of the proposed system as long as its performance limitation represented by Figure 32 is taken into account.

### 5.3 $\pi/4$ DQPSK Experiments

Figure 16 is shown here again to illustrate the experimental block diagram for the  $\pi/4$  DQPSK experiments. For these experiments,  $f_{IF}$  and  $f_{RF}$  are chosen to be 1.0 GHz and 4.1 GHz respectively resulting in the up-converted carrier at 16.4 GHz and information signal at 17.4 GHz. Six experiments were performed using the  $\pi/4$  DQPSK modulation format. Recall that Eq. 2-16 was derived by assuming that  $\epsilon = 0, \pm 1, \pm 2 \dots$  in Eq. 2-13, which means that the external modulator is biased at its maximum or minimum transmission points; the signal spectra of the system should therefore be the same under both bias conditions. In the first two experiments, the Mach-Zehnder modulator's DC bias point was set to 0 V for maximum transmission. The first experiment did not involve any optical fiber, while 25 km of fiber were inserted in the second experiment. In the third experiment, the DC bias point was set to  $V_{\pi}$  for minimum transmission to serve as a comparison to the first experiment. 50 km of fiber and an EDFA were used in the fourth experiment to investigate the long distance transmission characteristic of the



proposed up-conversion technique. BER versus optical loss measurements were obtained in the fifth experiment and finally, the dispersion effect of optical fiber was examined in the sixth experiment.

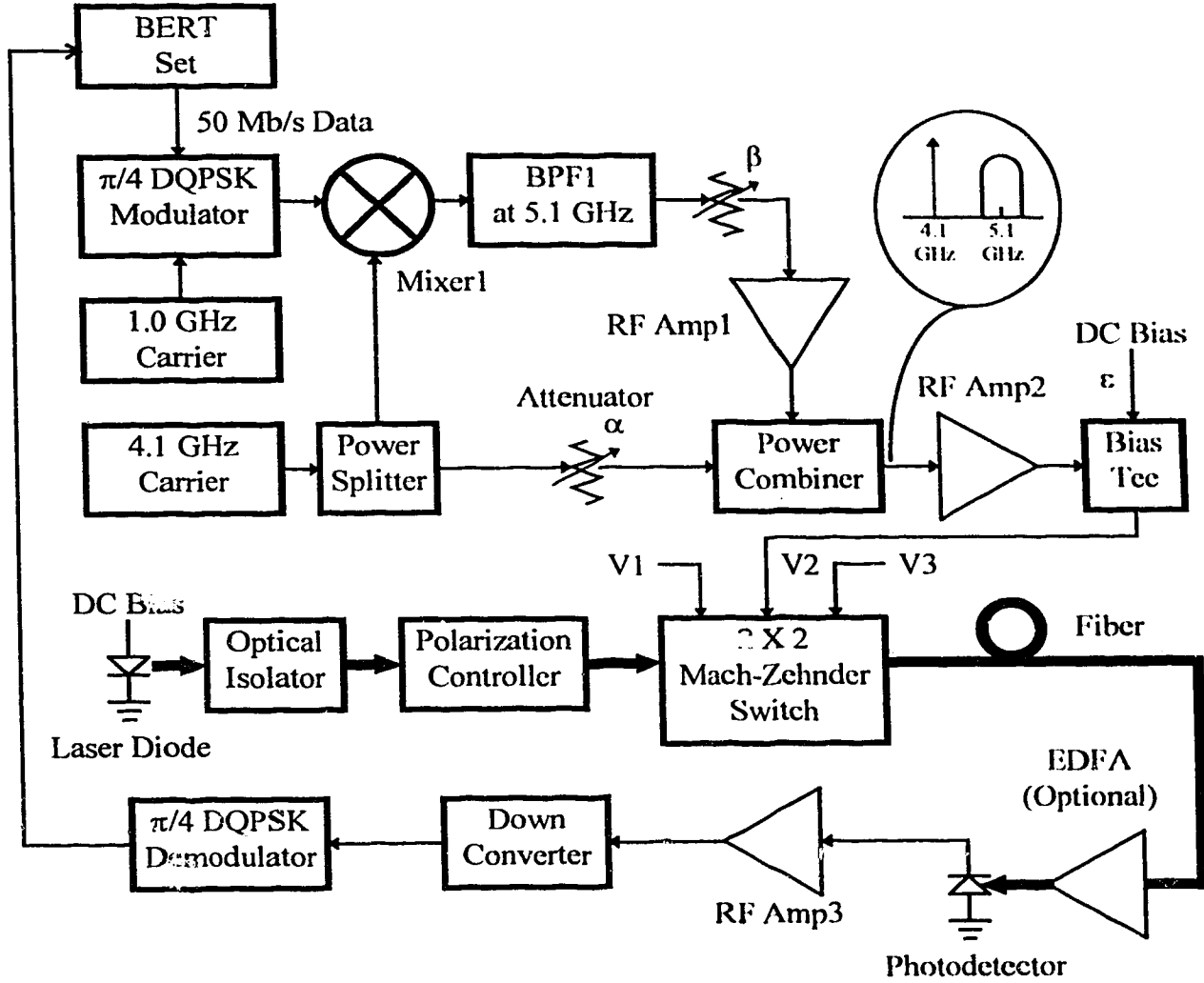


Figure 16:  $\pi/4$  DQPSK Experimental Setup Block Diagram

It is important to point out that for the first three experiments, it was not possible to obtain a BER versus SNR curve due to the unique setup in the receiver. A conventional method of obtaining BER versus SNR data usually involves the introduction of variable optical loss in the system via either a length of fiber or an optical attenuator for varying the received SNR. In this experimental setup, the desired signal is at 17.4 GHz and the

unmodulated carrier at 16.4 GHz is used as a LO source in the down converter as depicted in Figure 17. As described before, it is essential to maintain a constant +10 dBm input power level at the LO port of the microwave mixer in the down converter. Since both signals at 16.4 and 17.4 GHz undergo the same optical gain or loss through the system, the performance of the down converter is altered when the optical transmission loss is varied. In addition to the down converter mixer, the power at the LO port of the I & Q Phase Detector in the  $\pi/4$  DQPSK demodulator must also be kept at a constant + 10 dBm. This means that the receiver chain behaves differently under different received SNR levels, hence a BER versus SNR curve cannot be obtained unless there is enough received optical power or electrical amplification at 16.4 GHz so that electrical attenuators can be used to limit the LO inputs of the mixer and I & Q Phase Detector to +10 dBm. Since an additional electrical amplifier at 16.4 GHz was not available, an EDFA was needed to satisfy this power requirement and therefore a BER versus SNR curve was tabulated only for the last experiment. For the first four experiments, the system was simply tuned for best BER performance and the recorded measurements were used to compare against theoretical prediction. Although the dynamic range of the receiver is relatively small (only about 5 dB) even with an EDFA, it is noteworthy that the use of the up-converted 16.4 GHz LO signal eliminates the need of a second high frequency signal generator in the experiment while at the same time proving the possibility of using this up-converted signal as a LO source in a microcellular system.

### **5.3.1 Experiment #1: Maximum Transmission without Fiber and EDFA**

The purpose of the first experiment is to investigate the performance of the proposed up-conversion technique using the  $\pi/4$  DQPSK MODEM. In this experiment, the optical signal at the output of the Mach-Zehnder external modulator is immediately detected by the photodiode without any optical amplification or extensive fiber loss. Bias for the external modulator is set to the maximum transmission point of 0 V. Table 6 summarizes the experimental settings and measurements for this experiment.

Mach-Zehnder DC Bias	0 V (Max. Transmission)
RF Drive at 4.1 GHz ( $\beta$ )	25.2 dBm (1.47)
RF Drive at 5.1 GHz ( $\alpha$ )	11.2 dBm (0.29)
Received Optical Power (with Modulation)	-7.0 dBm
Received Optical Power (without Modulation)	-6.7 dBm
Received Carrier Power at 17.4 GHz	-66.0 dBm
Measured CNR at 1 GHz	15.4 dB
Measured BER	$1 \times 10^{-9}$

Table 6: Experimental Settings and Results for Experiment #1

The received carrier power of -66.0 dBm at 17.4 GHz in the above table is obtained by measuring the carrier power at the output of RF Amp4 with the base band modulation turned off (manually switching off the BER Test Set); the net gain of 62 dB (for RF Amp3, the RF power splitter, BPF2 and RF Amp4) is then subtracted from this measured carrier power to produce the received carrier power of -66 dBm referred to the output of the photodetector. Note also that an accurate CNR reading is available only at the output of the IF amplifier at 1.0 GHz since the received signal has gone through enough electrical gain at this point for the signal noise level to dominate over the spectrum analyzer's thermal noise floor. The technique described in the previous section for the characterization of the  $\pi/4$  DQPSK MODEM is used again to obtain the CNR reading at 1.0 GHz.

As a source of reference, the spectrum of the  $\pi/4$  DQPSK Modulating Signal at 5.1 GHz is shown in Figure 33. Figure 34 contains the spectrum of the up-converted signal at 17.4 GHz at the output of RF Amp4. The spectral similarity between the two figures confirms the proposed system's up-conversion capability for relatively wide-band phase modulated signal. Figure 35 illustrates the up-converted carrier at 16.4 GHz at the input to Mixer 2. In addition to the spectral purity of this signal, it is noteworthy that it can be amplified up to +10 dBm without the use of optical amplifiers; this verifies the concept of using this unmodulated carrier as the LO source in the up-link direction of a microcellular system.

Figure 36 depicts the received  $\pi/4$  DQPSK spectrum after it has been down-converted to 1.0 GHz; it is evident that the spectral shape is preserved up to the cutoff frequencies ( $1.0 \text{ GHz} \pm 50 \text{ MHz}$ ) of the IF filter at the output of the down converter. Using the same method described in the previous section, the measured CNR of 15.4 dB at 1.0 GHz translates to the SNR of 18.4 dB, and the corresponding measured BER is  $1 \times 10^{-9}$ . Referring to Figure 32, which plots the BER versus SNR curve with the MODEM connected back-to-back at 1.0 GHz, it is apparent that the measured SNR of 18.4 dB is quite close to the MODEM performance limit of 17.9 dB to give  $1 \times 10^{-9}$  BER. In comparison, the theoretical SNR value required to give the BER of  $1 \times 10^{-9}$  is approximately 14.9 dB according to Eq. 3-16. The difference of 3.5 dB between the theoretical and measured SNR is consistent with the difference depicted in Figure 32. It can therefore be concluded that the system is limited by the MODEM performance and that the up-conversion technique is basically transparent to the  $\pi/4$  DQPSK signal. It is noteworthy that the received SNR of 18.4 dB and BER of  $1 \times 10^{-9}$  are both more than adequate for wireless applications.

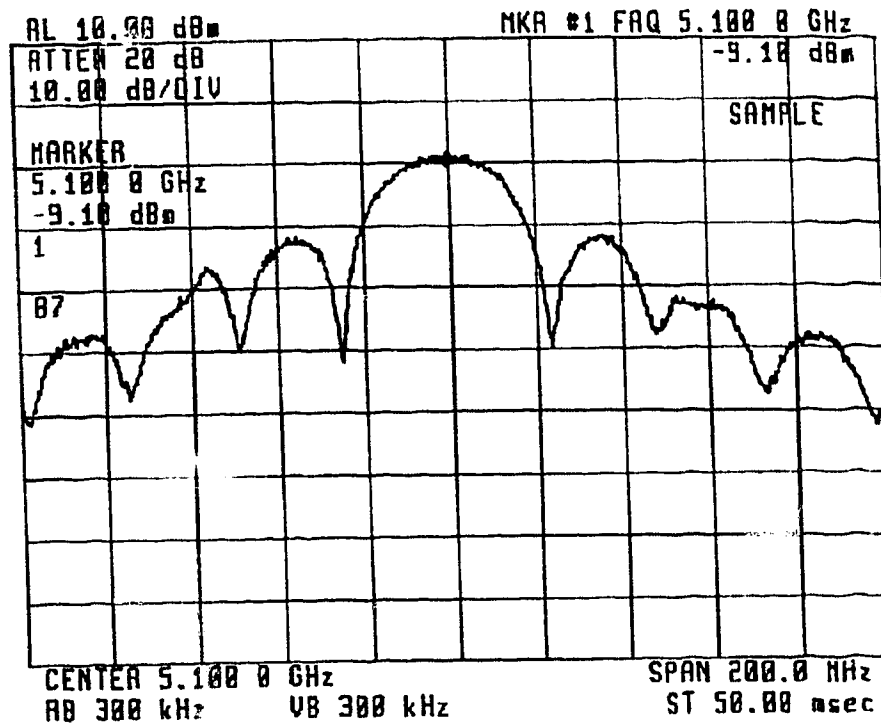


Figure 33:  $\pi/4$  DQPSK Modulating Signal at 5.1 GHz

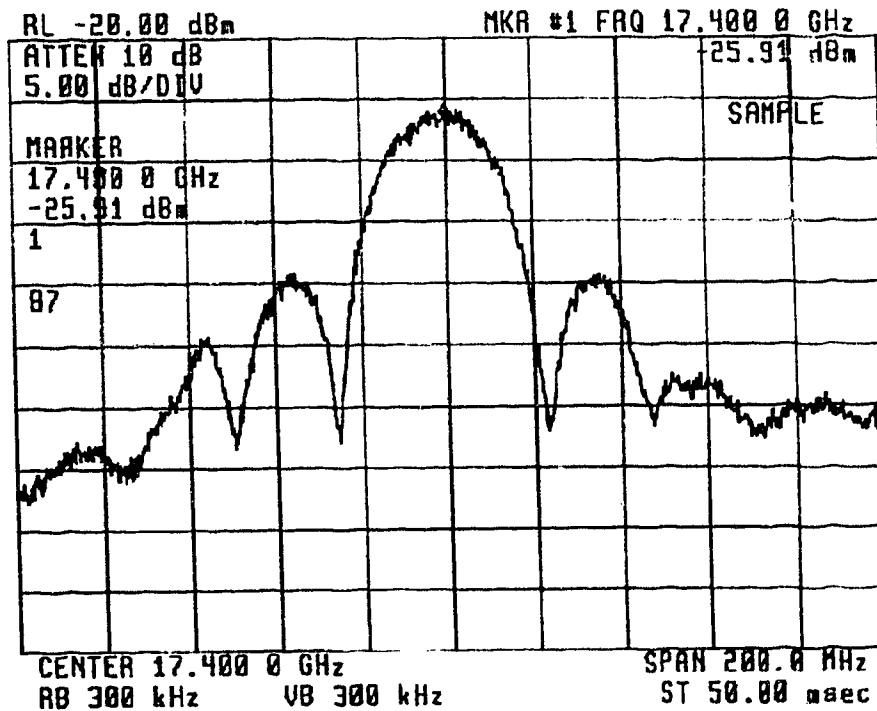


Figure 34:  $\pi/4$  DQPSK Spectrum at 17.4 GHz (no fiber, no EDFA)

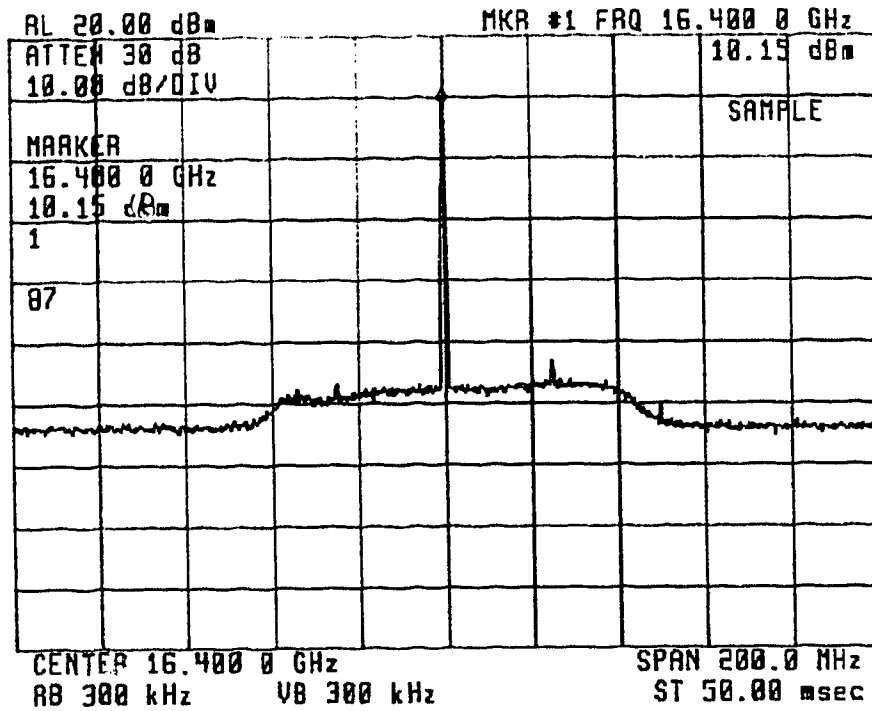


Figure 35: Unmodulated Carrier at 16.4 GHz (no fiber, no EDFA)

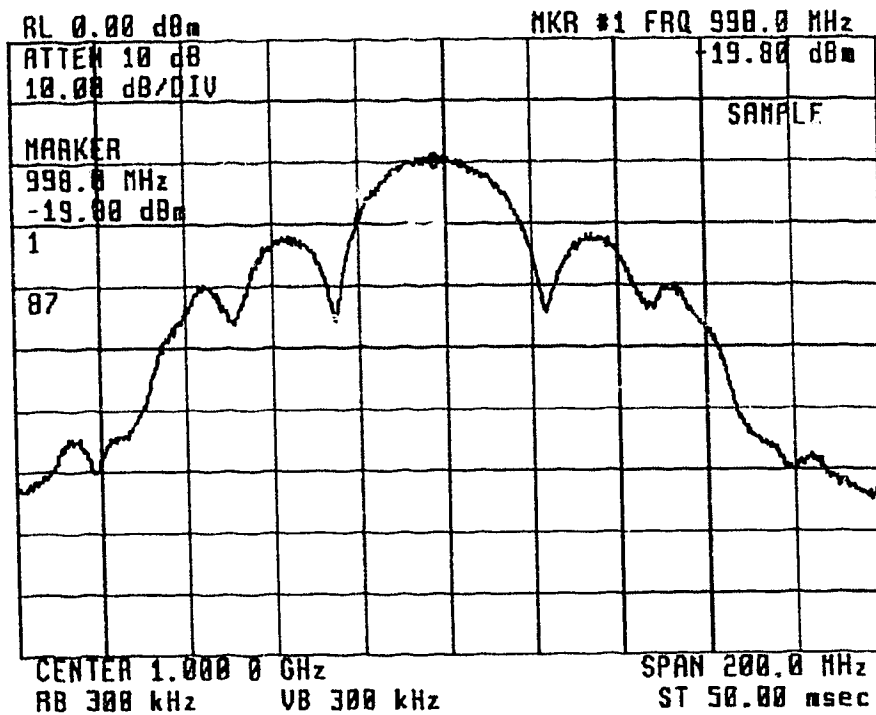


Figure 36: Down-converted Spectrum at 1.0 GHz (no fiber, no EDFA)

Table 7 summarizes the noise term contributions referred to the output of the photodiode. The noise current densities are expressed as average noise power in dBm using the following relationships derived from Eq. 4-5, Eq. 4-7 and Eq. 4-8. In the following equations,  $N_{th}$ ,  $N_{RIN}$  and  $N_{shot}$  are the average thermal noise power, laser RIN power, and signal shot noise power respectively. In addition,  $P_d$  is the average modulated optical of -7.0 dBm power at the photodiode.

$$\begin{aligned}
 N_{th} &= 10 \cdot \log(i_{th}^2 \cdot R \cdot 1000 \cdot B_N) \\
 &= 10 \cdot \log\left(\frac{4kTF}{R} \cdot R \cdot 1000 \cdot 100 \times 10^6\right) \\
 &= 10 \cdot \log(4 \cdot 1.38 \times 10^{-23} \cdot 300 \cdot 1.91 \cdot 1000 \cdot 100 \times 10^6) \\
 &= -85.0 \text{ dBm}
 \end{aligned}
 \tag{Eq. 5-1}$$

$$\begin{aligned}
 N_{RIN} &= 10 \cdot \log(i_{RIN}^2 \cdot R \cdot 1000 \cdot B_N) \\
 &= 10 \cdot \log\left(RIN(P_d \Re)^2 \cdot 50 \cdot 1000 \cdot 100 \times 10^6\right) \\
 &= 10 \cdot \log\left(1.26 \times 10^{-14} (2.0 \times 10^{-4} \cdot 0.5)^2 \cdot 5 \times 10^{12}\right) \\
 &= -92.0 \text{ dBm}
 \end{aligned}
 \tag{Eq. 5-2}$$

$$\begin{aligned}
 N_{shot} &= 10 \cdot \log(i_{shot}^2 \cdot R \cdot 1000 \cdot B_N) \\
 &= 10 \cdot \log(2q\Re P_d \cdot 50 \cdot 1000 \cdot 100 \times 10^6) \\
 &= 10 \cdot \log(1.6 \times 10^{-19} \cdot 0.5 \cdot 2.0 \times 10^{-4} \cdot 5 \times 10^{12}) \\
 &= -98.0 \text{ dBm}
 \end{aligned}
 \tag{Eq. 5-3}$$

Thermal Noise Power	-85.0 dBm
Signal Shot Noise Power	-98.0 dBm
RIN Power	-92.0 dBm
Total Noise Power	-84.0 dBm

Table 7: Noise Contribution for Experiment #1

To calculate the average signal power at 17.4 GHz, Eq. 4-10 can be used.

$$P_{sig} = [J_1(\pi\alpha)J_3(\pi\beta)]P_d \quad \text{Eq. 4-10}$$

Since this equation was derived using the ideal Mach-Zehnder characteristic, if the measured CNR level agrees well with the theoretical CNR level calculated using this equation, it can be concluded that the E-tek Electro-optic Switch can indeed be modeled as a Mach-Zehnder modulator.

The average carrier power at 17.4 GHz in dBm can be expressed as

$$\begin{aligned} C_{17.4 \text{ GHz}} &= 10 \cdot \log \left[ \frac{1}{2} (P_{sig} \cdot \Re)^2 \cdot R \cdot 1000 \right] \\ &= 10 \cdot \log \left[ \frac{1}{2} ([J_1(\pi\alpha)J_3(\pi\beta)]P_d \cdot \Re)^2 \cdot R \cdot 1000 \right] \\ &= 10 \cdot \log \left[ \frac{1}{2} ([0.172]P_d \cdot 0.5)^2 \cdot 50 \cdot 1000 \right] \\ &= -50.7 \text{ dBm} \end{aligned} \quad \text{Eq. 5-4}$$

where  $P_d$  is now the *unmodulated* optical power of -6.7 dBm giving the average carrier power of -50.7 dBm at 17.4 GHz using the measured  $\alpha$  and  $\beta$  values. When the theoretical noise power of -84.0 dBm is subtracted from this carrier power, a theoretical CNR of 33.3 dB is obtained, which is significantly greater than the measured value of 15.4 dB at 1.0 GHz. Note that this theoretical CNR is referred to the output of the photodiode; it is compared with the CNR at 1.0 GHz instead of the CNR at the output of the photodiode at 17.4 GHz because it is not possible to directly measure the CNR at 17.4 GHz. This is a result of the spectrum analyzer's noise floor which dominates over the signal noise levels at the outputs of RF Amp2 and RF Amp4 thus preventing accurate noise measurements at these points. The relatively large difference in CNRs suggests that the E-tek Electro-optic Switch cannot be considered as a pure Mach-Zehnder modulator, especially near the non-linear operation regions. Since the  $\beta$  value used is relatively large, it can be postulated that the E-tek Electro-optic Switch must have the exact sinusoidal transfer function defined by Eq. 2-9 over a large input modulating



voltage range if Eq. 4-10 is to be used in predicting the up-converter harmonic power. Furthermore, Eq. 2-9 assumes that the Mach-Zehnder modulator behaves the same under both static and dynamic conditions without taking into account the frequency response of the device; this may not be valid since the electrodes of the Mach-Zehnder modulator must have some frequency dependent characteristics. Nevertheless, it was observed that the desired harmonics are maximized when the DC bias is set to the maximum transmission point as predicted for a Mach-Zehnder modulator, so the E-tek Electro-optic Switch can still be described qualitatively by the Mach-Zehnder interferometer characteristic. As a final check, if the calculated total noise power of -84 dBm is subtracted from the measured average RF power of -66 dBm at 17.4 GHz, a CNR of 18.0 dB is obtained which is closer to the measured value of 15.4 dB. This verifies that at least the noise characteristics of the system are behaving according to theory.

Finally, the eye diagrams corresponding to the  $I_n$  and  $Q_n$  decision variables for the demodulated  $\pi/4$  DQPSK signal are shown in Figure 37. It can be qualitatively concluded that the BER associated with such eye diagrams should be minimal and the amount of time jitter is also negligible since the eye opening can be easily identified.

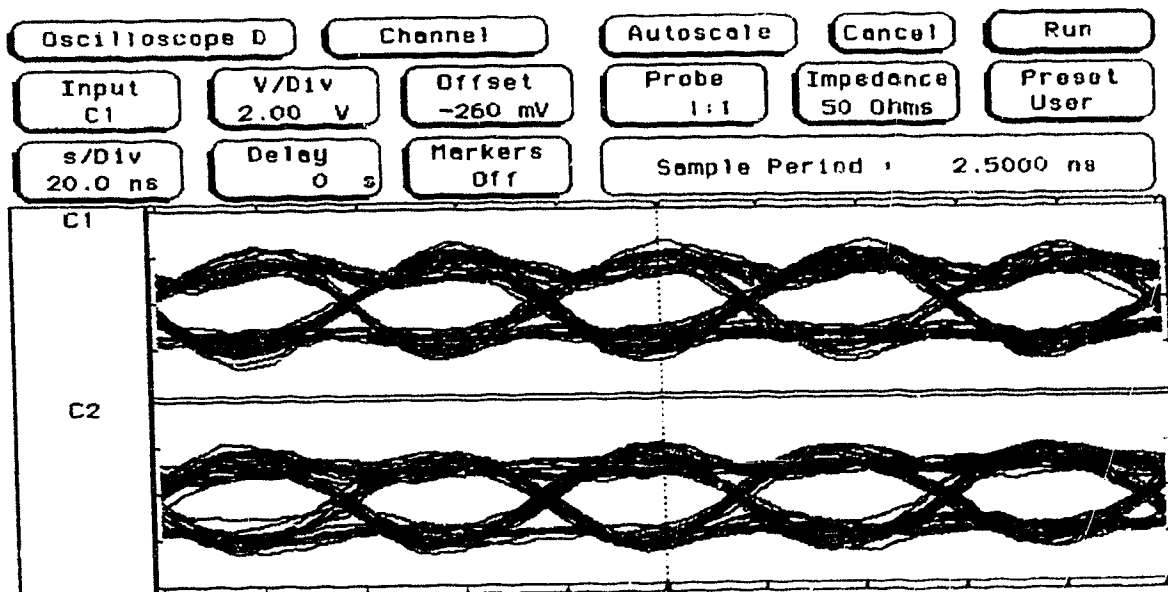


Figure 37: Eye Diagrams for Decision Variables (no fiber, no EDFA)

### 5.3.2 Experiment #2: Maximum Transmission with 25 km Fiber

The purpose of the second experiment is to investigate the performance of the proposed up-conversion technique with the addition of optical fiber. In this experiment, 25 km of optical fiber are inserted after the Mach-Zehnder external modulator and the output optical signal from the fiber is detected by the photodiode without any optical amplification. Again the external modulator is biased at its maximum transmission point of 0 V. Table 8 lists the experimental settings and measurements for this experiment.

Mach-Zehnder DC Bias	0 V (Max. Transmission)
RF Drive at 4.1 GHz ( $\beta$ )	27.6 dBm (1.94)
RF Drive at 5.1 GHz ( $\alpha$ )	12.8 dBm (0.35)
Fiber Loss	5.5 dB
Received Optical Power (with Modulation)	-15.6 dBm
Received Optical Power (without Modulation)	-10.7 dBm
Received Carrier Power at 17.4 GHz	-70.2 dBm
Measured CNR at 1 GHz	14.6 dB
Measured BER	$2 \times 10^{-7}$

Table 8: Experimental Settings and Results for Experiment #2

With the introduction of optical loss, it was necessary to readjust the RF drive power ( $\alpha$  and  $\beta$ ) to increase the amount of power at 16.4 GHz since the LO port of Mixer 2 must be kept at +10 dBm. The received unmodulated carrier at 16.4 GHz and  $\pi/4$  DQPSK signal at 17.4 GHz are shown in Figure 39 and Figure 38 respectively. Note that even after 25 km of dispersive fiber, the spectral shape of the  $\pi/4$  DQPSK signal is identical to the results obtained in the previous experiment. This suggests that it is possible to use the proposed up-conversion technique to distribute microwave signals in the feeder network of a microcellular system.

Figure 40 illustrates the spectrum of the down-converted  $\pi/4$  DQPSK signal at 1.0 GHz. The measured BER for this signal is  $2 \times 10^{-7}$ , and the measured CNR is 14.6 dB which translates to an SNR level of 17.6 dB. In comparison, the theoretical SNR value required for a BER of  $2 \times 10^{-7}$  is 13.5 dB. The 4.1 dB difference is close to the 3.5 dB observed when no fiber was used and hence it can probably be attributed to the same sources as described before. To confirm this, Figure 32 can again be used to shown that with the MODEM connected back-to-back the SNR required to produce the BER of  $2 \times 10^{-7}$  is 16.0 dB. This compares quite well with the measured SNR of 17.6 dB, so it can be concluded that the  $\pi/4$  DQPSK signal is not degraded by the up-conversion technique over 25 km of fiber. Finally, the eye diagrams for the decision variables are shown in Figure 41. Even though the eyes are smaller than the ones in Figure 37 (note that the voltage scale is 1 V/div instead of 2 V/div) due to additional optical loss introduced by the fiber, there is still enough eye opening (or SNR) for accurate decisions giving the BER of  $2 \times 10^{-7}$ , which is also adequate for wireless applications.

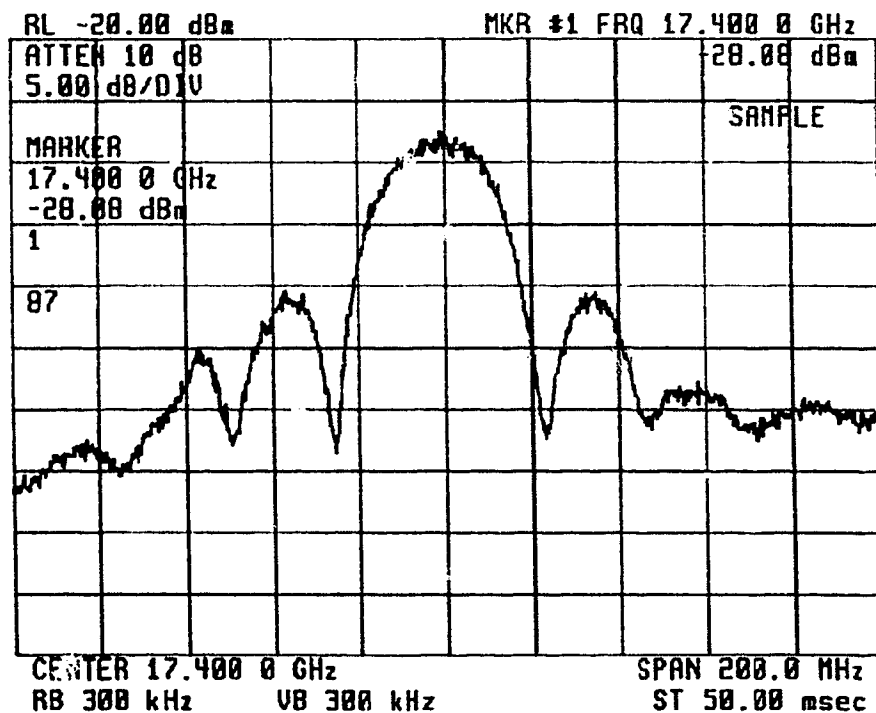


Figure 38:  $\pi/4$  DQPSK Spectrum at 17.4 GHz (with 25 km fiber, no EDFA)

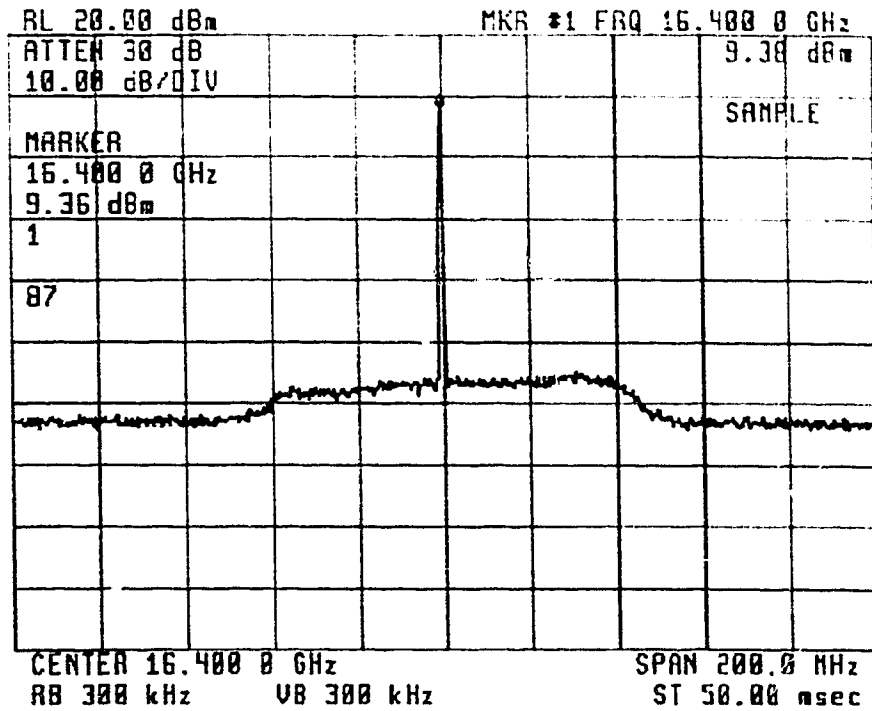


Figure 39: Unmodulated Carrier at 16.4 GHz (with 25 km fiber, no EDFA)

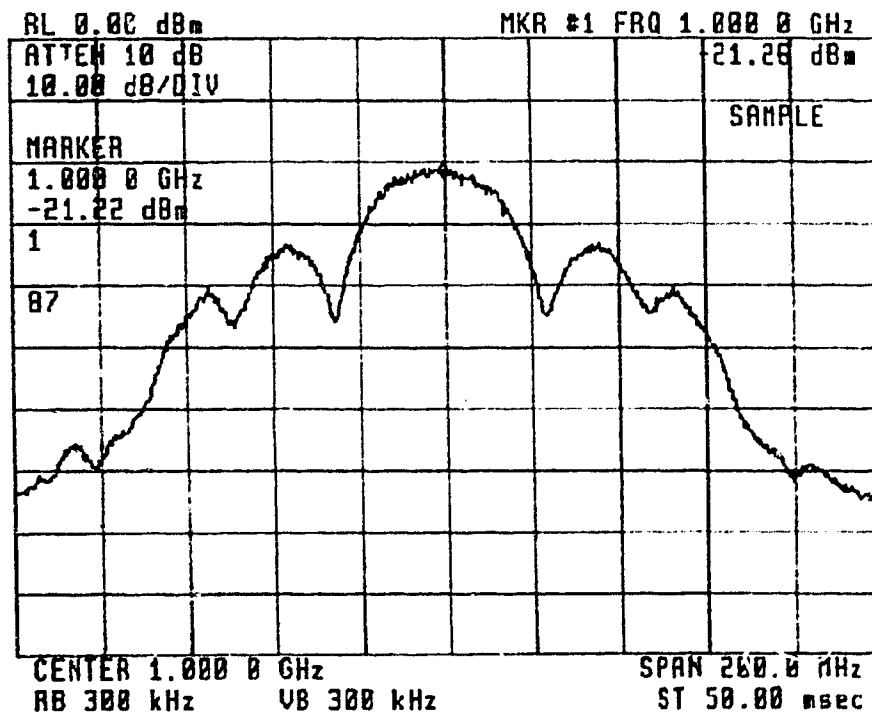


Figure 40: Down-converted Spectrum at 1.0 GHz (with 25 km fiber, no EDFA)

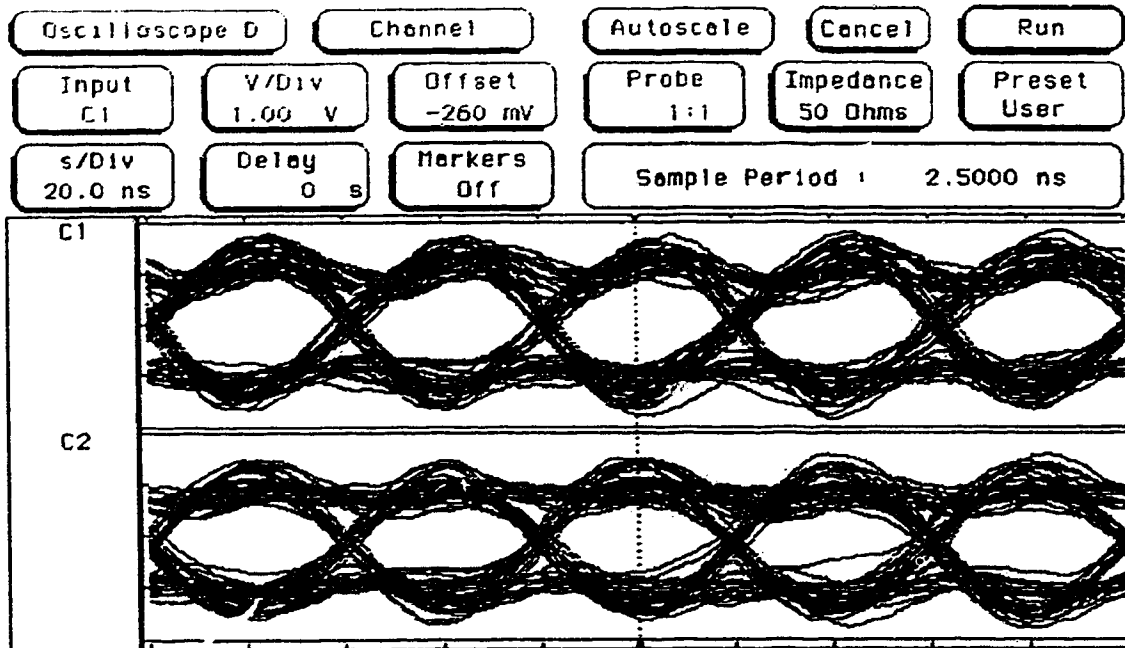


Figure 41: Eye Diagrams for Decision Variables (with 25 km fiber, no EDFA)

Thermal Noise Power	-85.0 dBm
Signal Shot Noise Power	-106.6 dBm
RIN Power	-109.2 dBm
Total Noise Power	-85.0 dBm

Table 9: Noise Contribution for Experiment #2

Table 9 lists the noise term contributions referred to the photodiode for this experiment using equations 5-1 to 5-3. The theoretical CNR obtained by subtracting the calculated noise power from the theoretical carrier power in Eq. 5-4 is 13.3 dB, which is quite close to the experimental value of 14.6 dB at 1.0 GHz. However, since there is a significant discrepancy between the measured and theoretical CNRs in the previous experiment, the validity in modeling the E-tek 2X2 switch as an ideal Mach-Zehnder external modulator is still undetermined at this point. On the other hand, if the calculated noise power of -85 dBm is subtracted from the measured average received power of -70.2 dBm at 17.4 GHz,

a CNR value of 13.8 dB is obtained, which agrees well with the measured value and therefore confirms the noise performance of the system.

### 5.3.3 Experiment #3: Minimum Transmission without Fiber and EDFA

As discussed in the beginning of section 5.3, the proposed up-conversion technique should perform equally as well with the external modulator biased at either its maximum or minimum transmission point. One of the advantages for setting the DC bias at minimum is that less optical noise (shot noise, RIN noise, etc.) will be generated since the average optical power is also minimized. It is therefore reasonable to assume that the BER performance for this experiment should be superior to that of the first experiment if optical noise is the dominant noise term. However, Table 7 and Table 9 clearly show that thermal noise is the strongest noise component in the previous experiments, hence the performance of the system under the two different DC bias conditions should be similar since this noise term remains constant in both cases. To verify this hypothesis, the Mach-Zehnder modulator is biased at its minimum transmission point in this experiment and the experimental results are compared with the ones obtained in the first experiment with the modulator biased at its maximum transmission point. Table 10 summarizes the experimental settings and measurements for this experiment.

Mach-Zehnder DC Bias	3.9 V (Min. Transmission)
RF Drive at 4.1 GHz ( $\beta$ )	25.2 dBm (1.47)
RF Drive at 5.1 GHz ( $\alpha$ )	12.3 dBm (0.33)
Received Optical Power (with Modulation)	-9.1 dBm
Received Optical Power (without Modulation)	-13.0 dBm
Received Carrier Power at 17.4 GHz	-66.6 dBm
Measured CNR at 1 GHz	15.6 dB
Measured BER	$1 \times 10^{-10}$

Table 10: Experimental Settings and Results for Experiment #3

It is evident that the spectra shown in Figure 42 to Figure 44 are consistent with the ones obtained with the external modulator biased at its maximum transmission point. The measured CNR of 15.6 dB at 1.0 GHz translates to the SNR value of 18.6 dB, and the corresponding measured BER is  $1 \times 10^{-10}$ . This again agrees closely with the MODEM's back-to-back SNR requirement of 18.7 dB to give the same BER reading using Figure 32. Note that this BER measurement is right at the limit of the display precision of the BER Test Set and is only an estimated value since the readings tend to fluctuate around this reading resulting in "error free" measurement at times. Table 11 summarizes the noise contribution for this experiment again using equations 5-1 to 5-3. In spite of the fact that the optical noise terms have decreased in comparison to the first experiment (see Table 9), the total noise power changes by less than 1 dB since thermal noise is the dominant noise term. So the measured SNRs for the first and this experiments are almost identical (18.4 versus 18.6 dB). In addition, even though the averaged received optical power is less (-9.1 dBm to -7.0 dBm) in this experiment, the received SNR values are almost the same for both cases. In summary, this experiment proves that the proposed up-conversion technique indeed operates under both DC bias conditions, and that the SNR obtained by biasing at the minimum transmission point is indeed similar to the one achieved at the maximum transmission point if thermal noise is the dominate noise factor.

Using Eq. 5-4 and the calculated noise power of -84.9 dBm, the theoretical CNR of 30.2 dB can be obtained using the measured  $\alpha$  and  $\beta$  values. This deviates significantly from the measured CNR of 15.6 dB, hence it can be concluded that the E-tek 2X2 switch cannot be perfectly modeled as a Mach-Zehnder external modulator.

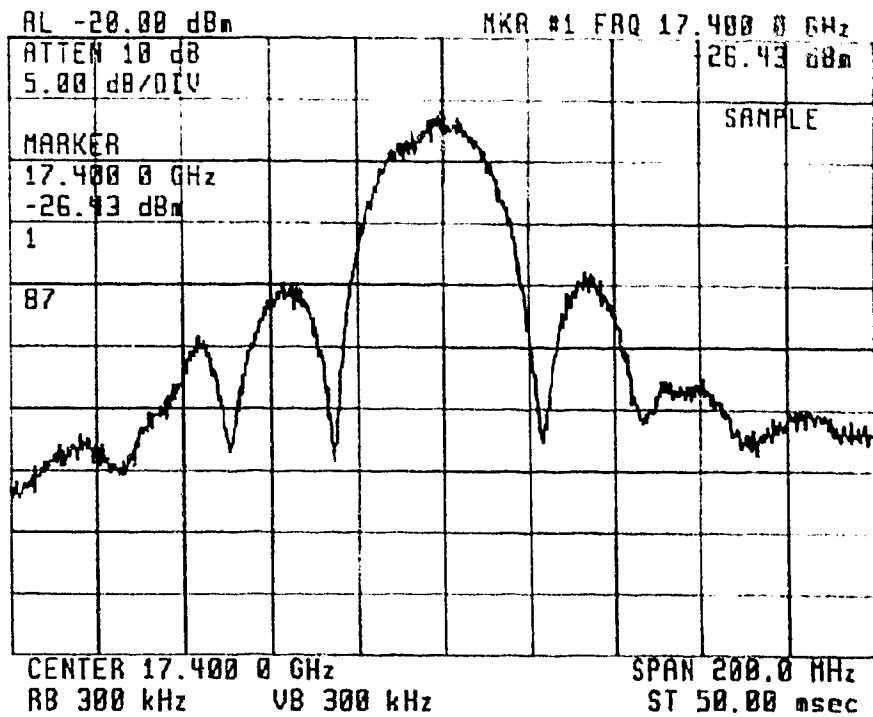


Figure 42:  $\pi/4$  DQPSK Spectrum at 17.4 GHz (no fiber, no EDFA)

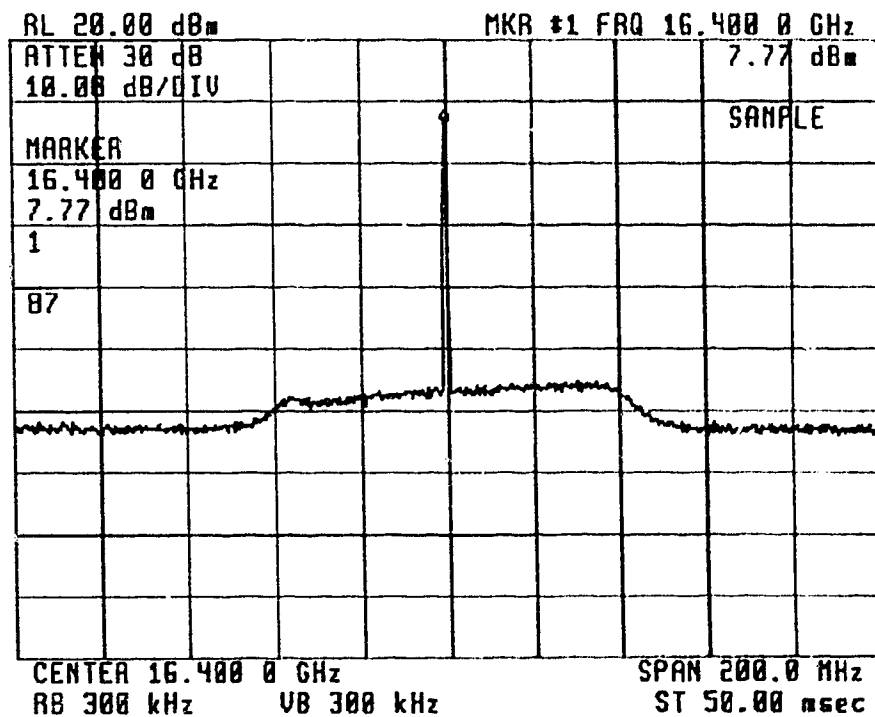


Figure 43: Unmodulated Carrier at 16.4 GHz (no fiber, no EDFA)



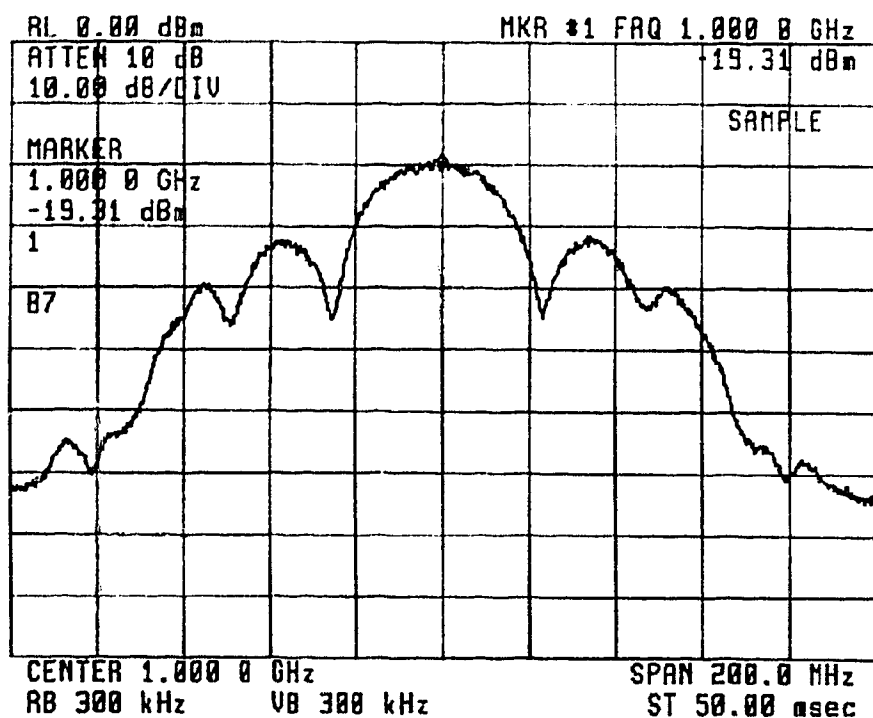


Figure 44: Down-converted Spectrum at 1.0 GHz (no fiber, no EDFA)

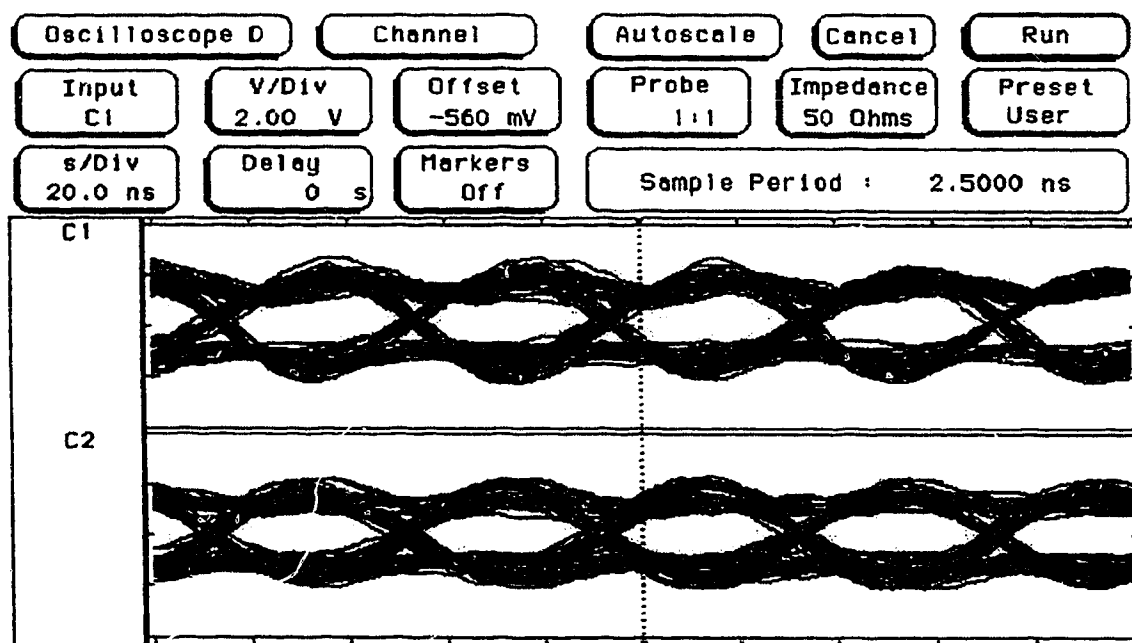


Figure 45: Eye Diagrams for Decision Variables (no fiber, no EDFA)

Thermal Noise Power	-85.0 dBm
Signal Shot Noise Power	-104.0 dBm
RIN Power	-104.0 dBm
Total Noise Power	-84.9 dBm

Table 11: Noise Contribution for Experiment #3

#### 5.3.4 Experiment #4: Maximum Transmission with 50 km Fiber and EDFA

This experiment explores the feasibility of using the proposed up-conversion technique for longer distance transmission using an optical amplifier. Here, 50 km of optical fiber are inserted after the external modulator and an EDFA is used prior to the photodiode as a pre-amplifier. Table 12 summarizes the experimental settings and results for this experiment.

Mach-Zehnder DC Bias	0 V (Max. Transmission)
RF Drive at 4.1 GHz ( $\beta$ )	26.1 dBm (1.64)
RF Drive at 5.1 GHz ( $\alpha$ )	9.0 dBm (0.23)
Fiber Loss	12.0 dB
EDFA Input Power (with Modulation)	-20.0 dBm
EDFA Gain	13.0 dB
Received Optical Power (with Modulation)	-10.6 dBm
Received Optical Power (without Modulation)	-7.6 dBm
Received Carrier Power at 17.4 GHz	-66.0 dBm
Measured CNR at 1 GHz	14.5 dB
Measured BER	$2 \times 10^{-10}$

Table 12: Experimental Settings and Results for Experiment #4

The received  $\pi/4$  DQPSK signal at 17.4 GHz and unmodulated carrier at 16.4 GHz are shown in Figure 46 and Figure 47 respectively. Observe that even after 50 km of dispersive fiber, the spectral shape of the  $\pi/4$  DQPSK signal is still preserved. Figure 48 illustrates the spectrum of the down-converted  $\pi/4$  DQPSK signal at 1.0 GHz with the corresponding demodulated eye diagrams shown in Figure 49. The measured BER for this signal is  $2 \times 10^{-10}$  and the measured CNR is 14.5 dB giving the SNR of 17.5 dB. In comparison, the theoretical SNR required for a BER of  $2 \times 10^{-10}$  is 15.2 dB. This discrepancy of 2.3 dB between the theoretical and measured SNR is less than the one obtained for the first two experiments of 3 to 4 dB. A possible explanation for this is that the optical noise power is more dominant with the use of an EDFA, hence the received signal is less sensitive to the electrical noise added by the non-ideal demodulator. In comparison to the MODEM performance, Figure 32 can be used to show that the SNR of 18.4 dB is required to give the BER of  $2 \times 10^{-10}$  with the MODEM connected back-to-back. Since the experimental value of 17.5 dB is actually better than the MODEM performance limit, it can be concluded the up-conversion system is transparent to the  $\pi/4$  DQPSK signal even with the use of 50 km of fiber and an EDFA. The small difference of 0.9 dB between the measured SNR and the MODEM limit is probably caused by measurement uncertainties in the experiment and in the characterization of the MODEM. A possible explanation for the apparent improvement in system performance over the MODEM limit is the effect of the overall transfer characteristic of the up-conversion system. It is well known that a raised cosine transfer function is desirable in a communication system for the elimination of inter-symbol interference (ISI) [41]. As the system comprises of many blocks each having a unique frequency response, the cascading effect of all of the system blocks may resemble a raised cosine transfer function more closely than the case where the modulator and demodulator are connected back-to-back, hence better BER performance is obtained.

Table 13 summarizes the calculated average noise power for each of the individual noise terms referred to the photodiode output using equations 5-1 to 5-3 with the addition of the following ASE beat noise power based on equations 4-2 and 4-4

$$\begin{aligned}
N_{sp-sp} &= 10 \cdot \log \left( i_{sp-sp}^2 \cdot R \cdot 1000 \cdot B_N \right) \\
&= 10 \cdot \log \left( 4 B_o \left[ N_{sp} \eta L (G-1) q \right]^2 \cdot 50 \cdot 1000 \cdot 100 \times 10^6 \right) \\
&= 10 \cdot \log \left( 4 \cdot 2.37 \times 10^{11} \left[ 1.26 \cdot 0.4 \cdot 0.44 (20-1) 1.6 \times 10^{-19} \right]^2 \cdot 5 \times 10^{13} \right) \\
&= -116.7 \text{ dBm}
\end{aligned}$$

Eq. 5-5

$$\begin{aligned}
N_{sig-sp} &= 10 \cdot \log \left( i_{sig-sp}^2 \cdot R \cdot 1000 \cdot B_N \right) \\
&= 10 \cdot \log \left( \frac{4q^2}{h\nu} \eta^2 L^2 P_{EDFA} N_{sp} (G-1) G \cdot 50 \cdot 1000 \cdot 100 \times 10^6 \right) \\
&= 10 \cdot \log \left( \frac{4 \cdot (1.6 \times 10^{-19})^2 (0.4)^2 (0.44)^2 (1 \times 10^{-5}) (1.26) (20-1) (20) 5 \times 10^{13}}{6.63 \times 10^{-34} \cdot 1.93 \times 10^{14}} \right) \\
&= -92.4 \text{ dBm}
\end{aligned}$$

Eq. 5-6

where  $N_{sp-sp}$  and  $N_{sig-sp}$  are the spontaneous-spontaneous and signal-spontaneous beat noise power respectively. If the calculated total noise power of -84.1 dBm is subtracted from the measured average signal power of -66.0 dBm, a CNR value of 18.1 dB is obtained which is relatively close to the measured value of 14.5 dB, so the noise characteristic of the system is behaving as predicted. The theoretical CNR of 27.9 dB can be obtained by subtracting the theoretical noise power of -84.1 dBm from the carrier power calculated using Eq. 5-4. This differs significantly from the measured CNR of 14.5 dB hence again confirming that the E-tek 2X2 switch is not an ideal Mach-Zehnder modulator.

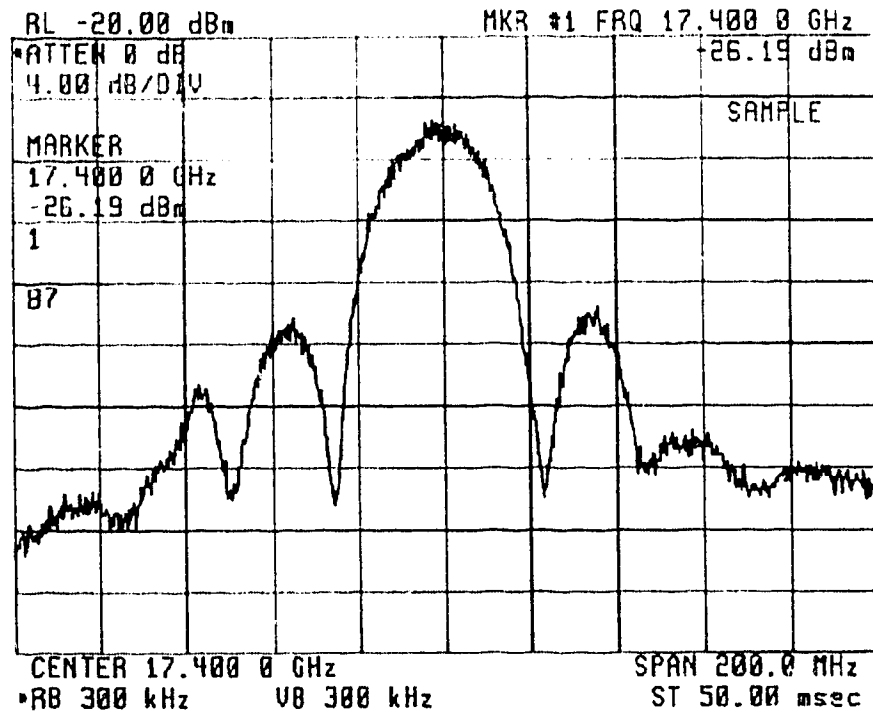


Figure 46:  $\pi/4$  DQPSK Spectrum at 17.4 GHz (with 50 km fiber and EDFA)

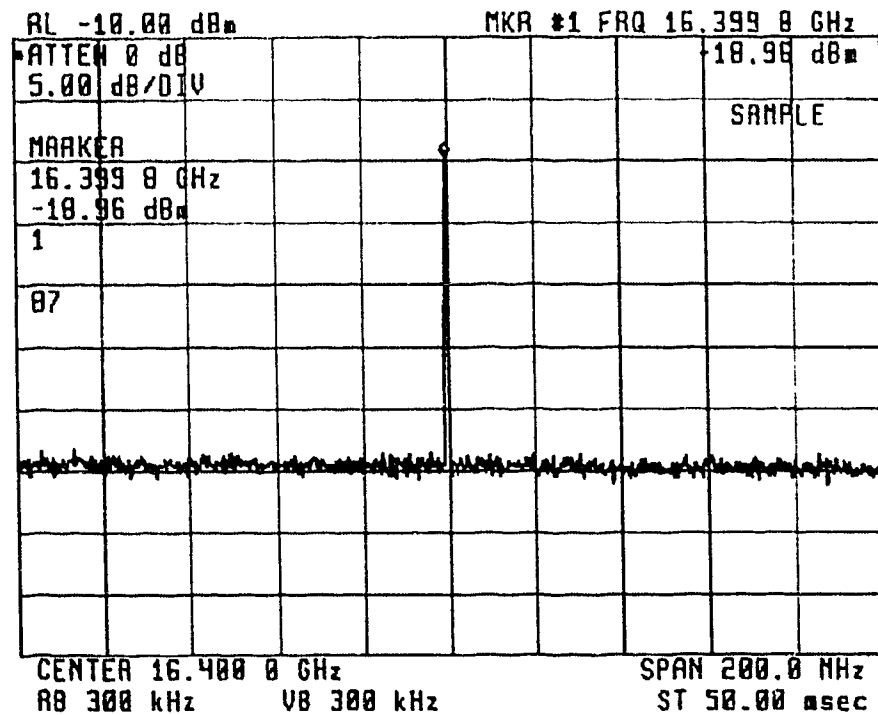


Figure 47: Unmodulated Carrier at 16.4 GHz (with 50 km fiber and EDFA)

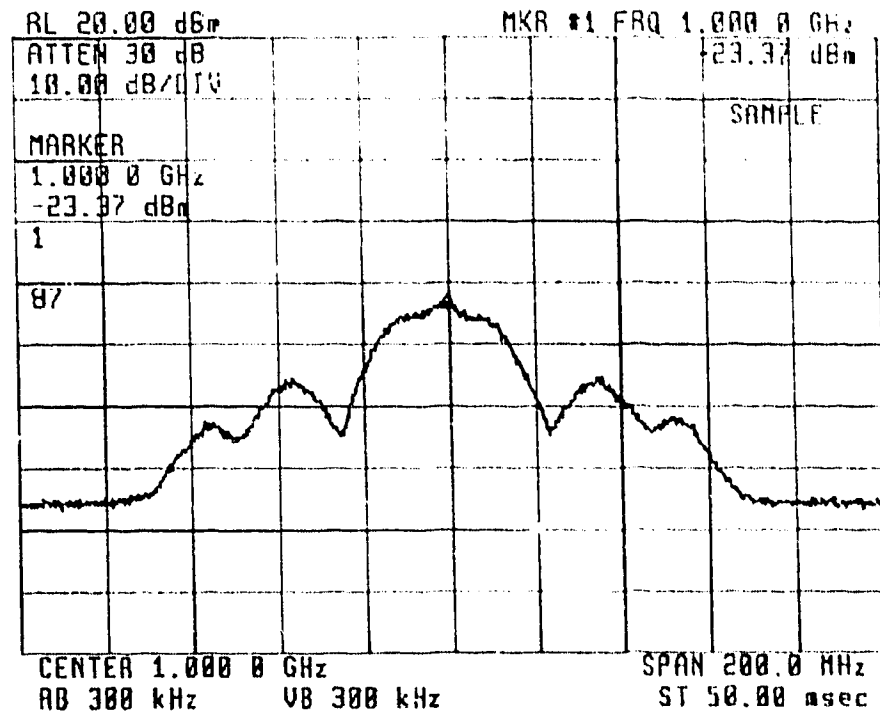


Figure 48: Down-converted Spectrum at 1.0 GHz (with 50 km fiber and EDFA)

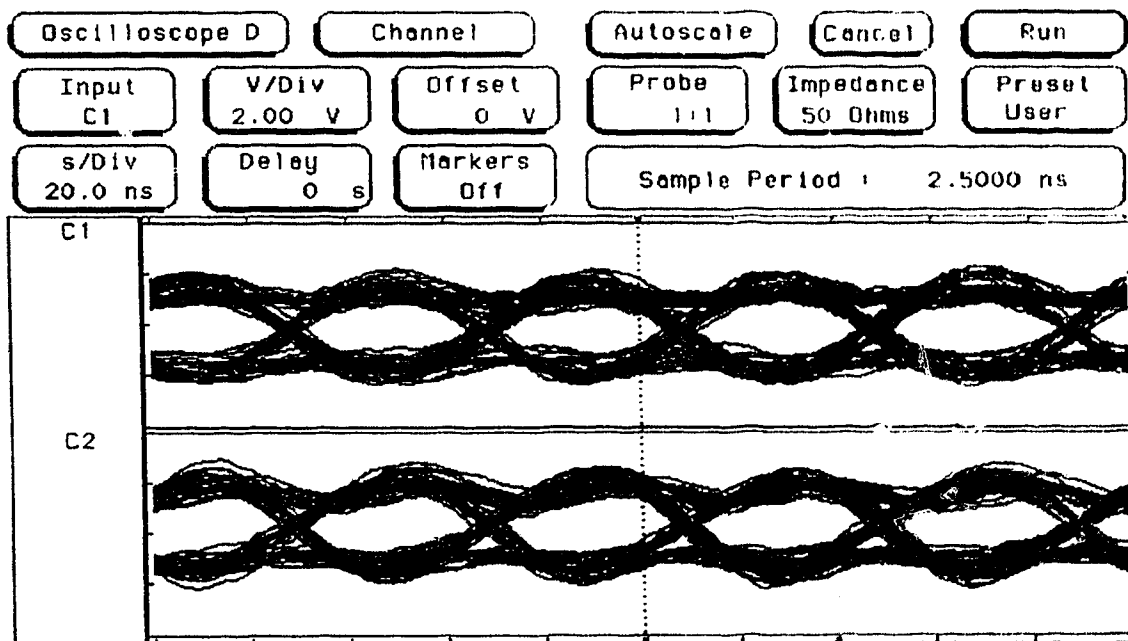


Figure 49: Eye Diagrams for Decision Variables (with 50 km fiber and EDFA)

Thermal Noise Power	-85.0 dBm
Signal and ASE Shot Noise Power	-101.5 dBm
RIN Power	-99.2 dBm
Spontaneous-Spontaneous Beat Noise Power	-116.7 dBm
Signal-Spontaneous Beat Noise Power	-92.4 dBm
Total Noise Power	-84.1 dBm

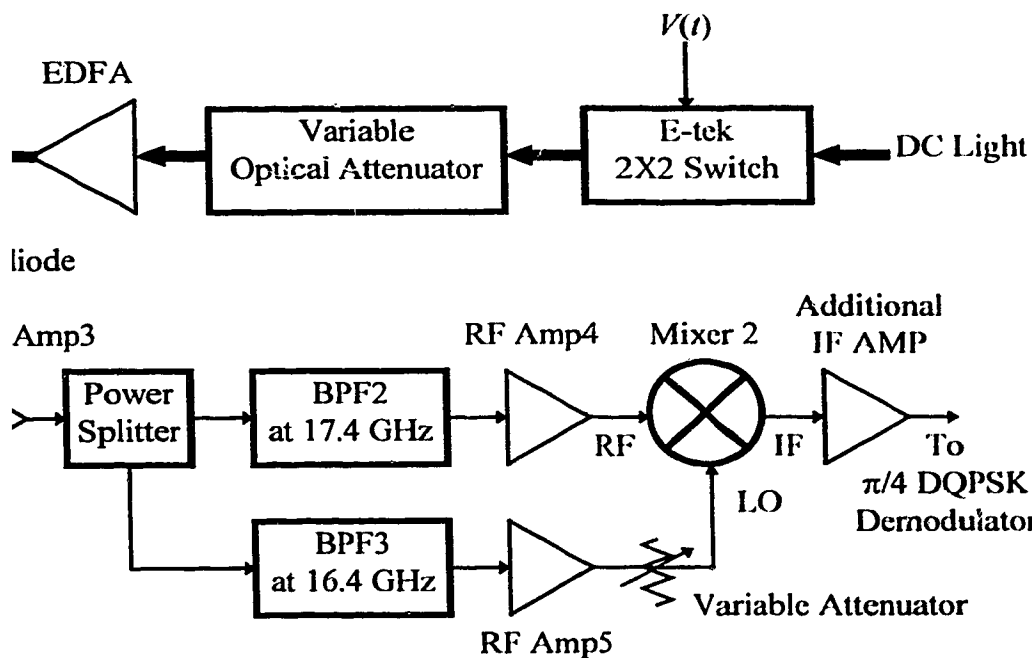
Table 13: Noise Contribution for Experiment #4

### 5.3.5 Experiment #5: BER vs. Optical Loss Measurement

The use of an EDFA makes possible the introduction of extra optical loss in the system, which means that it is possible to perform BER measurements under varying optical loss conditions. Figure 50 illustrates the experimental setup for this measurement. On the optical side, the external modulator is biased at its maximum transmission point. A variable optical attenuator (VOA) is substituted in place of the 50 km optical fiber to provide a variable optical loss. This VOA has an optical insertion loss of 2.0 dB even when the optical attenuation is set to 0 dB. An electrical variable attenuator is placed at the LO port of Mixer 2 in order to limit this input level to a constant +10 dBm; although not shown in Figure 50, the same variable attenuator is also inserted at the LO input of the I & Q Phase Detector for the same function. Furthermore, an additional IF amplifier is required at the IF output of Mixer 2 to provide the necessary power level at the LO input of the I & Q Phase Detector.

Even with this more elaborate setup, the usable electrical input power range of the receiver is only 5.0 dB. This usable power range is defined by the maximum and minimum settings on the VOA during the experiment. The maximum VOA setting used is 9.0 dB under which the LO input to Mixer 2 falls below +10 dBm even when the electrical attenuator is adjusted to minimum. The minimum VOA setting is 6.5 dB; it is the minimum setting which generates enough errors for the BER Test Set to obtain a

electrical power range of 5.0 dB, which is quite low due to the stringent requirement of constant input power levels to the LO ports. It is possible to relax the LO requirement by 1 or 2 dB without drastically affecting the performance of the system. The slight change in performance may result in a significant variation in the measurement, hence the experiment was performed with the LO input levels at a constant level. Furthermore, if a 16.4 GHz source had been available, the power range of the receiver could have been greatly increased since the only requirement would be the I & Q Phase Detector LO port power. Since IF amplifiers are readily available at TRLabs, this LO power level could be easily maintained at a constant level. Lastly, the usable power range could also be increased if a different receiver capable of counting a BER of less than  $10^{-10}$  is available.



### Experimental Setup for BER vs. Optical Loss Measurement

In the experiment, the EDFA gain is set to 12.5 dB and is kept constant for all optical loss settings. This is possible since the maximum input power to the EDFA was -16 dBm which is small enough to remain out of the saturation region of -16 dBm.



for the EDFA used. This maximum input power is obtained with the VOA adjusted to the minimum attenuation setting of 6.5 dB (recall that the VOA has an optical insertion loss of 2.0 dB) giving the net optical attenuation of 8.2 dB. The normalized input RF drive amplitudes ( $\alpha$  and  $\beta$ ) to the external modulator are adjusted to produce maximum power at 16.4 GHz since this is one of the limiting factors for the receiver dynamic range. In Figure 51, measured BER values for the received  $\pi/4$  DQPSK signal at 1.0 GHz are plotted against different SNR values for various optical loss settings. The  $\pi/4$  DQPSK MODEM limit is also plotted on the same graph for comparison. Table 14 summarizes the relationship between the optical loss settings and the corresponding SNRs. Note that the measured BER values are consistently slightly better than the MODEM limit, but since the differences in BER values between the two curves are very small and are within experimental uncertainties, it can be concluded that the experimental system is only limited by the MODEM performance and not by the up-conversion technique. For a more meaningful comparison, the usable power range of the receiver should be increased by either the use of an external LO source at 16.4 GHz or by additional electrical amplification of the up-converted LO signal. Improvement in the design and implementation of the demodulator may also boost the usable power range. Nonetheless, this experiment demonstrates the relationship between the BER and optical loss of the proposed up-conversion scheme within the experimental error limits.

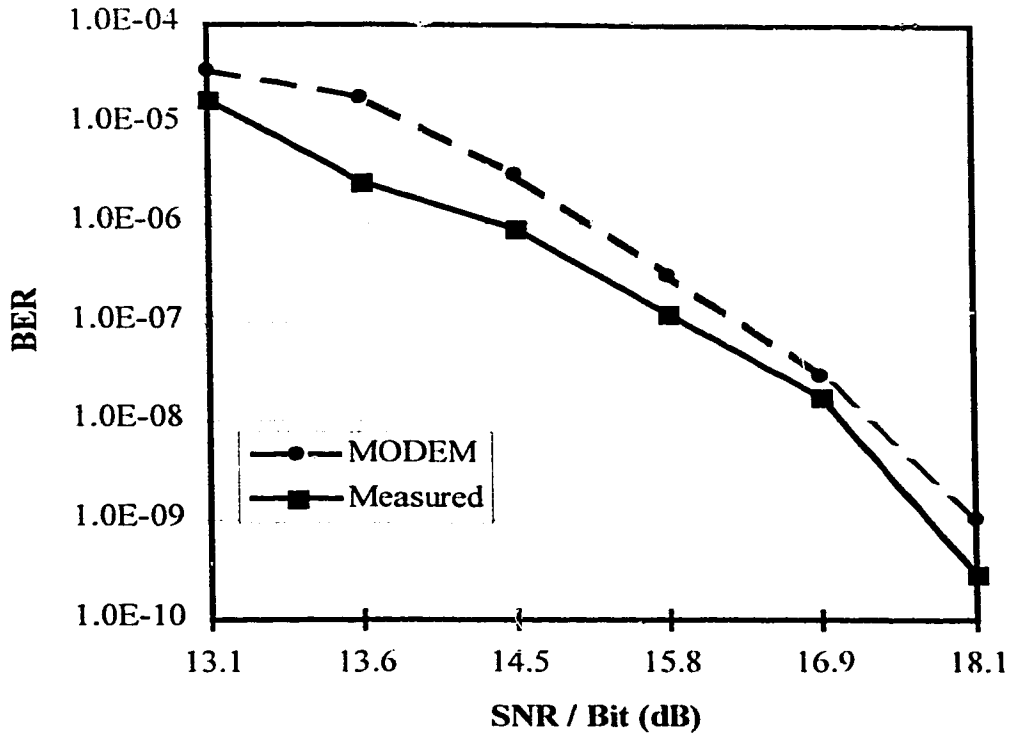


Figure 51: BER Performance vs. SNR

SNR / Bit (dB)	16.1	16.6	17.5	18.8	19.9	21.1
Optical Loss (dB)	11.0	10.5	10.0	9.5	9.0	8.5

Table 14: Optical Loss Settings

### 5.3.6 Experiment #6: Dispersion Experiment

Effects of chromatic dispersion for optical subcarrier system with subcarrier frequencies in the MMW range is another research area currently under study at TRLabs. To illustrate the problem of chromatic dispersion, let's examine the spectrum of the optical signal in the experiment. For the proposed system, the subcarriers are at 16.4 and 17.4 GHz. If we assume that these subcarriers are present at the transmitter, the optical spectrum would then contain two pairs of sidebands separated by 32.8 and 34.8 GHz and

centered at the optical carrier frequency (in THz). As these sidebands travel down a length of dispersive fiber, the upper and lower sidebands experience different propagation delays and therefore may add destructively at the end of the fiber if they are out of phase by exactly  $180^\circ$ . Using Eq. 4-3 at 1551 nm, the frequency separations of 32.8 and 34.8 GHz correspond to the linewidths of 0.263 and 0.279 nm respectively. With a dispersion factor of 17 ps/(km-nm) for the standard single mode fiber used, the relative delays between the upper and lower sidebands are respectively 4.47 and 4.74 ps/km for the 16.4 and 17.4 GHz subcarriers. This means that the upper and lower sidebands will be half a period out of phase if the length of the fiber is any odd multiple of 6.80 km for the 16.4 GHz signal and 6.06 km for the 17.4 GHz signal. It is therefore essential that the lengths of fiber used in the experiments do not lead to complete destructive interference of the upper and lower sidebands for both subcarrier frequencies.

Results of an exploratory experiment designed to illustrate the effects of dispersive fiber with the proposed up-conversion scheme are presented here. A more thorough investigation into dispersion effects in optical transmission system with unmodulated single-tone subcarrier at 5.0 GHz can be found in reference [42], but the analysis of dispersion limited microwave subcarrier transmission using Mach-Zehnder modulator non-linearity is beyond the scope of this project.

The setup for this experiment is similar to the one used in experiment 4 with the 50 km of fiber replaced with a VOA and various lengths of fiber (24, 35, and 50 km). With the VOA set to zero, the averaged optical power at the photodiode is recorded. Measurements are then taken for the up-converted electrical power levels at 16.4 and 17.4 GHz at the outputs of RF Amp4 and RF Amp5, the SNR at 1.0 GHz, and the corresponding BER. To establish the effect of fiber dispersion, the optical fiber is taken out of the experimental setup and the VOA is adjusted to produce the same optical power level at the photodiode so that the optical noise and signal levels are consistent with the previous measurements. Table 15 summarizes the results obtained for this experiment.

Fiber Length	Carrier Power at 17.4 GHz (dBm)	Carrier Power at 16.4 GHz (dBm)	SNR per bit at 1.0 GHz (dB)	Measured BER
25 km	-0.6	+9.2	16.5	$1 \times 10^{-6}$
No Fiber	+1.5	+10.5	20.8	$5 \times 10^{-9}$
35 km	-2.6	+9.1	14.9	$1 \times 10^{-5}$
No Fiber	-2.0	+9.7	17.2	$2 \times 10^{-7}$
50 km	-6.5	+9.2	12.5	$3 \times 10^{-5}$
No Fiber	-6.8	+7.3	12.5	$5 \times 10^{-5}$

Table 15: Experimental Results for Experiment #6

From this table it can be concluded that the system performance is indeed altered by the introduction of dispersive fiber. Both SNR and BER are generally degraded as a result of fiber dispersion except in the last case where 50 km of fiber are used. Since dispersion is a fiber length dependent process it is possible that at a given length of fiber the system performance is unaltered as compared to a dispersion free system for relatively narrow band signals. In fact, as discussed in reference [42], the detected microwave carriers after dispersive fiber may actually be higher in power as compared to a system using only optical attenuator depending on the chirp parameter of the external modulator and length of fiber used. To this end, the intent of this experiment is to introduce some of the system limiting effects of dispersion in a optical system employing microwave subcarriers; a more thorough study on this topic is required to quantitatively characterize the amount of dispersion penalty for wide band microwave subcarrier optical systems.

## **6. Conclusions**

### **6.1 Thesis Review**

Using the harmonic generation and opto-electronic mixing properties of Mach-Zehnder external modulators, the generation and transmission of  $\pi/4$  DQPSK signals at MMW frequencies has been demonstrated. This work was motivated by the need to generate MMW signals that are to be broadcast in future microcellular systems. To put this in context, chapter 1 introduced the microcellular system on a system level as a possible solution to the rising demand in wireless communications. Various advantages of using optical fiber as the feeder network for such a microcellular system were then highlighted. It was also concluded that MMW signals are inherently more suitable to microcellular applications. This led to a review of various techniques for the generation of MMW optical signals. The technique using the non-linearity of the Mach-Zehnder external modulator to up-convert signals at lower frequencies was emphasized due its implication of simple base station design and its exceptional optical line width performance. It was also pointed out that a published Mach-Zehnder non-linearity technique [20] requires a significant amount of optical hardware to impose modulation onto the up-converted signal. Therefore, the main objective of this thesis project was the demonstration of the viability of using the Mach-Zehnder non-linearity to up-convert both unmodulated tones and  $\pi/4$  DQPSK signals to MMW frequencies and to detect these signals successfully after transmission over optical fiber.

Chapter 2 began by introducing the theory of operation for a Mach-Zehnder external modulator. The theory behind the proposed system, which utilizes the harmonic generation as well as opto-electronic mixing properties of the Mach-Zehnder modulator, was presented. It was shown that with the proposed up-conversion technique, it is possible to up-convert a modulated signal using only one external modulator. In addition to the modulated MMW signal, it was also demonstrated that an unmodulated carrier can

be simultaneously up-converted to a frequency near the modulated signal. This chapter ended with the discussion of the use of the unmodulated carrier to simplify the base station design by eliminating the need for a LO source which, in a fully implemented system, would be required to down-convert the received signal in the up-link path of a microcellular system.

In chapter 3, the  $\pi/4$  DQPSK modulation format was chosen due to its compatibility with the proposed up-conversion technique, wide acceptance in the wireless communications industry, and relatively simple demodulator design. The operation of this modulation format was then introduced, followed by the block diagram level descriptions of the modulator and demodulator. The BER performance of the  $\pi/4$  DQPSK modulation format in the presence of additive white Gaussian noise was also presented in the end of this chapter, and the goal of  $10^{-9}$  BER was set for the experiments.

Chapter 4 presented the experimental setup for the thesis project and a characterization of the various building blocks. In order to verify the validity of the proposed up-conversion technique, a preliminary FM experiment was performed prior to the design and construction of the  $\pi/4$  DQPSK modulator/demodulator. To demonstrate the proposed usage of the unmodulated carrier in a microcellular system, this signal was used to down-convert the received  $\pi/4$  DQPSK signal in the experiment. Every optical and electrical component used in the experiments was also characterized including a more detailed description of the  $\pi/4$  DQPSK modulator/demodulator. A description of overall system noise degradation due to these components was included at the end of this chapter.

The experimental transmission results were described in chapter 5. First, the results of the preliminary FM experiment was presented. Based on this experiment, it was concluded that the proposed up-conversion technique can indeed be used to modulate as well as up-convert a MMW optical subcarrier. These results revealed that even after transmission through 20 km of dispersive fiber and an EDFA, the spectra of the modulated signals at 17.35 GHz and 18.30 GHz were identical to the theoretical simulations. It was therefore concluded that experimental designs be implemented for the

$\pi/4$  DQPSK experiments. The noise or BER performance of the  $\pi/4$  DQPSK MODEM was then determined using the ASE beat noise of the EDFA as a wide band noise source, and the resulting BER versus SNR curve illustrated the experimental limit of the overall system.

Six  $\pi/4$  DQPSK transmission experiments were performed. The first experiment demonstrated the operation of the proposed system when the Mach-Zehnder modulator was biased at the maximum transmission point. For this first experiment, no fiber was used. A BER of  $1 \times 10^{-9}$  and SNR of 18.4 dB was obtained, which are both more than adequate for microcellular applications. The second experiment involved the addition of 25 km of optical fiber and the resulting BER of  $2 \times 10^{-7}$  was measured. This experiment proved the distribution capability of the proposed system without the use of an optical amplifier. Experiment three was intended as a comparison between the two possible DC operating points of the Mach-Zehnder external modulator, i.e., at the maximum and minimum transmission. The experimental results demonstrated that the system performance was nearly identical under both operating conditions since thermal noise was the dominant noise factor for both experiments. In the fourth experiment, an EDFA and 50 km of optical fiber were used to validate the longer haul transmission performance using an optical pre-amplifier. Again excellent results of SNR=17.5 dB and BER= $2 \times 10^{-10}$  were measured. Finally, the system was reconfigured to provide for BER versus SNR measurement in the fifth experiment. It was shown that the usable input power range of the receiver is limited to 5 dB due to the unique use of the LO signal in the system, which is adequate for obtaining a BER versus SNR curve. From this curve it was shown that the up-conversion scheme is limited only by the MODEM performance for this experimental setup. A final experiment was presented to illustrate the effects of chromatic dispersion on the experimental system and it was concluded that the system performance was indeed dependent on the length of fiber used.

Despite the good BER and SNR measurements obtained, there were some problems associated with the experimental system. First of all, the measured BER readings were

never quite as low as predicted by calculations using measured SNR values due to the MODEM performance limit. Second, it was not possible to predict accurately the received signal power at a particular up-conversion frequency. Both of these shortcomings may be caused by non-ideal components used in the system, but further investigation is required to fully account for them. Nonetheless, it is noteworthy that the MODEM's performance came within approximately 3 dB of an ideal demodulator down to a BER of  $10^{-10}$ . From a proof-of-concept perspective, all of the experimental results supported the use of the proposed system in generating and transmitting  $\pi/4$  DQPSK MMW signals over optical fiber, hence this thesis project can be considered a success.

## **6.2 Future Improvement and Research**

There are a few unresolved aspects in the proposed system which demand further investigation but are beyond the scope or time constraint of this thesis project. The most obvious one is to improve the performance of the demodulator so that the measured BER can correlate better with theoretical values. Secondly, the dynamic response of the Mach-Zehnder modulator should also be taken into account so that the up-converted signal power levels can be accurately predicted. In addition, since the proposed up-conversion technique was intended for microcellular applications, the concept will not be fully proven until wireless links and two way optical fiber transmission are implemented in the experiments. This will also require the characterization of the radio channel at 16 to 18 GHz to better understand the overall system performance. The use of the up-converted LO signal at 16.4 GHz should also be configured for its intended use; that is, it should be tested in the down-conversion of a received MMW at the base station to directly modulate a laser diode for the up-link connection.

There are also other areas relating to this work which demand additional research. One possible research area is the choice of other digital modulation schemes that are more suitable to wireless Local Area Network (LAN) applications such as Code Division Multiple Access (CDMA) [43]. There are also other sources of optical non-linearity



which may be exploited to generate MMW signals such as harmonic generation due to laser clipping. Both of these research topics are currently under study at TRLabs.

This thesis deals with the technology of providing wireless communications. The freedom to communicate with anyone at any location within a microcellular system is perhaps the strongest driving force behind all the research in this area. As research in the field of RF on fiber intensifies, it will be interesting to see how these two exciting technologies continue to converge in the future.

## List of References

- [1] Greenstein, L. J., Amitay, N., Chu, T., Cimini, L. J., Foschini, G. J., Gans, M. J., I, C., Rustako, A. J., Valenzuela, R. A., and Vannucci, G., "Microcells in Personal Communications Systems", *IEEE Communications Magazine*, pp. 76-88 December 1992.
- [2] Lee, W. C. Y., "Smaller Cells for Greater Performance", *IEEE Communications Magazine*, pp. 19-23, November 1991.
- [3] Potter, A. R., et al., "Increasing the Capacity of a Digital Cellular Radio System Using Microcellular Systems", *Proceedings of International Conference on Digital Land Mobile Radio Communications*, June 1987.
- [4] Hawkins, P. W., "The Millimetric Opportunity - How Real is the Hype?", *ICC '91 Conference Record*, vol. 3, pp. 1196-1200, 1991.
- [5] Shibutani, M., Kanai, T., Emura, K., and Namiki, J., "Feasibility Studies on an Optical Fiber Feeder System for Microcellular Mobile Communication Systems", *ICC '91 Conference Record*, vol. 3, pp. 1176-1181, 1991.
- [6] Yoneda, E., Suto, K., Kikushima, K., and Yoshinaga, H., "All-Fiber Video Distribution (AFVD) Systems Using SCM and EDFA Techniques", *Journal of Lightwave Technology*, vol. 11, no. 1, pp. 128-137, January 1993.
- [7] Darcie, T. E. and Bodeep, G. E., "Lightwave Subcarrier CATV Transmission Systems", *IEEE Transactions on Microwave Theory and Techniques*, vol. 38, no. 5, pp. 524-533, May 1990.
- [8] Morita, K. and Ohtsuka, H., "The New Generation of Wireless Communications Based on Fiber-Radio Technologies", *IEICE Transactions on Communications*, vol. E76-B, no. 9, pp. 1061-1068, September 1993.
- [9] Shibutani, M., Kanai, T., Domom, W., Emura, K., and Namiki, J., "Optical Fiber Feeder for Microcellular Mobile Communication Systems (H-015)", *IEEE Journal on Selected Areas in Communications*, vol. 11, no. 7, pp. 1118-1126, September 1993.
- [10] Ohmoto, R., Ohtsuka, H., and Ichikawa, H., "Fiber-Optic Microcell Radio Systems with a Spectrum Delivery Scheme", *IEEE Journal on Selected Areas in Communications*, vol. 11, no. 7, pp. 1108-1117, September 1993.
- [11] Chu, T. and Gans, M. J., "Fiber Optic Microcellular Radio", *IEEE Transactions of Vehicular Technology*, vol. 40, no. 3, pp. 599-606, August 1991.

- [12] Ogawa, H., "Microwave and Millimeter-Wave Fiber Optic Technologies for Subcarrier Transmission Systems", *IEICE Transactions on Communications*, vol. E76-B, no. 9, pp. 1078-1090, September 1993.
- [13] Dolfi, D. W. and Ranganath, T. R., "50 GHz Velocity-Matched Broad Wavelength LiNbO<sub>3</sub> Modulator with Multimode Active Section", *Electronics Letters*, vol. 28, no. 13, pp. 1197-1198, 1992.
- [14] Ogawa, H. and Polifko, D., "Fiber Optic Millimeter-Wave Subcarrier Transmission Links for Personal Radio Communication Systems", *IEEE Microwave Theory and Techniques - Symposium Digest*, pp. 555-558, 1992.
- [15] Saleh, B. E. A. and Teich, M. C., Fundamentals of Photonics, John Wiley & Sons Inc., pp. 703-705, 1991.
- [16] Liu, Q. Z., Davies, R., and MacDonald, R. I., "Experimental Investigation of Fiber Optic Microwave Link with Monolithic Integrated Optoelectronic Mixing Receiver", *IEEE Transactions on Microwave Theory and Techniques*, vol. 43, no. 9, pp. 2357-2360, September 1995.
- [17] Simonis, G. J. and Purchase, K. G., "Optical Generation, Distribution, and Control of Microwaves Using Laser Heterodyne", *IEEE Transactions on Microwave Theory and Techniques*, vol. 38, no. 5, pp. 667-669, May 1990.
- [18] Daryoush, A. S., Herczfeld, P. R., Turske, Z., and Wahi, P. K., "Comparison of Indirect Optical Injection-Locking Techniques of Multiple X-Band Oscillators", *IEEE Transactions on Microwave Theory and Techniques*, vol. 34, no. 12, pp. 1363-1369, December 1986.
- [19] Herczfeld, P. R., Daryoush, A. S., Rosen, A., Sharma, A. K., and Contarino, V. M., "Indirect Subharmonic Optical Injection locking of a Millimeter-Wave IMPATT Oscillator", *IEEE Transactions on Microwave Theory and Techniques*, vol. 34, no. 12, pp. 1371-1375, December 1986.
- [20] O'Reilly, J. and Lane, P., "Remote Delivery of Video Services Using mm-Waves and Optics", *Journal of Lightwave Technology*, vol. 12, no. 2, pp. 369-375, February 1994.
- [21] O'Reilly, J. and Lane, P., "Fibre-Supported Optical Generation and Delivery of 60 GHz Signals", *Electronics Letters*, vol. 30, no. 16, pp. 1329-1330, August 1994.
- [22] O'Reilly, J. J., Lane, P. M., Heidemann, R., and Hofstetter, R., "Optical Generation of Very Narrow Linewidth Millimeter Wave Signals", *Electronics Letters*, vol. 28, no. 25, pp. 2309-2311, December 1992.

- [23] Schmuck, H., Heidemann, R., and Hofstetter, R., "Distribution of 60 GHz Signals to more than 1000 Base Stations", *Electronics Letters*, vol. 30, no. 1, pp. 59-60, January 1994.
- [24] O'Reilly, J. and Lane, P., "Delivering Broadband Services via Fibre - mm Wave Radio", *Proceedings of International Symposium on Fibre Optic Networks and Video Communications*, vol. 1974, pp. 6-17, 1993.
- [25] Koyama, F. and Iga, K., "Frequency Chirping in External Modulators", *Journal of Lightwave Technology*, vol. 6, no. 1, pp. 87-92, January 1988.
- [26] Gradshteyn, I. S. and Ryzhik, I. M., Table of Integrals, Series, and Products, Academic Press Inc., 1980.
- [27] O'Reilly, J. J., Lane, P. M., Capstick, M. H., Salgado, H. M., Heidemann, R., Hofstetter, R., and Schmuck, H., "RACE R2005: Microwave Optical Duplex Antenna Link", *IEE Proceedings-J*, vol. 140, no. 6., pp. 385-391, December 1993.
- [28] Baker, P. A., "Phase-Modulation Data Sets for Serial Transmission at 2,000 and 2,400 Bits per Second", *AIEE Transactions Part 1: Communication Electronics*, vol. 81, pp. 166-171, July 1962.
- [29] Ng, C. S., Tjhung, T. T., Adachi, F., and Lye, K. M., "On the Error Rates of Differentially Detected Narrowband  $\pi/4$  DQPSK in Rayleigh Fading and Gaussian Noise", *IEEE Transactions on Vehicular Technology*, vol. 42, no. 3, pp. 259-265, August 1993.
- [30] Adachi, F. and Ohno, K., "BER Performance of QDPSK with Postdetection Diversity Reception in Mobile Radio Channels", *IEEE Transactions on Vehicular Technology*, vol. 40, no. 1, pp. 237-249, February 1991.
- [31] Proakis, J. G., Digital Communications, McGraw-Hill Book Co., pp. 265-272, 1989.
- [32] Petermann, K., Laser Diode Modulation and Noise, Kluwer Academic Publishers, pp. 152-162, 1988.
- [33] Gimlett, J. L., Iqbal, M. Z., Cheung, N. K., Righetti, A., Fontana, F., and Grasso, G., "Observation of Equivalent Rayleigh Scattering Mirrors in Lightwave Systems with Optical Amplifiers", *IEEE Photonics Technology Letters*, vol. 2, no. 3, pp. 211-213, March 1990.
- [34] Koehler, B. G. and Bowers, J. E., "In-Line Single-Mode Fiber Polarization Controllers at 1.55, 1.30, and 0.63  $\mu\text{m}$ ", *Applied Optics*, vol. 24, no. 3, pp. 349-353, February 1985.

- [35] Desurvire, E., Erbium Doped Fiber Amplifiers: Principles and Applications, John Wiley & Sons Inc., 1994.
- [36] Olsson, N. A., "Lightwave Systems with Optical Amplifiers", *Journal of Lightwave Technology*, vol. 7, no. 7, pp. 1071-1082, July 1989.
- [37] Habba, I. M. I. and Cimini, L. J., "Optimized Performance of Erbium-Doped Fiber Amplifiers in Subcarrier Multiplexed Lightwave AM-VSB CATV Systems", *Journal of Lightwave Technology*, vol. 9, no. 10, pp. 1321-1329, October 1991.
- [38] Ziemer, R. E. and Tranter, W. H., Principles of Communications: Systems, Modulation, and Noise, Houghton Mifflin Co., pp. 770-771, 1990.
- [39] Young, T., Conradi, J., Tinga, W., and Davies, B., "Generation and Transmission of FM and  $\pi/4$  DQPSK Signals at Microwave Frequencies Using Harmonic Generation and Optoelectronic Mixing in Mach-Zehnder Modulators", *Tenth International Conference on Integrated Optics and Optical Fibre Communication - Technical Digest*, vol. 4, pp. 72-73, June 1995.
- [40] Young, T., Conradi, J., and Tinga, W., "Generation and Transmission of FM and  $\pi/4$  DQPSK Signals at Microwave Frequencies Using Harmonic Generation and Optoelectronic Mixing in Mach-Zehnder Modulators", to be published in an upcoming issue of *IEEE Transactions on Microwave Theory and Techniques*.
- [41] Stremmler, F. G., Introduction to Communication Systems, Addison-Wesley Publishing Co., pp. 386-390, 1990.
- [42] Hakki, B. W., "Dispersion of Microwave-Modulated Optical Signals", *Journal of Lightwave Technology*, vol. 11, no. 3, pp. 474-480, March 1993.
- [43] Whipple, D. P., "North American Cellular CDMA", *Hewlett-Packard Journal*, pp. 90-97, December 1993.
- [44] Benterud, K. R., Fiber Optic Transmission Using Optical Time Division Multiplexing, University of Alberta M. Sc. Thesis, pp. 71-73, July 1993.

## **Appendix A: Digital Cellular System Standards**

Standards	IS-54 North America Digital Cellular	IS-95 North America Digital Cellular	GSM Global System for Mobile Communications (Europe)	PDC Personal Digital Cellular (Japan)
Frequency Allocation (MHz)	Rx: 869-894 Tx: 824-849	Rx: 869-894 Tx: 824-849	Rx: 935-960 Tx: 890-915	Rx: 940-956 1477-1501 Tx: 810-826 1429-1453
Multiple Access Method	TDMA FDM	CDMA FDM	TDMA FDM	TDMA FDM
Duplex Method	FDD	FDD	FDD	FDD
Number of Channels	832 (3 users per channel)	10 (118 users per channel)	124 (8 users per channel)	1600 (3 users per channel)
Channel Spacing	30 kHz	1250 kHz	200 kHz	25 kHz
Modulation Format	$\pi/4$ DQPSK	BPSK / OQPSK	GMSK (0.3 Gaussian Filter)	$\pi/4$ DQPSK
Bit Rate	48.6 kb/s	1.2288 Mb/s	270.833 kb/s	42 kb/s

Table 16: Digital Cellular System Standards

TDMA: Time Division Multiple Access

FDM: Frequency Division Multiplexing

FDD: Frequency Division Duplex

Rx: Receive Frequency Range

Tx: Transmit Frequency Range

BPSK: Binary Phase Shift Keying

DQPSK: Differential Quaternary Phase Shift Keying

OQPSK: Offset Quadrature Phase Shift Keying

GMSK: Gaussian Minimum Phase Shift Keying

## **Appendix B: Digital Cordless Phone Standards**

Standards	CT2 / CT2+ Cordless Telephone 2	DECT Digital European Cordless Telephone	PHP Personal Handy Phone (Japan)	DCS 1800 Digital Cordless Standard (UK)
Frequency Allocation (MHz)	CT2: 864/868  CT2+: 930/931 940/941	1880-1990	1895-1907	Rx: 1805- 1880  Tx: 1710- 1785
Multiple Access Method	TDMA  FDM	TDMA  FDM	TDMA  FDM	TDMA  FDM
Duplex Method	TDD	TDD	TDD	FDD
Number of Channels	40	10 (12 users per channel)	300 (4 users per channel)	750 (16 users per channel)
Channel Spacing	100 kHz	1728 kHz	300 kHz	200 kHz
Modulation Format	GFSK (0.5 Gaussian Filter)	GFSK (0.5 Gaussian Filter)	$\pi/4$ DQPSK	GMSK (0.3 Gaussian Filter)
Bit Rate	72 kb/s	1.152 Mb/s	384 kb/s	270.833 kb/s

**Table 17: Digital Cordless Telephone Standards**

**TDMA: Time Division Multiple Access**

**FDM: Frequency Division Multiplexing**

**FDD: Frequency Division Duplex**

**TDD: Time Division Duplex**

**Rx: Receive Frequency Range**

**Tx: Transmit Frequency Range**

**BPSK: Binary Phase Shift Keying**

**GFSK: Gaussian Frequency Shift Keying**

**DQPSK: Differential Quaternary Phase Shift Keying**

**GMSK: Gaussian Minimum Phase Shift Keying**

## Appendix C: $\pi/4$ DQPSK Modulator Design

This appendix contains the schematic level design description for the  $\pi/4$  DQPSK modulator. A functional description of the modulator was presented in section 4.3.4. The block diagram for the  $\pi/4$  DQPSK Modulator is shown again in the following figure. Schematic diagrams for the modulator can be found in Figures A1 to A5. Fast Transistor-Transistor-Logic (Fast TTL) family digital components are used for both the modulator and demodulator due to its exceptional speed (typical clock rate of 100 MHz) and propagation delay (typically 3.7 ns). Although the Emitter-Coupled-Logic (ECL) family has even better performance than Fast TTL, it is more sensitive to noise and requires 50 Ohms transmission lines and terminations. Note that the propagation delays of the Fast TTL family approaches the clock period of the 50 MHz clock (20 ns), hence logic delays are used through out the design to adjust for proper timing between stages.

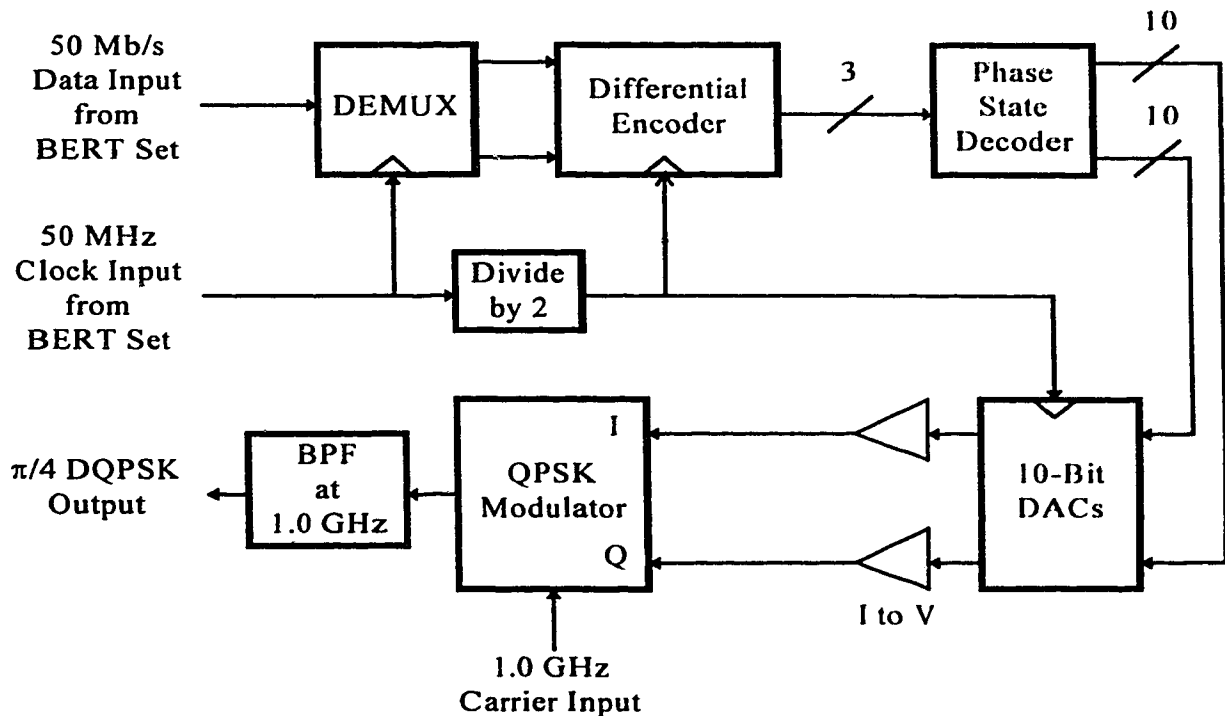


Figure 18:  $\pi/4$  DQPSK Modulator Block Diagram



### **DEMUX (refer to Appendix E1)**

The DEMUX (demultiplexer) serves the function of interleaving the 50 Mb/s input data stream into two parallel data lines at 25 Mb/s to form the symbol stream. A shift register is used to perform this function. This shift register is made up of two D flip-flops connected in series (U4). Outputs of the shift register (U4 PIN5 and PIN9) are connected to two data latches (U5) which are clocked by the 25 MHz clock. This 25 MHz clock is derived by passing the 50 MHz clock through a D flip-flop (U3). Since the shift register and the data latches are triggered by the 50 MHz and 25 MHz clocks respectively, the data is loaded into the data latches every second clock cycle in reference to the 50 MHz. As a result two parallel data streams represented by  $X_2, X_1$  are generated.

### **Differential Encoder (refer to Appendix E2)**

The differential encoder performs the function of making the absolute phase assignment based on the present symbol and the previous phase state. This requirement calls for a state machine. The following state diagram can be used to represent the differential encoding scheme

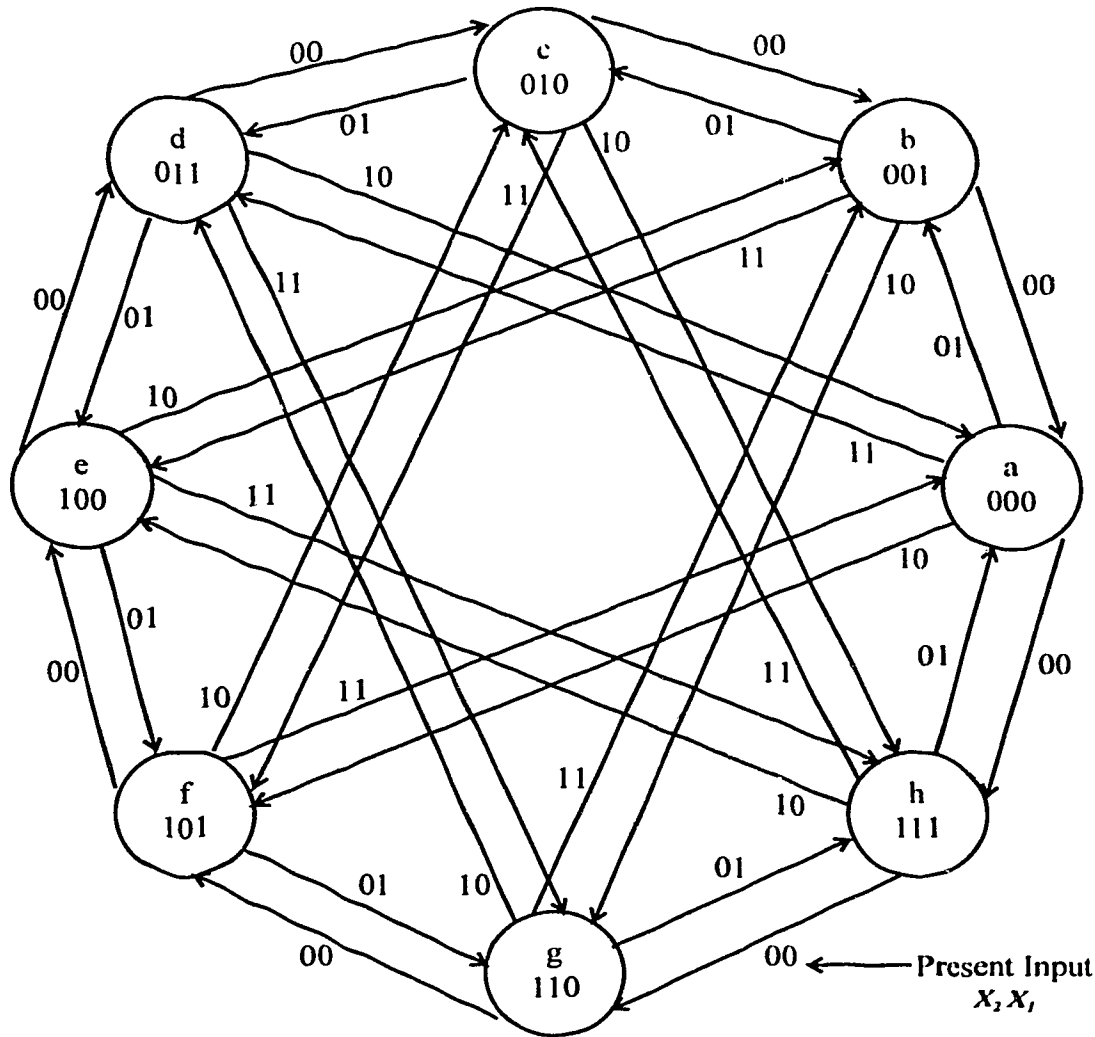


Figure 52: Differential Encoder State Diagram

Note that  $X_2$  and  $X_1$  define the current symbol generated by the MUX with  $X_2$  being the bit more advanced in time. The relationship between the logical states a to h and the absolute phase states is defined by the following table:

Logical States	a	b	c	d	e	f	g	h
Phase States	0	$\pi/4$	$\pi/2$	$3\pi/4$	$\pi$	$5\pi/4$	$3\pi/2$	$7\pi/4$

Table 18: Logical State Assignment

Based on the next state map, the following next state table can be constructed:

Present State $ABC$	Next State ( $A^+ B^+ C^+$ )			
	$X_2 X_1 = 01$	$X_2 X_1 = 00$	$X_2 X_1 = 11$	$X_2 X_1 = 10$
000	001	111	011	101
001	010	000	100	110
010	011	001	101	111
011	100	010	110	000
100	101	011	111	001
101	110	100	000	010
110	111	101	001	011
111	000	110	010	100

Table 19: Differential Encoder Next State Table

where  $A$ ,  $B$ ,  $C$ , and  $A^+$ ,  $B^+$ ,  $C^+$  are the present state and the next state variables respectively. By plotting the K-maps for the next state table, and simplifying using the J-K flip-flop implementation, the following logical expressions can be derived for the next state variables  $a^+$  and  $b^+$

$$J_A = \overline{BC}\overline{X_1} + \overline{BC}X_2 + \overline{BC}X_2 + BCX_1$$

$$K_A = J_A$$

$$J_B = \overline{C}\overline{X_2}\overline{X_1} + \overline{C}X_2X_1 + CX_2\overline{X_1} + C\overline{X_2}X_1$$

$$K_B = J_B$$

where  $J$  and  $K$  are the J and K inputs to the next state variable flip-flops. The next state variable  $C^+$  can also be easily obtained by plotting its K-map giving  $C^+ = \overline{C}$ . So a simple D flip-flop (U11) can be used for this next state variable. In Appendix E2, The combinational logic (U6 to U9) provides the necessary J and K inputs to the JK flip-flops (U10). These flip-flops are clocked by the 25 MHz clock so that a phase transition occurs for every symbol period. The outputs of the flip-flops represent the next state variables  $A$ ,  $B$ ,  $C$  and their complements.

### **Phase State Decoder (refer to Appendix E3)**

The phase state decoder maps the three next state variables onto one of eight ten bit digital words that represent the normalized I and Q current values for the corresponding phase state. These normalized I and Q currents specify the current values required to drive the I and Q mixers in the QPSK modulator to produce the correct phase state. They are normalized to the maximum current required to turn the mixers fully on. Table 20 illustrates the relationship between the logical states and the normalized current levels.

Phase States	0	$\pi/4$	$\pi/2$	$3\pi/4$	$\pi$	$5\pi/4$	$3\pi/2$	$7\pi/4$
Logical States ABC	000	001	010	011	100	101	110	111
Normalized I Current	1	0.707	0	-0.707	-1	-0.707	0	0.707
Normalized Q Current	0	0.707	1	0.707	0	-0.707	-1	-0.707

Table 20: Normalized I/Q Current Levels

To complete the modulator design, the DAC resolution of  $\pm 0.002$  A/A was chosen. With a 10-Bit DAC, and with the full scale normalized current of 2 A/A (from -1 to 1 A/A), the resolution available is  $2 / 2^{10} = 0.0019531$  A/A per bit, hence it is adequate for the application. Table 21 relates the 10-Bit code words to the five normalized current levels.

Normalized Current	-1	-0.707	0	0.707	1
Code Word	0000000000	0010010110	1000000000	1101101010	1111111111

Table 21: DAC Code Word Assignment

With the DAC code words defined, the following truth table can then be used to determine the logical expression for each bit of the code words.

<i>ABC</i>	I Current Code Word										Q Current Code Word									
	D9	D8	D7	D6	D5	D4	D3	D2	D1	D0	D9	D8	D7	D6	D5	D4	D3	D2	D1	D0
000	1	1	1	1	1	1	1	1	1	1	1	0	0	0	0	0	0	0	0	0
001	1	1	0	1	1	0	1	0	1	0	1	1	0	1	1	0	1	0	1	0
010	1	0	0	0	0	0	0	0	0	0	1	1	1	1	1	1	1	1	1	1
011	0	0	1	0	0	1	0	1	1	0	1	1	0	1	1	0	1	0	1	0
100	0	0	0	0	0	0	0	0	0	0	1	0	0	0	0	0	0	0	0	0
101	0	0	1	0	0	1	0	1	1	0	0	0	1	0	0	1	0	1	1	0
110	1	0	0	0	0	0	0	0	0	0	0	0	0	0	0	0	0	0	0	0
111	1	1	0	1	1	0	1	0	1	0	0	0	1	0	0	1	0	1	1	0

Table 22: DAC Code Word Truth Table

where D9 is the most significant bit of the code words. After constructing the K-map for each of the data inputs, the following logical expressions can be obtained for the inputs to the DACs

Inputs for the I DAC:

$$D9 = \overline{A}\overline{B} + B\overline{C} + AB$$

$$D8 = \overline{A}\overline{B} + ABC$$

$$D7 = \overline{A}\overline{B}\overline{C} + \overline{A}BC + A\overline{B}\overline{C}$$

$$D6 = D5 = D3 = D8$$

$$D4 = D2 = D7$$

$$D1 = \overline{A}\overline{B} + C$$

$$D0 = \overline{A}\overline{B}\overline{C}$$

Inputs for the Q DAC

$$D9 = \overline{A} + \overline{B}\overline{C}$$

$$D8 = \overline{A}B + \overline{A}C$$

$$D7 = \overline{A}B\overline{C} + AC$$

$$D6 = D5 = D3 = D8$$

$$D4 = D2 = D7$$

$$D1 = \overline{A}B + C$$

$$D0 = \overline{A}B\overline{C}$$

In Figure E3, the combinational logic (U12 to U17) performs the encoding defined by the above logical expressions based on the logical state  $ABC$ . The outputs D9 to D0 are generated to be fed as inputs to the DACs. Note that additional digital delays are used to introduce delay in the 25 MHz clock for proper timing.

### **10-Bit DACs and I to V Converters (refer to Appendix E4)**

Two Analog Devices AD9721 10-Bit, 100 Mega-sample/s D to A converters were used to produce the analog driving signals to the QPSK Modulator. These DACs (U19 and U20) accept the 10-bit code words from the Phase State Decoder as inputs and generate the corresponding output analog current levels. The full scale output current of the DAC is set to 0 to -20.41 mA for the digital inputs of 0000000000 to 1111111111. This full scale current is defined by the resistors connected to the  $R_{set}$  inputs (Pin 17) by the equation:  $I_{full-scale} = 32 \times (V_{Pin26} / R_{set})$ . In this case, Pins 26 are connected to the DACs' reference output (Pins 25) of -1.25 V and the resistor value used for  $R_{set}$  is 1960 Ohms giving the full scale current of -20.41 mA.

The I to V Converters consist of two Analog Devices AD9617 Wide Bandwidth Op Amps (U22 and U24). The current outputs of 0 to -20.41 mA from the DACs are fed to two 25 Ohms resistors in parallel (R4, R5 and R19, R11) resulting in the voltage outputs in the range of 0 to -0.2676 V. These two voltage signals are then connected to the inputs of the op-amps via R4 and R10. The gain of the op-amps can be adjusted up to 20 V/V via VR2 and VR4 resulting in the maximum output voltage range of 0 to -5.352 V. This voltage range is obviously not usable since bipolar driving signals are required for the QPSK Modulator, so additional AD708 Op Amps (U21 and U23) are used to inject extra current into the inputs of U22 and U24 to center the output voltage swing around 0 V. The first op-amps of U21 and U23 are employed as voltage buffers for the Reference Outputs (Pins 25) from the DACs. The second set of op-amps convert the voltage reference into a current reference. VR1 and VR3 can also be used to fine tune the amount of injected current so that the maximum output voltage range is exactly  $\pm 2.676$  V. This

voltage swing corresponds to the current range of  $\pm 53.5$  mA, which is more than enough to fully turn on the mixers inside the QPSK Modulator since only  $\pm 30$  mA is needed.

## **Appendix D: $\pi/4$ DQPSK Demodulator Design**

This appendix contains the design description for the  $\pi/4$  DQPSK modulator on a schematic level. A functional description of the Demodulator was presented in section 4.3.5. The block diagram for the  $\pi/4$  DQPSK Demodulator is redrawn again in the following figure. The schematic diagrams for the modulator can be found in Figure A6. Again, note that Fast TTL components are used for the demodulator.

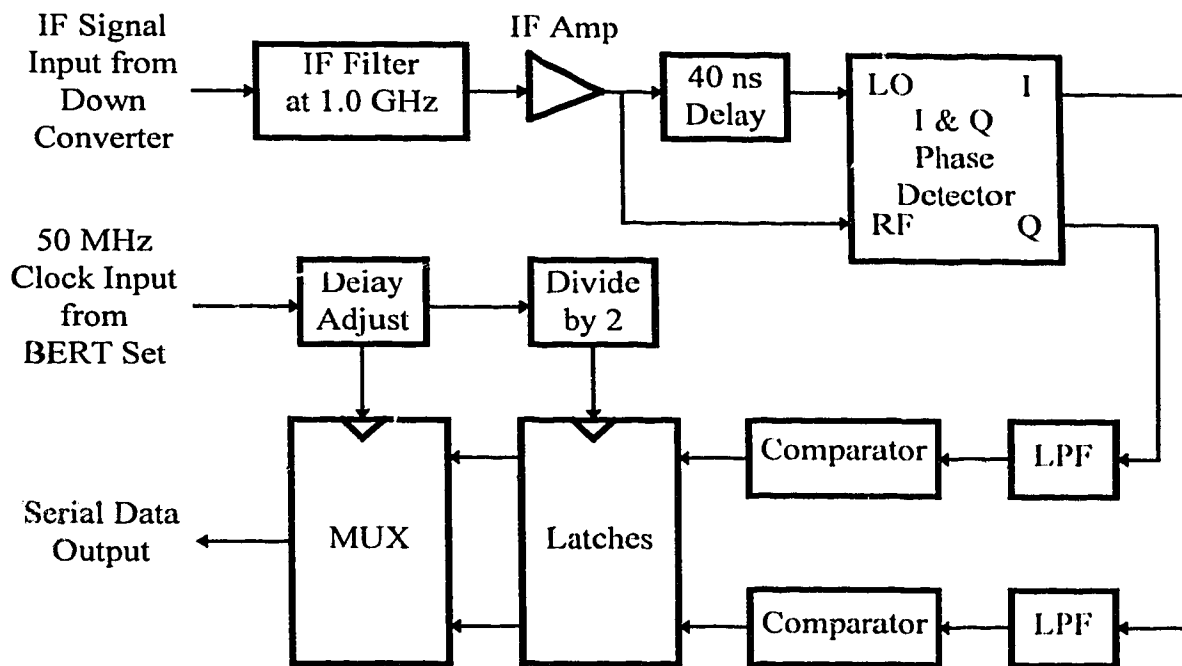


Figure 19:  $\pi/4$  DQPSK Demodulator Block Diagram

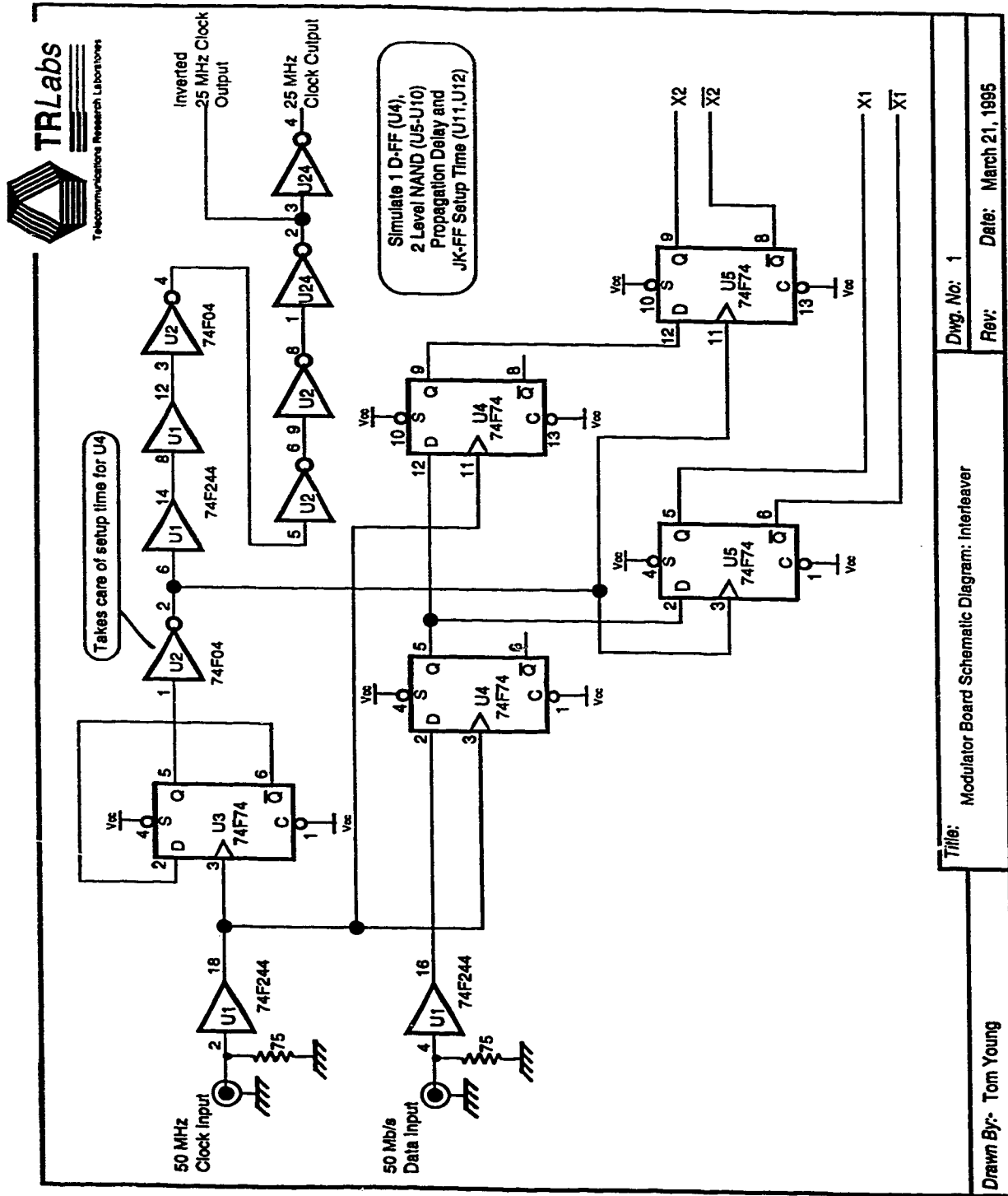
The schematic diagram containing the comparators, latches, MUX, delay adjust and Divide by 2 circuit can be found in Appendix E5. The low pass filtered I and Q decision variables are first fed to two buffers with variable gain. These buffers are constructed using the same AD9617 op-amps (U4 and U5) used in the modulator. Two Analog Devices high speed comparators (AD9698) from a dual package IC (U6) are used to performing the decision making. One of the comparator inputs is connected to ground while the other input is connected to the buffer output, so a transition occurs at the output



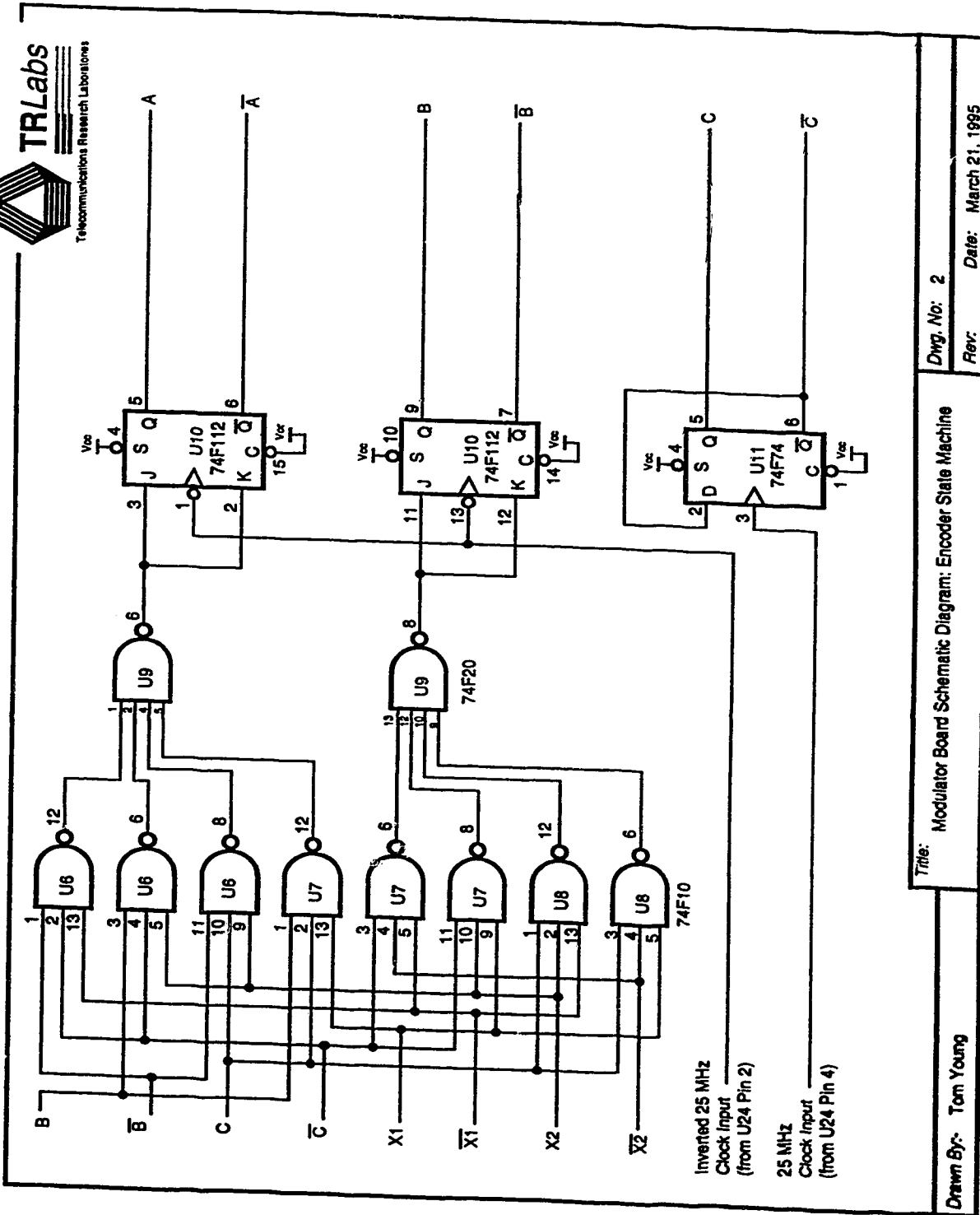
of the comparators whenever the buffered decision variables cross 0 V. The comparator outputs are fed to two data latches (U7), and the two parallel outputs from the data latches are converted back to a serial data stream via the multiplexer (U8). Two Dallas Semiconductors digital delays (DS1007) are used to provide for manual adjustment of the decision time by delaying the 50 MHz clock input. The first digital delay (U1) provides fine adjustment of 3, 4, 6, 8 or 10 ns using Delay Switch 1 while the second digital delay (U2) can be used to obtain coarse adjustment of 5, 10, 15, 20 and 25 ns using Delay Switch 2. The delayed 50 MHz clock signal is divided down to 25 MHz by a flip-flop (U3), and the 25 MHz is used to trigger the data latches. This 50 MHz clock is also routed to the output data latch (U3) which receives the output of the MUX as its input; this generates the 50 Mbit/s bit stream which is fed back to the BER test set for BER measurements. During the experiment, both delay switches are adjusted to give the optimal measured BER.

## **Appendix E: Schematic Diagrams**

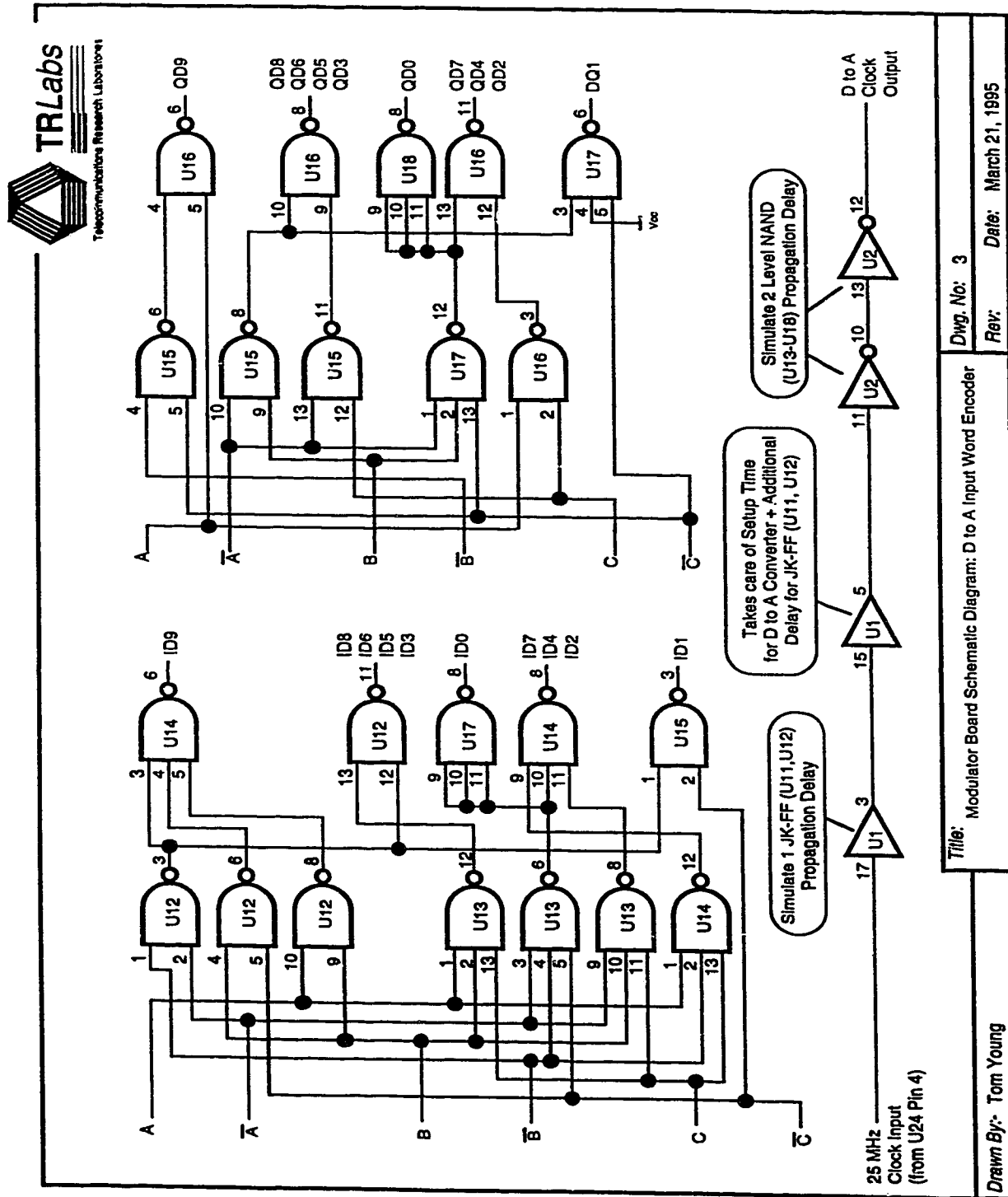
# Appendix E1: DEMUX Schematic



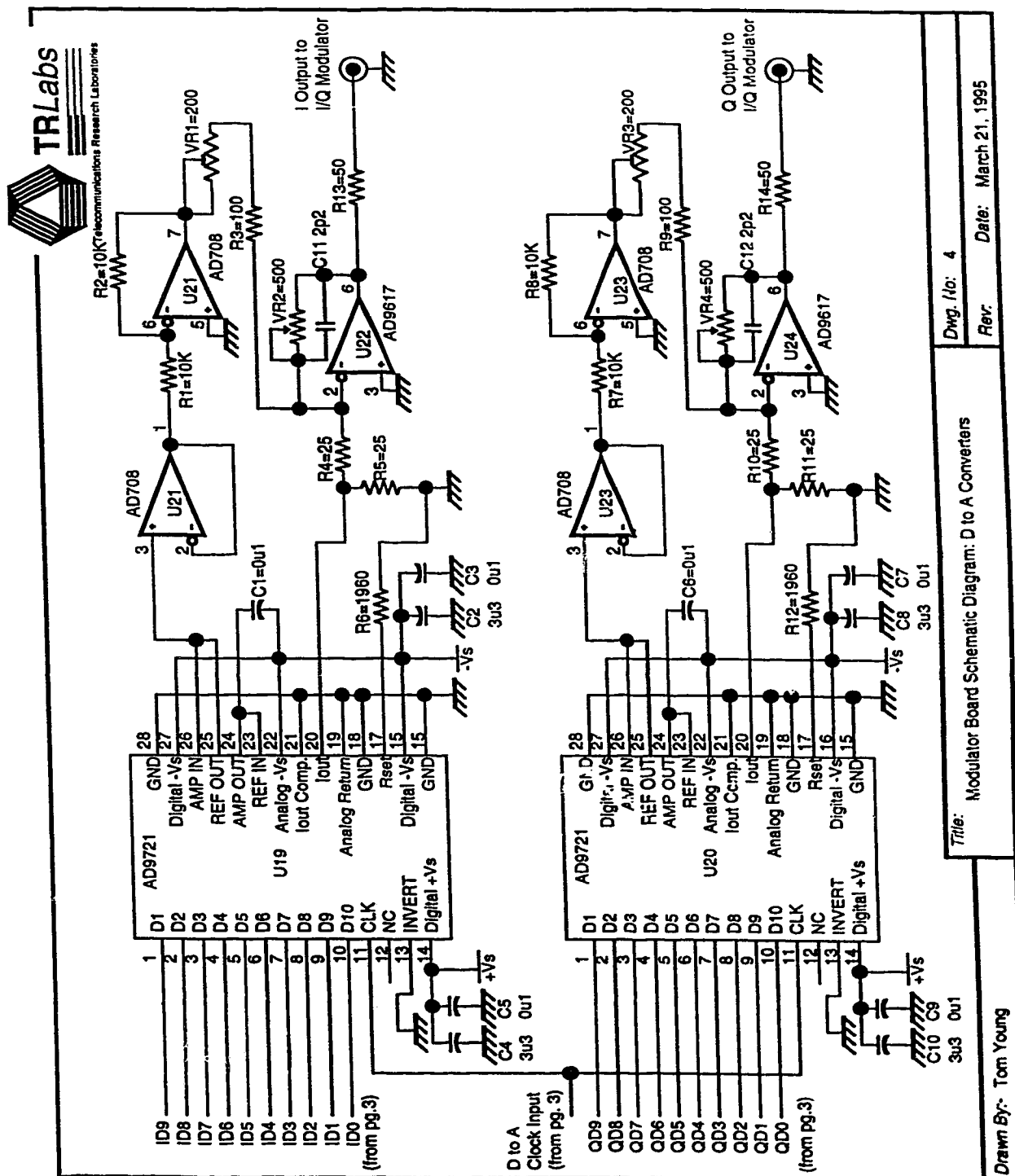
# Appendix E2: Differential Encoder Schematic



# Appendix E3: Phase State Decoder Schematic



# Appendix E4: DAC and I to V Schematic



# Appendix E5: Demodulator Schematic

